Louisiana Tech University
Louisiana Tech Digital Commons

Doctoral Dissertations | Graduate School

Fall 2011

Passive micromixers and organic electrochemical transistors for biosensor applications

Senaka Krishna Kanakamedala
Louisiana Tech University

Follow this and additional works at: https://digitalcommons.latech.edu/dissertations

Part of the Biomedical Engineering and Bioengineering Commons, Electrical and Computer Engineering Commons, and the Nanoscience and Nanotechnology Commons

Recommended Citation
Kanakamedala, Senaka Krishna, "" (2011). *Dissertation*. 366.
https://digitalcommons.latech.edu/dissertations/366

This Dissertation is brought to you for free and open access by the Graduate School at Louisiana Tech Digital Commons. It has been accepted for inclusion in Doctoral Dissertations by an authorized administrator of Louisiana Tech Digital Commons. For more information, please contact digitalcommons@latech.edu.

PASSIVE MICROMIXERS AND ORGANIC ELECTROCHEMICAL TRANSISTORS FOR BIOSENSOR APPLICATIONS

by

Senaka Krishna Kanakamedala, B.Tech.

A Dissertation Presented in Partial Fulfillment
of the Requirement for the Degree of
Doctor of Philosophy

COLLEGE OF ENGINEERING AND SCIENCE
LOUISIANA TECH UNIVERSITY

November 2011

UMI Number: 3492487

All rights reserved

INFORMATION TO ALL USERS
The quality of this reproduction is dependent upon the quality of the copy submitted.

In the unlikely event that the author did not send a complete manuscript
and there are missing pages, these will be noted. Also, if material had to be removed,
a note will indicate the deletion.

UMI 3492487
Copyright 2012 by ProQuest LLC.
All rights reserved. This edition of the work is protected against
unauthorized copying under Title 17, United States Code.

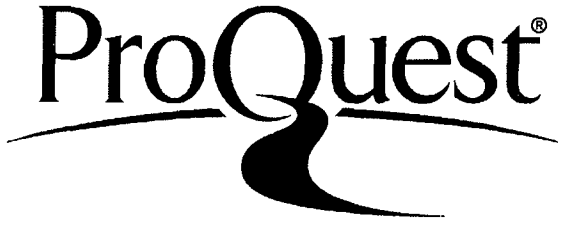

ProQuest LLC
789 East Eisenhower Parkway
P.O. Box 1346
Ann Arbor, MI 48106-1346

LOUISIANA TECH UNIVERSITY

THE GRADUATE SCHOOL

09/26/2011

Date

We hereby recommend that the dissertation prepared under our supervision by SENAKA KRISHNA KANAKAMEDALA

entitled PASSIVE MICROMIXERS AND ORGANIC ELECTROCHEMICAL TRANSISTORS FOR BIOSENSOR APPLICATIONS

be accepted in partial fulfillment of the requirements for the Degree of DOCTOR OF PHILOSOPHY IN ENGINEERING

Supervisor of Dissertation Research

Head of Department

Department

Recommendation concurred in:

Advisory Committee

Approved:

Director of Graduate Studies

Approved:

Dean of the Graduate School

Dean of the College

GS Form 13a
(6/07)

ABSTRACT

Fluid handling at the microscale has greatly affected different fields such as bio-medical, pharmaceutical, biochemical engineering and environmental monitoring due to its reduced reagent consumption, portability, high throughput, lower hardware cost and shorter analysis time compared to large devices. The challenges associated with mixing of fluids in microscale enabled us in designing, simulating, fabricating and characterizing various micromixers on silicon and flexible polyester substrates. The mixing efficiency was evaluated by injecting the fluids through the two inlets and collecting the sample at outlet. The images collected from the microscope were analyzed, and the absorbance of the color product at the outlet was measured to quantify the mixing efficacy. A mixing efficiency of 96 % was achieved using a flexible disposable micromixer.

The potential for low-cost processing and the device response tuning using chemical doping or synthesis opened doorways to use organic semiconductor devices as transducers in chemical and biological sensor applications. A simple, inexpensive organic electrochemical transistor (OECT) based on conducting polymer poly(3,4-ethyelenedioxythiphene) poly(styrene sulfonate) (PEDOT:PSS) was fabricated using a novel one step fabrication method. The developed transistor was used as a biosensor to detect glucose and glutamate. The developed glucose sensor showed a linear response for the glucose levels ranging from 1 μM-10 mM and showed a decent response for the glucose levels similar to those found in human saliva and to detect glutamate released from brain tumor cells. The developed glutamate sensor was used to detect the glutamate re-

leased from astrocytes and glioma cells after stimulation, and the results are compared with fluorescent spectrophotometer. The developed sensors employ simple fabrication, operate at low potentials, utilize lower enzyme concentrations, do not employ enzyme immobilization techniques, require only 5 μL of both enzyme and sample to be tested and show a stable response for a wide pH ranging from 4 to 9.

APPROVAL FOR SCHOLARLY DISSEMINATION

The author grants to the Prescott Memorial Library of Louisiana Tech University the right to reproduce, by appropriate methods, upon request, any or all portions of this Dissertation. It is understood that "proper request" consists of the agreement, on the part of the requesting party, that said reproduction is for his personal use and that subsequent reproduction will not occur without written approval of the author of this Dissertation. Further, any portions of the Dissertation used in books, papers, and other works must be appropriately referenced to this Dissertation.

Finally, the author of this Dissertation reserves the right to publish freely, in the literature, at any time, any or all portions of this Dissertation.

Author K Senakakeishme

Date 10/21/2011

GS Form 14
(5/03)

DEDICATION

To my

Mother, Lokeswari Kanakamedala;

Father, Ramakoteswar Rao Kanakamedala;

Brother, Hari Prasad Kanakamedala; Sister-in-law, Vani Kanakamedala;

Brother, Vijay Krishna Kanakamedala; Sister, Jaya Lakshmi Kanakamedala;

and

Nephew, Jathin Chowdary Kanakamedala.

TABLE OF CONTENTS

ABSTRACT iii

DEDICATION vi

LIST OF TABLES xii

LIST OF FIGURES xiii

ACKNOWLEDGEMENTS xviii

CHAPTER 1 INTRODUCTION 1

1.1 Introduction to Microfluidics 1

1.1.1 The Physics of Microfluidics 1

1.1.2 Fabrication Technologies 5

1.1.2.1 Micromachining 5

1.1.2.2 Soft lithography 5

1.1.2.3 Stereo lithography 6

1.1.2.4 Laser ablation 7

1.1.2.5 Hot embossing 7

1.1.2.6 Microthermoforming 8

1.1.2.7 Injection molding 9

1.1.2.8 Xurography 10

1.2 Introduction to Organic Electronics 10

1.2.1 Fabrication Methods 11

1.2.2 Sensor Applications 12

1.3 Motivation of the Project 13

1.4 Organization of Dissertation 13

CHAPTER 2 PASSIVE MICROMIXERS 15

2.1 Literature Review 15

2.1.1 Introduction to Micromixers 15

2.1.2 Classification of Micromixers 16

2.1.2.1 Active micromixers 17

2.1.2.1.1 Pressure field disturbance. 17

2.1.2.1.2 Electrohydrodynamic, dielectrophoretic, electrokinetic and magneto hydrodynamic disturbances 18

2.1.2.1.3 Acoustic and thermal disturbance 19

2.1.2.2 Passive micromixers 20

2.1.2.2.1 Parallel and serial lamination micromixers 20

2.1.2.2.2 Injection micromixers 22

2.1.2.2.3 Micromixers based on chaotic advection 22

2.1.2.2.4 Droplet micromixers 24

2.2 Passive Micromixers on Silicon 25

2.2.1 Fluidic Simulations of Micromixers 25

2.2.1.1 Introduction to simulation tool 26

2.2.1.2 Fluid flow simulation in micromixers 27

2.2.1.2.1 Simulated designs 27

2.2.1.2.2 Simulation results 29

2.2.2 Micromixer Fabrication 37

2.2.3 Test Setup 44

2.2.4 Results and Discussion 45

2.2.5 Quantification of Mixing Efficiency 50

2.3 Flexible Polymer Micromixer 52
2.3.1 Fabrication of Polymer Micromixer 53
2.3.2 Characterization and Mixing Analysis 56
2.3.3 Results and Discussion 57
CHAPTER 3 PEDOT:PSS BASED ELECTROCHEMICAL TRANSISTOR 62
3.1 Conjugated Polymers 62
3.1.1 Conducting Mechanism of Conjugated Polymers 63
3.1.2 Electrochromism in Conducting Polymers 70
3.1.3 Ionic Conduction in Conjugated Polymers 71
3.1.4 Conducting Polymer – PEDOT:PSS 72
3.2 Organic Thin Film Transistors 75
3.2.1 Organic Field Effect Transistor (OFET) 75
3.2.2 Organic Electrochemical Transistor (OECT) 77
3.3 PEDOT:PSS based OECT 79
3.3.1 Fabrication Process 79
3.3.1.1 Substrate cleaning 80
3.3.1.2 Mask preparation 80
3.3.1.3 Oxygen plasma treatment 80
3.3.1.4 Polymer deposition 81
3.3.1.5 Polymer annealing and stripping 81
3.3.1.6 Preparing polymer wells 82
3.3.2 OECT Device Description and Dimensions 83
3.3.3 Polymer Well Effect on Film Conductivity 85
3.3.4 OECT Characteristics 86

3.3.5 Device Stability Test 91
3.3.6 Effect of pH on OECT Characteristics 92
CHAPTER 4 OECTS FOR BIOSENSOR APPLICATIONS 93
4.1 Introduction to Biosensors 93
4.1.1 Classification of Biosensors 94
4.1.1.1 Calorimetric biosensors 95
4.1.1.2 Optical and piezoelectric biosensors 95
4.1.1.3 Electrochemical biosensors 95
4.1.1.3.1 Conductometric and potentiometric biosensors 96
4.1.1.3.2 Amperometric biosensors 96
4.2 Glucose Sensor 97
4.2.1 Literature Review 97
4.2.2 Micromolar Glucose Sensor 98
4.2.2.1 Materials and methods 99
4.2.2.2 Glucose sensor working principle 100
4.2.2.3 Results and discussion 101
4.3 Glutamate Sensor 106
4.3.1 Literature Review 106
4.3.2 Micromolar Glutamate Sensor 109
4.3.2.1 Materials and methods 109
4.3.2.1.1 Reagent preparation 109
4.3.2.1.2 Cell culture 110
4.3.2.1.3 Methods 111
4.3.2.2 Glutamate sensor working mechanism 112
4.3.2.3 Results and discussion 112

4.3.2.3.1 Control tests 114

4.3.2.3.2 Glutamate sensing 117

4.3.2.3.3 Glutamate release from brain cell stimulation 119

CHAPTER 5 CONCLUSIONS AND FUTURE WORK 126

5.1 Conclusions 126

5.2 Future Work 128

APPENDIX A CELL PREPARATION AND CELLULAR MEDIAS 130

A.1 Cellular Medias 131

A.1.1 Preparation of CRL-2303 (glioma cells) Media 131

A.1.2 Preparation of Astrocytes Media 131

A.2 Preparation of 24 Well Cell Plate 132

REFERENCES 133

LIST OF TABLES

Table 2.1 Properties of water and ethanol at 20 °C 30

Table 2.2 ICP etching parameters. 41

Table 3.1 Conductivities of ITO, PEDOT:PSS, and treated PEDOT:PSS films [125]. ... 74

Table 3.2 Micro-RIE parameters for oxygen plasma treatment..... 80

Table 4.1 Chemicals used in OECT based glucose sensor. 100

Table 4.2 Chemicals used in OECT based glutamate sensor..... 111

LIST OF FIGURES

Figure 1.1 (a) Fluid element that is rounding the corner loses the momentum (b) Fluid element flowing through a contracting channel gains the momentum [2] 3

Figure 1.2 Two fluids are brought together at T-junction to flow alongside down the channel [2] 4

Figure 1.3 Schematic of PDMS casting process [8] 6

Figure 1.4 Schematic of microthermoforming process [7] 9

Figure 1.5 OTFT circuit fabricated on flexible plastic substrate [18] 11

Figure 2.1 Classification of micromixers [27] 17

Figure 2.2 Pressure field disturbance schemes (a) serial segmentation using micro-pump (b) flow velocity generation along the channel (c) integrated magnetic microstirrer in the microchannel [28] 18

Figure 2.3 (a) Electrohydrodynamic disturbance by placing electrodes on the channel (b) dielectrophoretic disturbance in the chamber (c) electrokinetic disturbance in the chamber and (d) electrokinetic disturbance in the channel [28].. 19

Figure 2.4 Parallel lamination micromixers (a) parallel lamination concept (b) hydraulic focusing concept [28] 21

Figure 2.5 Serial lamination techniques [27] 22

Figure 2.6 Chaotic advection based micromixers (a) cylindrical obstacles in the channel (b) modified Tesla structure (c) L-shape microchannel (d) staggered-herringbone grooves [28] 23

Figure 2.7 Simulated micromixer designs 28

Figure 2.8 Dimensions of the simulated designs 29

Figure 2.9 Fluid flow in omega channels 31

Figure 2.10 Stream line traces in omega channel micromixer 31

Figure 2.11 Vorticity contours of designs 1 (a) and (b) 32

Figure 2.12 Velocity magnitude of the fluid flow in design 2 (b); (a) At the inter-section of the two fluids (b) in the middle of the channel 33

Figure 2.13 Mixing phenomenon observed in designs 2 (a) and 2 (b) 35

Figure 2.14 Velocity magnitude of design 3 (a) 36

Figure 2.15 Velocity magnitude of design 4 (a) 36

Figure 2.16 Mixing of two colors (fluids) in design 3 (a) 37

Figure 2.17 Mixing of two colors (fluids) in design 3 (b) 37

Figure 2.18 Primer spin coating parameters 38

Figure 2.19 PR 1813 coating parameters 39

Figure 2.20 Schematic illustrations of micromixer fabrication process steps 43

Figure 2.21 Fabricated micromixers (a) straight channels with "binomial tree" inlet and outlet section (b) omega channel with "binomial tree" inlet and outlet sections (c) omega channel with "T" inlet junction (d) omega channel with "intermediate stage" 44

Figure 2.22 Test setup of micromixer 45

Figure 2.23 Straight channel micromixer testing results 46

Figure 2.24 Fluid distribution in omega channel micromixer with "binomial tree" inlet section 46

Figure 2.25 Fluid distribution in the binomial tree inlet section 47

Figure 2.26 Micro-mixer with T-inlet section (left) and inlet design with more omega channel for initial mixing of the two fluids (right) 48

Figure 2.27 Fluid distribution in T-inlet omega channel micromixer 48

Figure 2.28 Modified inlet section (left) and initial mixing observed at the inlet section (right) 49

Figure 2.29 Circular flow at the intermediate stage (left) and mixing at the junction (right) 50

Figure 2.30 Measuring RGB values at inlet (left) and outlet (right) section 51

Figure 2.31 (a) Solid works model of the polymer micromixer (Top view) (b) Three layered polymer patterns constitute microchannel of the micromixer (Top view) 52

Figure 2.32 The process steps involved in polymer micromixer fabrication 54

Figure 2.33 Fabricated flexible polymer micromixers 55

Figure 2.34 The inlet (left) and outlet (right) sections of the polymer micromixer 56

Figure 2.35 Formation of pink color product at (a) inlet T-junction (b) near inlet junction (c) middle of the channel (d) near outlet section 57

Figure 2.36 Mixing index vs Reynolds number (*Re*). The *Re* mentioned here is the *Re* calculated at the inlet T-junction 58

Figure 2.37 Testing results obtained from repeatability test 59

Figure 2.38 Mixing index vs bending angle 60

Figure 2.39 GOx activity measured in microchannels 61

Figure 3.1 Chemical structures of (a) polyethylene (b) polyacetylene [75] 63

Figure 3.2 Formation of σ and π-bonds due to the overlapping of $2sp^2$ and $2p_z$ orbitals [77] 64

Figure 3.3 (a) Trans-polyacetylene, (b) cis-polyacetylene [15] 65

Figure 3.4 Conductivities of few organic and inorganic materials [75] 66

Figure 3.5 Solitons in degenerate conjugated polymers [84] 68

Figure 3.6 Positive polaron and bipolaron formation and energy levels of the neutral polymer, a polaron, a bipolaron, and bipolar energy bands in PEDOT [88] . 69

Figure 3.7 Schematic representation of optical transmission with the increasing doping level from left to right [84] 71

Figure 3.8 Various applications for PEDOT 72

Figure 3.9 Chemical structure of PEDOT:PSS [124] 73

Figure 3.10 Typical architecture of organic field effect transistor (OFET) [22] 76

Figure 3.11 (a) FET operation with the application of gate and drain voltages (b) transistor characteristics of FET [22] 77

Figure 3.12 Schematic illustration of typical OECT [73] 78

Figure 3.13 Schematic illustration of OECT fabrication (a) Pretreat substrate (b) fasten patterned polyimide tape (c) strip patterned region (d) spin coat PEDOT:PSS (e) peel unwanted tape (f) fasten polymer well (g) final device with electrolyte solution 79

Figure 3.14 Parameters for polymer coating 81

Figure 3.15 PEDOT:PSS film surface profile 82

Figure 3.16 Polymer well preparation (a) attach double sided tape to polyester sheet (b) pattern the polymer sheet (c) remove unwanted region (d) strip the well from polymer sheet 83

Figure 3.17 Fabricated organic electrochemical transistor on glass slide (left) and polyester sheet (right). The overall dimensions of the device are 9 × 11 mm 84

Figure 3.18 Three-dimensional schematic of final device 85

Figure 3.19 Deviation in drain current for various V_{ds} at V_{gs} = 0.2 V 86

Figure 3.20 Micromanipulator electrical probe station and OECT measurement setup (inset) 87

Figure 3.21 Transfer characteristics (I_{ds}-V_{gs}, V_{ds} = -0.4 V) of OECT measured in 1 × tris electrolyte solution 89

Figure 3.22 Output characteristics of OECT measured at various gate potentials 90

Figure 3.23 OECT drain current as a function of drain potential over several days 91

Figure 3.24 Transistor response vs pH. The pH sensitivity of the drain current curve (y-axis) at different gate potentials (V_{gs}) , is shown for three different pH values 92

Figure 4.1 Schematic diagram of biosensor 94

Figure 4.2 Schematic of electron transfer in electrochemical biosensors (a) non-mediated (b) mediated electron transfer [151] 96

Figure 4.3 Schematic of OECT based glucose sensor (top view) 99

Figure 4.4 Reaction cycle of PEDOT:PSS based glucose sensor 101

Figure 4.5 Application of gate bias (solid line) resulted in reversible modulation in drain current (I_{ds}) (dotted line) 102

Figure 4.6 Relative response of I_{ds} as a function of V_{ds} under different glucose concentrations 103

Figure 4.7 Selectivity test to observe the drain current deviation in the presence of glucose and glutamate 104

Figure 4.8 Normalized response (NR) of the device for various glucose concentrations. NR is getting saturated after 10 mM glucose concentrations 106

Figure 4.9 OECT based glutamate sensor (top view) 109

Figure 4.10 Applied gate bias (solid line) causes reversible modulation in drain current (dotted line) 114

Figure 4.11 The shift in the drain current curve with the addition of GluOx to the glutamate containing well at various gate potentials 115

Figure 4.12 The deviation in the drain current with the successive addition of glutamate and GluOx as function of time 116

Figure 4.13 Downward shift in the drain curve with the successive addition of higher glutamate concentrations to the same device as a function of drain voltage 117

Figure 4.14 Normalized response of the sensor as function of glutamate concentration. 119

Figure 4.15 Effect of stimulating agents on drain current. Minimal downward shift in the drain current in the presence of (a) ATP, (b) KCl and (c) cystine 121

Figure 4.16 The minimal OECT response for stimulating chemicals (negative controls) 122

Figure 4.17 Detected glutamate release from brain tumor glioma cells 123

Figure 4.18 Detected glutamate release from astrocytes 123

Figure 5.1 Reactivation of Apo-GOx with various FAD concentrations 129

ACKNOWLEDGEMENTS

I wish to express my deepest gratitude to my mentor and advisor, Dr. Mark DeCoster, for his constant advice, support and encouragement in technical and professional aspects of my research work. I am thankful to members of my advisory committee, Dr. Yuri Lvov, Dr. Eric Guilbeau, Dr. Shengnian Wang and Dr. Niel Crews for their valuable advice in my research.

I especially thank Dr. Kody Varahramyan and Dr. Yuri Lvov for giving me an opportunity to be a part of this exciting research project at one of the finest research institutions in the world. I would like to express my sincere thanks to Dr. Mangilal Agarwal and Mr. Ji Fang for their continued support, guidance and encouragement as well as insight and experience through the course of this research work. I am thankful to Ms. Katharine Hamlington, Dr. Mehnaaz Ali, and Dr. Diane Blake for their collaboration. I would like to acknowledge the experimental resources made available by the Institute for Micromanufacturing (IfM), Center for Biomedical Engineering and Rehabilitation Science (CBERS) and the professors concerned with my experimental work. I especially thank the IfM staff, Dr. Alfred Gunasekaran, Mr. Philip Coane, Mr. Donald Tatum, Ms. Deborah Wood, Mr. John McDonald, Ms. Jeanette Futrell, Ms. Sharon Ellis, and the late Mr. Scott Williams for their support at various stages of my project.

I am thankful to my group members, Mr. Haidar Alshakhouri, Ms. Kinsey Cotton, Dr. James McNamara, Ms. Jessica Wasserman, Ms. Sowgandhi Maddi, Mr. Ruturaj Masvekar, Mr. Dustin Green, Ms. Chitra Jeyasankar, Mr. Bharat Karumuri, Mr. Vivek Datta, Mr. Chaitanya Joshi, Ms. Sneha Deodhar, and Ms. Charuta Agashe for their support and friendship. I would like to thank my seniors, Dr. Sudhir Shrestha, Dr. Jie Liu, and Dr. Deeba Balachandran for their guidance during the initial stages of my research work. I am very thankful to my colleagues Mr. Ilija Pjescic, Dr. Raja Mannam, Mr. Venu Kotipalli, Mr. Wajihuddin Mohammad, Dr. Joel Soman, Ms. Manasa Paidipalli, Dr. Bobby Mathew, Dr. Tom John, and Mr. Gong for their suggestions and encouragement. Not, but not least, I would like to thank my family and friends for their inspiration, continued support and encouragement.

CHAPTER 1

INTRODUCTION

Microfluidics and organic electronics possess several applications in common. The development and integration of microfluidic devices such as micromixers and organic electronic devices such as organic electrochemical transistors (OECT) using low cost and rapid fabrication technologies will have potential applications in biomedical field, especially for biosensors in point of care analysis.

1.1 Introduction to Microfluidics

Fluid handling at the microscale has greatly affected different fields and has led to a new concept, called microfluidics. Microfluidics is a field of plumbing and manipulating fluids at a micro scale region to provide the solutions for outstanding system integration issues of chemistry and biology. It is assumed that this field may automate biology and chemistry to an extent where the current integrated circuit revolution automated the computation. The applications of microfluidics can be extended to biology, chemistry, medicine, energy generation, heat management, control systems, and display technologies. Commercially available liquid crystal displays (LCDs) and ink jet printers can be considered as microfluidic devices [1, 2].

1.1.1 The Physics of Microfluidics

Fundamental physical effects change more rapidly in microfluidics than that of microelectronics as the size is diminished. For example, viscous forces dominate the

inertial forces and the mass transport of the fluid is generally laminar at microscale, i.e., the physics of the fluid flow differs from macroscale. In fact, microfluidic physics draws attention from different classical physics and chemistry such as thermodynamics, electrostatics, statistical mechanics, fluid mechanics, fluid dynamics, polymer physics, and elasticity [1, 2].

Fluids are continuum materials and are made of molecules. The velocity field of a Newtonian fluid obeys the Navier-Stokes equations and is given by Eq. 1.1:

$$\rho\left(\frac{\partial u}{\partial t}+u\cdot\nabla u\right)=\nabla\cdot\ddot{\sigma}+f=-\nabla p+\eta\nabla^2u+f\,, \tag{1.1}$$

where f denotes body force densities. The left side of the equation represents the inertial acceleration terms, and the right side represents the forces. In microfluidics, inertial forces are small compared to the viscous forces, so the nonlinear term can be avoided resulting in the following Stokes Eq. 1.2:

$$\rho\frac{\partial u}{\partial t}=\nabla\cdot\sigma+f=-\nabla p+\eta\nabla^2u+f\,. \tag{1.2}$$

Figure 1.1 depicts fluid flow through a microchannel that takes an instant right turn and a microchannel with contracting width. In the first case, fluids flow with a certain velocity through a microchannel of a certain width undergoes an unexpected right turn. A fluid element rounding the corner exerts an inertial centrifugal force density f_i and loses momentum density during the turn time. Due to this curved stream line, fluid inertial forces points outwards centrifugally. In the second case, fluids flow through a contracting channel and attain a higher momentum. Despite the direction of fluid flow, inertial force points towards the wide end of the channel.

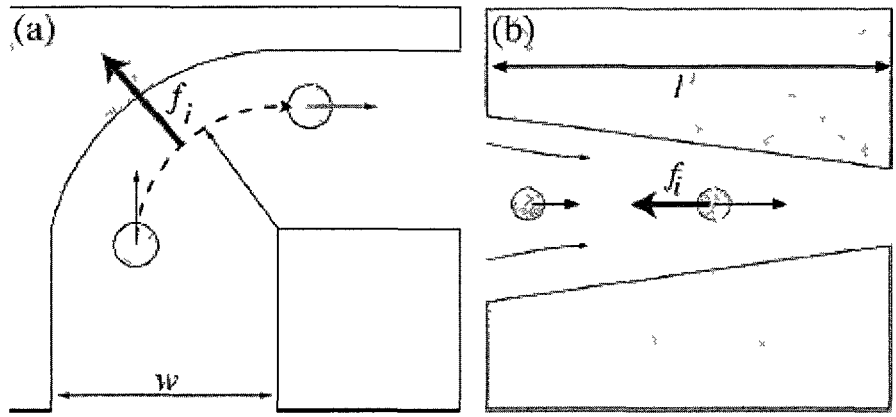

Figure 1.1 (a) Fluid element that is rounding the corner loses the momentum (b) Fluid element flowing through a contracting channel gains the momentum [2].

Inertial and viscous force densities and their magnitudes have to be accounted for both cases. The ratio of inertial forces to viscous force densities is known as Reynolds number (*Re*) and is described in Eq. 1.3:

$$\mathrm{Re} = \frac{\rho U_0 L_0}{\eta}, \tag{1.3}$$

where ρ is the density of fluid, U_0 is velocity scale, L_0 is generic length scale, and η is shear viscosity. The Reynolds number ranges between in the order of 10^{-6}-10 in a typical microfluidic device with water as the working fluid, with velocities and channel radii in the ranges of 1 μm/s-1 cm/s and 1-100 μm, respectively. These values confirm the domination of viscous forces over inertial forces in the microscale region and result in a laminar flow. As *Re* increases, a secondary flow is generated in a circular channel driven by the centrifugal forces on the fluid. This results in an unpredictable and irregular turbulent flow in the macroscale [2].

In high Reynolds number world, turbulent mixing happens due to the random eddies and secondary flows. In low *Re* world, diffusion is the only phenomenon behind fluid mixing resulting in long mixing times on the order of minutes. Some microfluidic

applications demand rapid mixing by different approaches rather than a time consuming diffusion based mixing. Figure 1.2 depicts a simple T-junction, in which two different fluids were injected. Diffusion based mixing takes place at the intersection of the two fluids and it increases as the fluids flow down the channel as depicted in yellow in Figure 1.2.

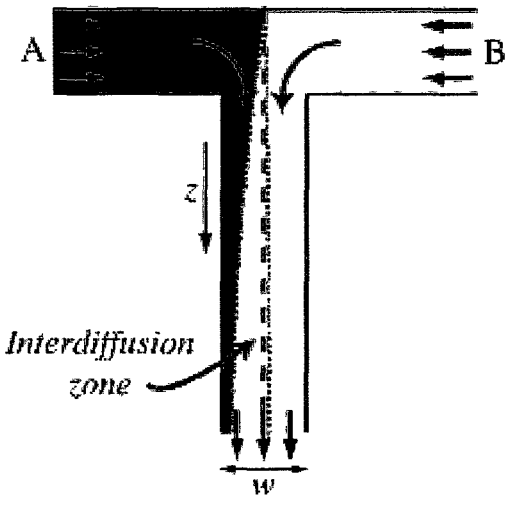

Figure 1.2 Two fluids are brought together at T-junction to flow alongside down the channel [2].

How far the fluids must flow to attain a complete mixing across the channel is expressed using the Péclet number (*Pe*). It is defined as the ratio of convection to diffusion and is described in Eq. 1.4:

$$Pe = \frac{U_0 w}{D}, \tag{1.4}$$

where w is channel width, D is diffusivity, and U_0 is velocity scale. In general, a small protein flowing through a 100 μm wide channel with a 100 μm/s velocity requires a *Pe* of 250 channel widths approximately to mix completely [1-5].

1.1.2 Fabrication Technologies

Micromachining, soft lithography, stereo lithography, laser ablation, hot embossing, microthermoforming, injection molding, and xurography are currently available techniques for microfluidic device fabrication. The suitable method for device fabrication is chosen depending on the specific application [6].

1.1.2.1 Micromachining

Silicon micromachining is one of the earliest technique applied to microfluidic device fabrication. The microchannels can be created by using photolithography and wet/dry etching techniques depending on the application. Recent advancements in this technique can be used to create nanometer structures. However, many microfluidic applications do not require this precision [6].

1.1.2.2 Soft lithography

Soft lithography or elastomeric material casting is one of the widely used process for generating polymeric microstructures owing to easy processing, low cost, and high replication accuracies. There are different casting processes available, such as microcontact printing (μCP), microtransfer molding (μTP), replica molding, solvent-assisted micromolding (SAMIM), and micromolding in capillaries (MIMIC). The casting process is depicted in Figure 1.3. It starts with mixing ten parts of base elastometer with one part of curing agent to produce an optically transparent, chemically inert and electrically insulating elastometer. The polymer mixture is then poured onto the master mold and is cured. The stiffness of the elastometer depends on the ratio of the curing agent and the curing temperature. The elastometer is simply peeled away from the master mold after curing. Polydimethylsiloxane (PDMS) can be easily bonded to glass or other PDMS sheet using

oxygen plasma treatment for 10-30 s. The accuracy of this replication process is very high and 10 nm featured size structures have been reported [7, 8].

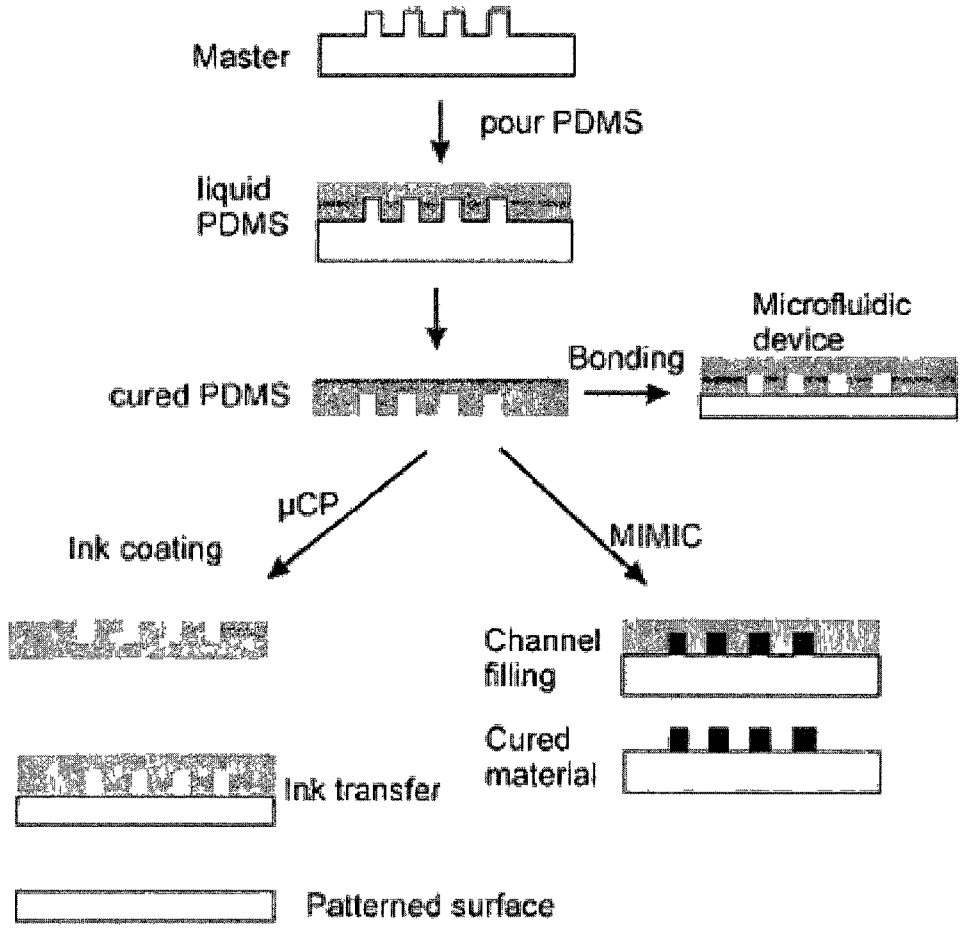

Figure 1.3 Schematic of PDMS casting process [8].

1.1.2.3 Stereo lithography

Stereo lithography is one of the well established rapid prototyping techniques in the macroworld. It uses liquid resin that is exposed to two high intensity light beams using laser sources. When the two beams meet at a certain location, the generated light intensity is sufficient to cross-polymerize the photoresist. The process is simple, and the first device can be produced very fast using this method; however, it suffers from several

disadvantages such as serial device fabrication rather than batch processing, relatively high surface roughness and limited choice of materials [8, 9].

1.1.2.4 Laser ablation

Laser ablation uses a high intensity laser beam to create required geometry either by exposing the substrate through the mask or by moving either the substrate or the laser beam in x and y directions to produce the desired pattern on the substrate. In both cases, high intensity focused laser beam ablates a certain amount of material, typically 1 μm per laser shot, depending on laser intensity, wavelength and material wavelength. Deeper structures require several shots leading to a characteristic surface roughness and the ablated material is removed by suitable means. Laser ablation is generally used to structure thermoset polymers. Exposure of intense laser beams to the substrate alters the surface chemistry and surface charge. So laser ablation is not recommended to fabricate devices for surface sensitive applications such as electrokinetic transport systems [8, 10].

1.1.2.5 Hot embossing

Simple processing, a large range of suitable materials, low master structure requirements, high replication accuracy, and commercially available instrumentation make hot embossing one of the most widely used techniques for polymeric microstructure fabrication. The process starts with loading the polymer substrate in the system and heating it to a temperature above the glass transition temperature in a vacuum along with the master structure. Depending on the design, master material and polymer material, the master structure is pressed into the polymer with certain force. Later, the master and polymer substrate are cooled below the transition temperature [8, 11].

1.1.2.6 Microthermoforming

Microthermoforming is very simple and the structures can be created rapidly although it suffers from limited accuracy in structure replication, ability to create sharp angles, and high aspect ratio structures compared with the hot embossing method. Generally, this method is used for producing thin walled plastic devices. Typically, 50 μm thin polymer foil is clamped in the mold tool that has microstructure on one side as depicted in Figure 1.4. Later, the polymer foil is heated 10 °C above transition temperature followed by pressing into the master mold using compressed gas. Then the polymer structure is cooled down to 20 °C below transition temperature to achieve the required polymer microstructure [7-8, 12].

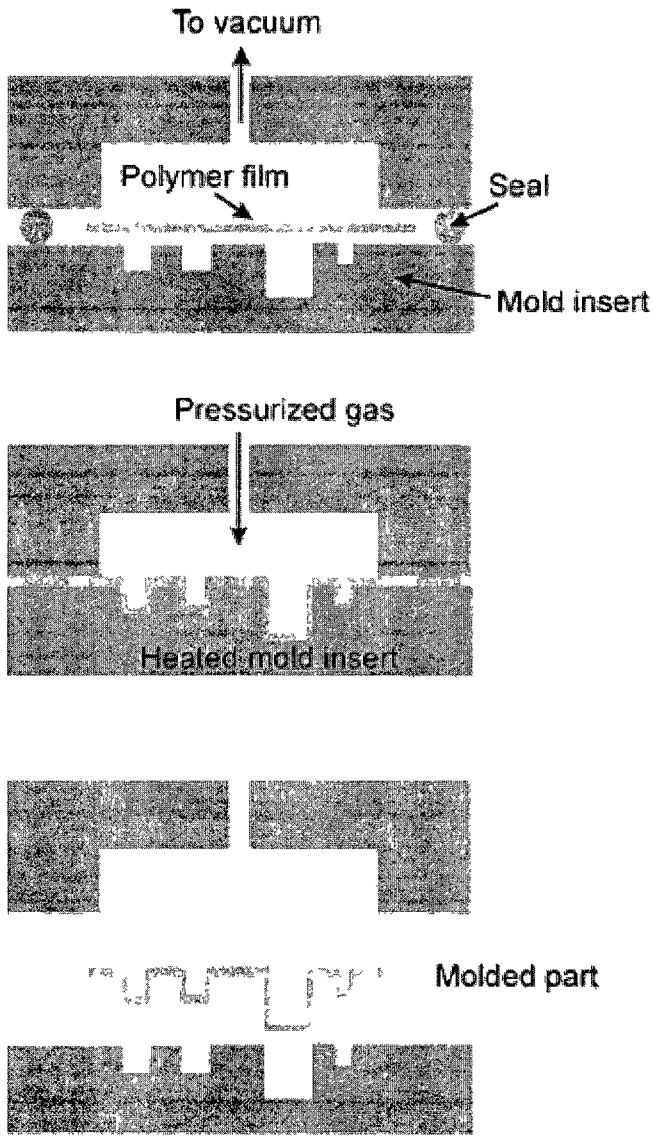

Figure 1.4 Schematic of microthermoforming process [7].

1.1.2.7 Injection molding

For injection molding, the polymer material that has to be microstructured should be in the form of pre-dried granules. The ability to produce three-dimensional objects and the rapid production time are the major advantages of this process; however, it suffers from various disadvantages such as the complex process, thermally stable complex mold requirement, and less replication accuracy [8, 13].

1.1.2.8 Xurography

D.A. Bartholomeusz et al. [14] first reported xurography technique to fabricate microfluidic structures in various films. The word *xurography* was derived from Greek root words Xuron (razor) and graphē (writing). This inexpensive rapid prototyping technique uses a cutting plotter, which is generally used to cut the graphics in adhesive vinyl films. This computer-controlled cutting plotter cuts the films of different thicknesses ranging from 25 μm-1000 μm, according to the specific design with a resolution of 10 μm. Several polymer films can be attached together after microstructuring to create 3-D layered channels [14].

1.2 Introduction to Organic Electronics

The discovery of conduction in polymer materials in 1977 opened the doors for organic electronics [15]. During the past few decades, several conductive polymer based devices such as field effect transistors, rectifiers, sensors and light emitting diodes (LEDs) were developed using simple fabrication techniques such as drop casting, spin coating, ink-jet printing and self assembly [16, 17]. Among all the developed devices, organic thin film transistors (OTFTs) have attracted a great deal of attention for sensor applications such as humidity sensor, hydrogen peroxide sensor, and glucose sensors. Figure 1.5 depicts the circuit made of OTFTs on a plastic substrate.

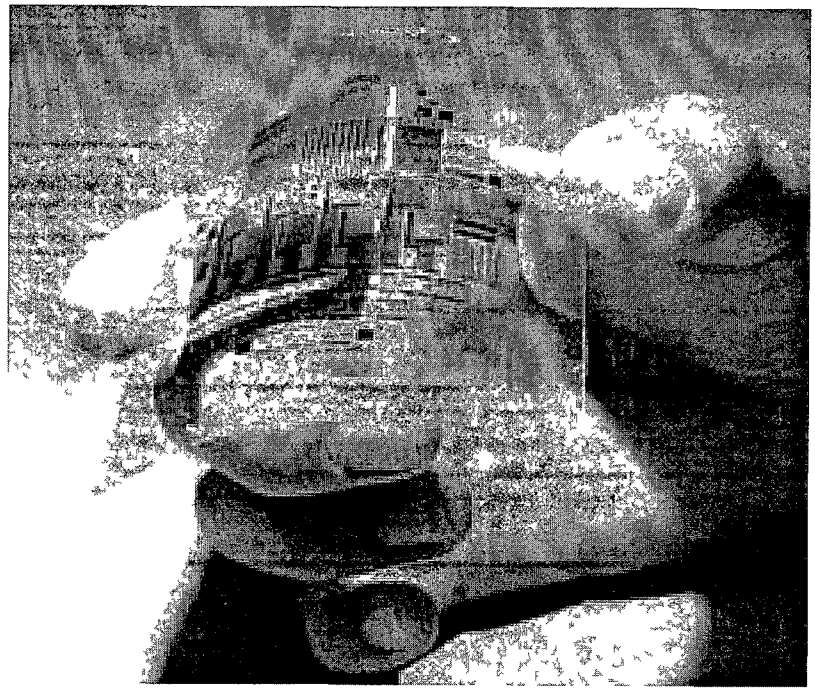

Figure 1.5 OTFT circuit fabricated on flexible plastic substrate [18].

1.2.1 Fabrication Methods

The organic electronic structures can be obtained by high speed, low cost and simple fabrication methods such as drop-casting, spin coating, layer-by-layer (LBL) self assembly and ink-jet printing in addition to tedious micromanufacturing techniques. In all of these mentioned fabrication methods, polymer is dissolved either in water or in organic solvent.

In the drop-casting technique, a drop of polymer solution is dropped onto a substrate, and later it was dried or annealed at certain temperatures to attain a polymer film in between the electrodes. Though it is a simple technique, the films obtained in general are not uniform and the film thickness is only controlled by changing the polymer concentration.

Spin coating is the most common fabrication process to get uniform thin films. In this method, a small volume of fluid is deposited onto the center of the substrate and is spun at high speeds to spread it all over the substrate. Later, the substrate is annealed to get uniform thin films. The thickness of the deposited films depend on the concentration of the polymer solution, viscosity of the solution, spinning speed, surface tension, and drying rate.

Layer-by-Layer self assembly is one of the promising technologies to achieve ultra thin uniform films in the range of nanometers. The alternating layers of polycations and polyanions are deposited onto the surface of the substrate using dip-coating and spray-coating techniques. Different hierarchical order of materials can be deposited by changing the order of dipping or spraying solutions [19, 20].

Recently, ink-jet printing is gaining a lot of attention in printing the electronic structures and is one of the main contenders for field emissions, flat screen displays, and light emitting diode fabrication processes. There are two approaches in ink-jet printing technique; one is the "Continuous, Charge and Deflect" method that deflects a 0.5 mm drop. The second one is "Drop-on-Demand (DOD)", which is used for small drops in the range from 20 μm-100 μm [21].

1.2.2 Sensor Applications

Recently, conducting polymers are attracting a lot of attention in biological and chemical sensor developments. OTFTs are promising devices for sensor applications, as they are aqueous compatible, can be operated at low potentials, and can be fabricated using low cost rapid fabrication techniques. OTFTs are dividend into organic field effect transistors (OFETs) and organic electrochemical transistors (OECTS) and use different principles to detect the analytes. In OFETs, the applied electric field across an insulating

layer modulates the transistor channel current. In OECTs, the channel current is modulated by the electrochemical doping/dedoping of the polymer material and is discussed in detail in Chapter 4. The analyte can be detected by either direct analyte-semiconductor interactions or indirect receptor (immobilized on the surface) interactions [22, 23].

1.3 Motivation of the Project

Recently, much effort is made to develop biosensors, particularly to detect lower molecular weight reagents. The rapid increase in deadly diseases, pollutants, and chemical warfare agents around the globe greatly demands highly sensitive and selective onsite sensors [24]. High specificity and sensitivity of antibodies and the technology of producing antibodies against any particular organic compounds made immunosensors as the obvious choice [25]. Most currently available immunosensors are designed to detect high molecular weight molecules (primarily proteins and infectious agents), and chemical agents of small sizes remain very difficult to detect. Thus, the development of a simple, low cost Lab-On-a-Chip (LOC) device consisting of passive micromixers and polymer based biosensor for immunosensor applications is required.

1.4 Organization of Dissertation

The dissertation is organized into five chapters. Overview on micromixers, simulation, fabrication and characterization of various passive micromixers on silicon, and the development of flexible passive micromixer are demonstrated in Chapter 2. The introduction to conducting polymer, literature review on organic thin film transistors (OTFT), development of organic electrochemical transistor (OECT), and the fabricated device characteristics are presented in Chapter 3. Chapter 4 deals with the development of glucose sensor to detect glucose levels similar to those found in human saliva and micromolar

glutamate sensor to detect glutamate released from astrocytes and glioma cells after stimulation. Conclusion and future work are presented in Chapter 5.

CHAPTER 2

PASSIVE MICROMIXERS

This chapter deals with the design, simulation, fabrication, and characterization of passive micromixers. Various micromixer designs were proposed and the mixers were fabricated on silicon and polyester sheet using micromanufacturing and xurography techniques. The flexible polymer micromixer developed on polyester sheet exhibited a mixing efficacy of 96% at $Re = 1$, and the mixing index was higher than 90% for a wide Reynolds number range. The developed flexible micromixer is biocompatible and was used to mix glucose oxidase and glucose, and the results indicated that the mixing efficiency is higher than the pipette mixing, potentially leading to better biosensors.

2.1 Literature Review

2.1.1 Introduction to Micromixers

Fluid handling and analysis at the microscale has gained a lot of attention during the last two decades. Over the past decade, microfluidic device development greatly affected different fields such as biomedical, pharmaceutical, biochemical engineering and environmental monitoring due to their reduced reagent consumption, portability, high throughput, lower hardware cost, and shorter analysis time compared to large devices. Since then different microfluidic structures have been proposed by considering different factors such as operation principle, device performance, fabrication method, and materials

used. The components of these microfluidic devices include micropump, micromixers, microactuators, and microvalves [4].

Micromixers are one of the important microfluidic systems besides micropump and can work either stand-alone or by integration in a microfluidic system. Several biological, chemical and biochemical processes often require rapid mixing. Micromixers play an important role in cell activation, enzyme reactions, protein folding, drug delivery, biochemistry analysis, and sequencing of nucleic acid [5, 26].

Viscous forces dominate the molecular forces when considering mixing at the microscale. Therefore, it is difficult to generate turbulent flow at this low Reynolds number regime. Thus, the effective mixing in microfluidic devices is challenging due to the laminar and stable flow of the fluids. Transverse flow in microscale can be created by employing various micromixing techniques [28-31] .

2.1.2 Classification of Micromixers

Micromixers are categorized into active and passive micromixers as depicted in Figure 2.1. Active micromixers use an external field to create disturbance in the flow to further enhance the mixing process and are categorized by an external disturbance effect type such as pressure, electrohydrodynamic, electrokinetic, dielectrophoretic, magneto hydrodynamic, thermal, and acoustic effects. The integration of active micromixers in a microfluidic system is challenging and expensive as the fabrication process often involves complicated processes and the mixer operation requires external power sources. Passive micromixers completely rely on molecular diffusion and chaotic advection and do not require external energy. Molecular diffusion can be improved by increasing the contact surface area between two fluids, while chaotic advection can be achieved by using obstructions in the channel by manipulating the laminar flow. Therefore, these are categorized by

the arrangement of mixed phases such as lamination, injection, chaotic advection, and droplet techniques. Passive micromixers are simple, robust and do not require external energy to enhance mixing; thus, it can be easily integrated in a microfluidic system [27, 28].

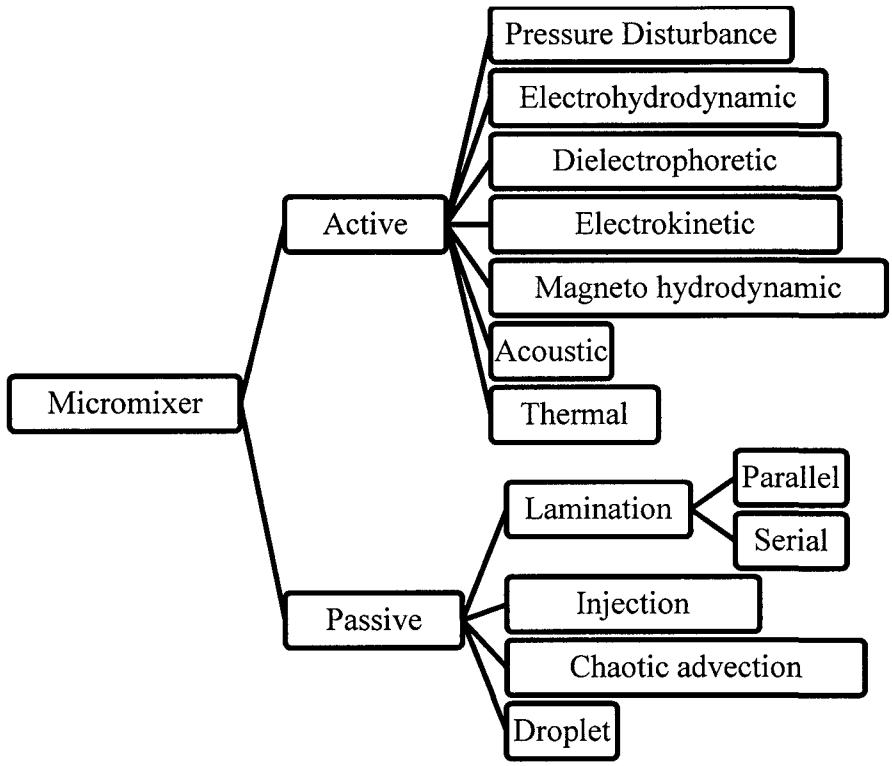

Figure 2.1 Classification of Micromixers [27].

2.1.2.1 Active Micromixers

2.1.2.1.1 Pressure field disturbance. Pressure field disturbance is one of the earliest adopted techniques to achieve mixing in active micromixers. Pressure disturbance was achieved by using micropumps, generating pulsing velocity, and integrating a microstirrer in the channel. Micropump driven pressure disturbance can be achieved either by integrating micropump in a microfluidic system that is fabricated using optical lithography techniques, or by using an external micropump. In this technique, mixing liquids are divided

into serial segments as shown in Figure 2.2 (a) to generate convection independent mixing process by driving and stopping the fluid flow in the microchannel using micropump. In the second technique, pulsing velocities are generated in the channel by pulsing the side flow at a *Re* of 0.3 as depicted in Figure 2.2 (b), and the mixing efficacy is dependent on pulsing frequency and number of mixing units [31-33]. Pressure disturbance can also be achieved by placing a micromachined magnetic stirrer at the intersection of the liquids in a simple T-mixer as shown in Figure 2.2 (c). This rotating stirrer rotates at a speed between 100 rpm and 600 rpm with the application of an external magnetic field [28, 34].

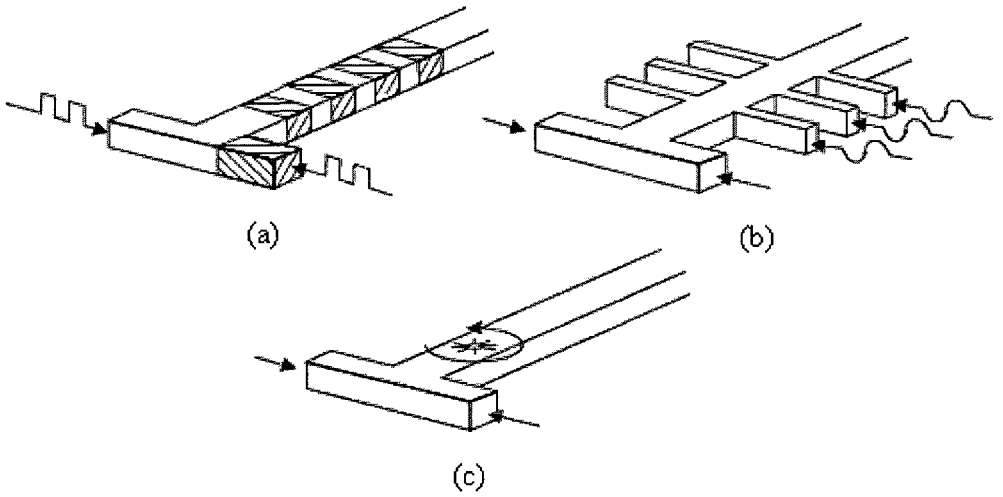

Figure 2.2 Pressure field disturbance schemes (a) serial segmentation using micropump (b) flow velocity generation along the channel (c) integrated magnetic microstirrer in the microchannel [28].

2.1.2.1.2 Electrohydrodynamic, dielectrophoretic, electrokinetic and magneto- hydrodynamic disturbances. A.O. Moctor et al. [35] reported an electrohydrodynamic disturbance based micromixer by placing a series of titanium wires perpendicular to the channel that is 30 mm long, 250 μm wide and 250 μm deep as depicted in Figure 2.3 (a). Voltage and frequency on the electrode were altered to achieve good mixing at a *Re* of 0.02 [28]. Deval et al. [36] and Lee et al. [37] reported micromixers based on

dieelctrophoresis (DEP) phenomenon that moves the particle to and from an electrode by polarizing the particle relative to its surrounding medium in a non-uniform electric field. The local geometry variations and electrically actuated embedded particles correspond to chaotic advection as depicted in Figure 2.3 (b). Several groups have used electrokinetic flow to transport liquid in the channels instead of pressure driven flow and Figures 2.3 (c) and (d) depict micromixers based on electrokinetic disturbance. Mixing liquids were divided into serial segments by turning on or off the applied voltage [38, 39]. In a magneto hydrodynamic disturbance based micromixer, DC voltages applied on the electrodes generate Lorentz forces in the presence of the magnetic field. If the liquids to be mixed are electrolyte solutions, the generated Lorentz force rolls and folds the electrolytes to induce mixing phenomenon in the chamber [28, 40].

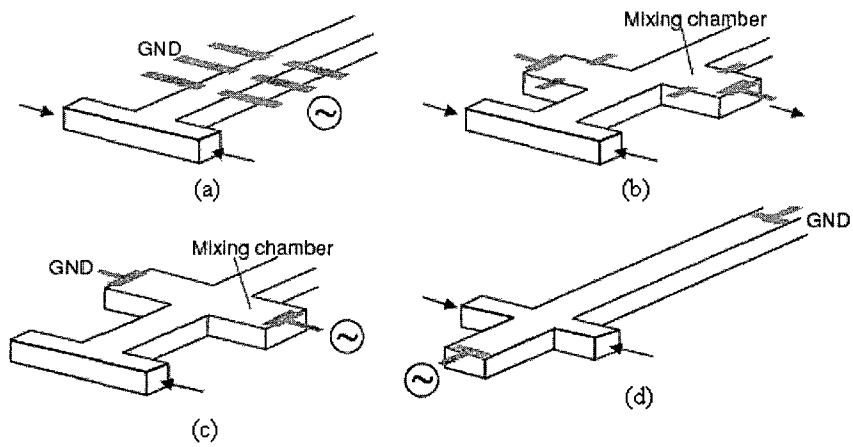

Figure 2.3 a) Electrohydrodynamic disturbance by placing electrodes on the channel (b) dielectrophoretic disturbance in the chamber (c) electrokinetic disturbance in the chamber and (d) electrokinetic disturbance in the channel [28].

2.1.2.1.3 Acoustic and thermal disturbance. Moroney et al. [41] reported acoustic mixing proof of concept with a flexible-plate-wave (FPW) device. Zhu and Kim [42] analyzed focused acoustic wave model and fabricated an acoustic micromixer in silicon with dimensions of 1 mm × 1 mm × 10 μm by placing a zinc oxide membrane at the

bottom of the chamber. The frequency and the voltage of the input signal control acoustic vibrations. Various schemes such as acoustically induced flow focused acoustic streaming and high frequency stirring were employed to realize mixing at microscale. The acoustic energy also raises temperature, and the ultrasonic mixing phenomenon poses problems for highly temperature sensitive biological and chemical sample analysis, and also it may create cavities in the biological samples if the ultrasonic wave is around 50 kHz [28]. Yasuda [43] reported an acoustic micromixer that uses piezoelectric zinc oxide thin film to generate loosely focused acoustic wave for stirring movements. A sinusoidal wave with thickness-mode resonance frequencies of the piezoelectric film such as 240 MHz and 480 MHz was used to drive the actuator, and it was operated without any significant raise in temperature and is compatible for temperature sensitive fluids. Mao et al. [44] demonstrated a temperature gradient across the parallel channels to examine temperature dependence of fluorescent dyes. This technique may possibly be used for micromixing as temperature highly affects the diffusion coefficient [28].

2.1.2.2 Passive micromixers

2.1.2.2.1 Parallel and serial lamination micromixers. A basic T-mixer is dependent on molecular diffusion phenomenon. So, a long mixing channel is required to achieve complete mixing. Chaotic flow and multiple stream lamination result in short mixing lengths at high Reynolds numbers. However, the supply pressure has to be very high to achieve high *Re* that may pose severe problems for bonding and interconnection technologies. Mixing in basic T-design can be enhanced by throttling the channel entrance and roughening the channel [4, 28].

Mixing path can be reduced by narrowing mixing, realizing parallel lamination with multiple streams and hydrodynamic focusing [45-47]. In parallel lamination

technique, multiple streams were laminated parallel to each other to achieve mixing as depicted in Figure 2.4 (a), and the flow can be driven either by pressure or by electro-osmosis [48]. The hydrodynamic focusing based micromixer is made up of a long micro-channel with three inlets, where the middle inlet is the sample and the other two inlets serve as the sheath flows as depicted in Figure 2.4 (b), and this focusing decreases the mixing path by reducing sheath width [28, 49].

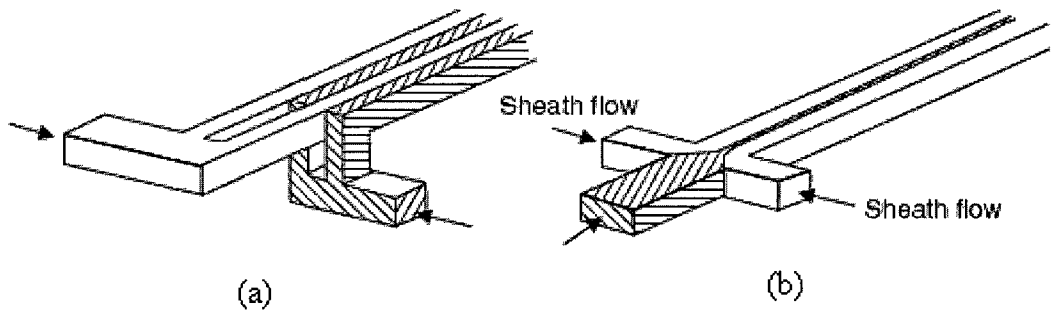

Figure 2.4 Parallel lamination micromixers (a) Parallel lamination concept (b) hydraulic focusing concept [28].

Serial lamination micromixers also increase mixing by splitting and joining the streams as shown in Figure 2.5 similar to parallel lamination micromixers. The inlet streams are joined horizontally followed by vertical joining stage; 2^m liquid layers can be laminated after m splitting and joining stages leading to a 4^{m-1} times enhancement in mixing time [50]. Several groups have developed serial laminated micromixers on silicon using KOH wet etching or deep reactive ion etching (DRIE) technique and using multiple polymer layers. Both electrokinetic flows and pressure driven flows can use the serial lamination concept to enhance mixing [28, 51].

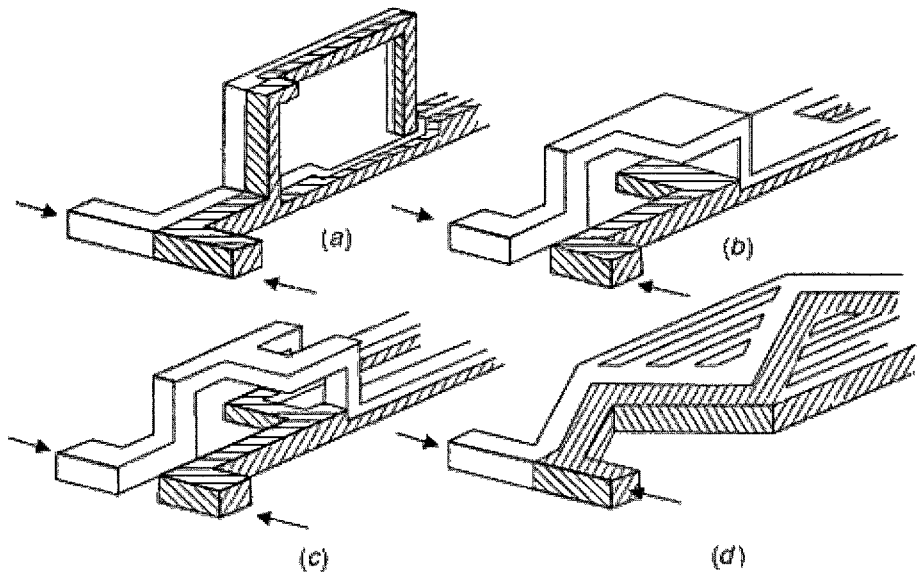

Figure 2.5 Serial lamination techniques [27].

2.1.2.2.2 Injection micromixers. Injection micromixers split the solute flow into many streams followed by injecting them into solvent flow similar to parallel lamination where both inlet flows are divided and then joined. In injection micromixers, a number of solute microplumes are created using an array of nozzles to increase the contact surface area and thus the mixing efficacy. Miyake et al. demonstrated an injection micromixer fabricated on silicon using DRIE that has 400 nozzles arranged in a square array placed in the mixing chamber [28].

2.1.2.2.3 Micromixers based on chaotic advection. At low *Re*, advection plays an important role in mass transfer besides diffusion and is often parallel to the main flow direction. In passive micromixers, chaotic advection is achieved by special channel geometries as shown in Figure 2.6 which split, stretch, fold, and break the flow. Inserting obstacle structures in the mixing channel is one of the simple techniques to achieve chaotic advection. Several arrangements of obstacles were studied and it was found that asymmetric obstacle arrangement alters the flow direction and forces fluids to merge. Lin et al. [52]

demonstrated 50 μm × 100 μm ×100 μm mixing chamber fabricated on silicon. Seven cylinders of diameter 10 μm were located in the narrow channel as depicted in Figure 2.6 (a) to improve the mixing and the mixer showed efficient mixing in between 200-2000 Re. Chaotic advection can also be achieved by periodic steps of zig-zag microchannels to generate recirculation around the turns at high Re. Megneaud et al.[53] fabricated a zig-zag micromixer on a poly ethylene terephthalate (PET) substrate using an excimer laser [28].

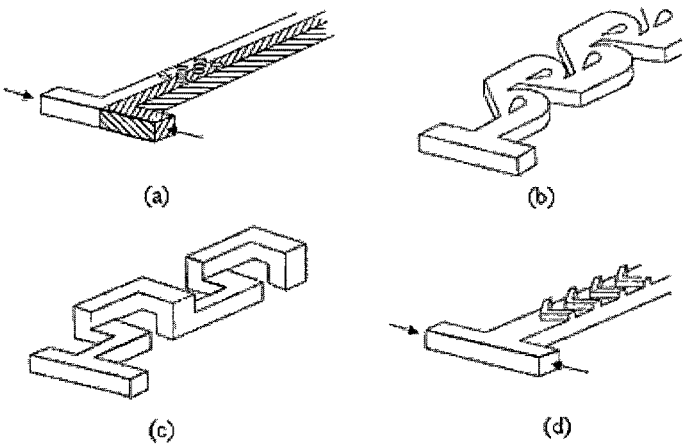

Figure 2.6 Chaotic advection based micromixers (a) cylindrical obstacles in the channel (b) modified Tesla structure (c) L-shape microchannel (d) staggered-herringbone grooves [28].

Hong et al. [54] reported a two-dimensional modified Tesla structure inplane micromixer as depicted in Figure 2.6 (b). It was fabricated on cyclic olefin copolymer (COC) using hot embossing and thermal direct bonding. Chaotic advection is generated by the Coanda effect in the structure and the mixer works well at $Re > 5$. Vijayendran et al. [55] demonstrated a three-dimensional serpentine micromixer fabricated on PDMS as shown in Figure 2.6 (c). The channel consists of a series of L-shaped segments in

perpendicular planes and has a width of 1 mm and a depth of 300 μm and the length of 30 mm. The serpentine mixer was tested at *Re* of 1, 5 and 20 [28].

Rips or grooves on the microchannel wall as depicted in Figure 2.6 (d) can generate chaotic advection similar to macroscale mixers. Johnson et al. [56] first reported a micromixer on polycarbonate sheet (PC) covered with poly ethylene terephthalate glycol (PETG) using excimer laser ablation technique. The channel has 72 μm width at the top, 28 μm width at the bottom and 31 μm depth. The 14 μm wide grooves are ablated on the bottom wall with a center-to-center separation of 35 μm. Stroock et al. [57] studied different groove patterns to generate chaotic advection. Staggered herringbone micromixer works well at *Re* from 1 to 100 [28].

2.1.2.2.4 Droplet micromixers. The generation and transportation of individual droplets can be achieved by pressure or capillary effects such as electrowetting and thermocapillary. However, they can also be generated by creating large difference of surface forces in small channels using multiple immiscible phases such as oil/water or water/gas. The droplet movement creates mixing inside the droplet using the internal flow field. Hosokawa et al.[58] first reported droplet micromixer fabricated in PDMS that uses hydrophobic microcapillary vent to join the two initial droplets. Paik et al. [59] investigated various mixing schemes in which droplets are split and merged repeatedly and the merged droplets are transported using electrowetting concept. Flow instabilities between two immiscible liquids can be used to create droplet micromixer. Droplets of the aqueous samples are formed using a carrier liquid such as oil. The shear force between the oil and sample accelerates the mixing process in the droplet while going through the channel [28, 60].

2.2 Passive Micromixers on Silicon

In this work, four types of passive micromixers were reported. The mixing efficiency was measured by analyzing the images collected from the microscope. The simulations of various designs were done using MemCFD module of CoventorWare^{TM} software.

2.2.1 Fluidic Simulations of Micromixers

Fluid dynamic problems can be analyzed using computational fluid dynamic (CFD) methods. Generally, the fluid domain is discrete into a number of small cells to form grids, and Navier-Stokes equations are solved for the domains. For laminar flows, the Navier-Stokes equation is accurate enough, while for turbulent flows, specials turbulence models are used. In addition to solving the fluid flow equations, CFD module also solves the equations of chemical reactions, heat transfer, and radiation heat transfer. Advanced and complex simulation tools also solve the complex cases for those involving non-Newtonian fluids or multi-phase fluid flows [61]. Finite element and finite volume methods are widely used numerical methods for solving the equations.

Finite element method (FEM) solves the partial differential equations in two or three-dimensional space with fixed boundary conditions either in steady state or transient systems. In FEM, the system is divided into a number of finite elements (small geometries) and edges of these small elements comprise the mesh nodes. The partial differential equations (PDE) are solved at each node and are expressed into a matrix form (n×n matrix for n nodes). The final formulations are solved with appropriated algorithms.

In finite volume method (FVM), "finite volume" corresponds to the small volume surrounding each node point. Therefore, the unstructured meshes can be formulated easily. The volume integrals in PDE are converted into surface integrals using divergence theorem and are evaluated as fluxes at each finite volume surfaces [62]. Fluid flow

equations in a control volume can be obtained by applying fundamental physical principle to that control volume in the form of integration, and these governing equations in the integral form are manipulated to get PDEs.

Following are the basic steps used in solving the fluid dynamics problems using any method:

a). Defining the physical boundaries (geometry).

b). Dividing the geometry occupied by the fluid into a number of discrete cells (meshing).

c). Defining the boundary conditions which involve assigning the fluid properties and behavior at boundaries.

d). Solving the equations using the specified method.

e). Analyzing or visualizing the solution.

2.2.1.1 Introduction to simulation tool

CoventorWare^{TM} is a microelectromechanical systems (MEMS) software package developed by Coventor Inc. [63]. It allows users to design, specify, model and visualize MEMS structures. MemCFD model of this software was used to simulate the micromixers presented in this research. It offers a wide variety of boundary conditions and can provide the solutions for both static and transient compressible and incompressible flows. The fluid flow through the control volume is governed by Navier-Stokes equation and the flow is subjected to conversation of momentum. The equation of the momentum is given by Eq. 2.1:

$$\frac{\partial \vec{V}}{\partial t} + \vec{V} \cdot \nabla \vec{V} = -\frac{1}{\rho} \nabla P + \mu \partial^2 \vec{V} + \vec{f}, \quad (2.1)$$

where $\vec{V}$ and P are the velocity vector and pressure, respectively, $\vec{V} \cdot \nabla \vec{V}$ is the fluid flow flux, $\partial^2 \vec{V}$ is the tensor, and $\vec{f}$ is the vector of body force per unit mass acting on the fluid element.

A wide range of useful measurements such as fluid velocity, viscosity, vorticity, diffusion coefficient, enzyme reaction kinetics and chemical binding coefficients at a given location can be obtained from a simulated microfluidic device.

2.2.1.2 Fluid flow simulation in micromixers

2.2.1.2.1 Simulated designs. The fluid flow, flow velocity, vorticity, and mixing phenomenon were observed in various microchannels using MemCFD module. Figure 2.7 depicts the simulated micromixer designs. Each design has two inlets for fluid injection and one outlet for product collection. Designs 1 (a) and 1 (b) are similar except some of the omega channels in 1 (b) are oriented in different directions. Designs 2 (a) and 2 (b); 3 (a) and 3 (b); 4 (a) and 4 (b) are similar but one of the inlet section of the designs 2 (b), 3 (b), and 4 (b) is divided into two equal channels and these channels are connected to a reactor as depicted in Figure 2.7.

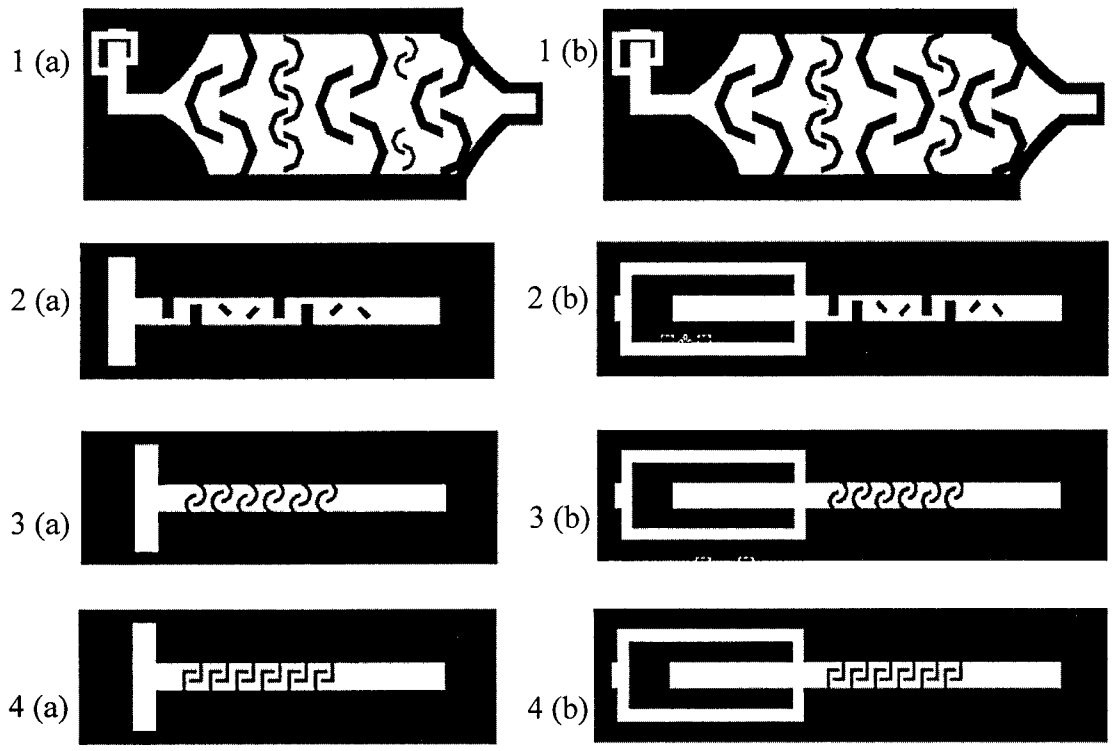

Figure 2.7 Simulated micromixer designs.

Figure 2.8 shows the dimensions of simulated designs. Designs 1 (a) and 1 (b) are equal in dimension. The dimensions of the designs 2 (a), 3 (a) and 4 (a) are equal, but each of them different channels. Similarly designs 2 (b), 3 (b) and 4 (b) are equal. In designs 1 (a) and 1 (b), the widths of the larger, medium and smaller omega channels are 250 μm, 150 μm and 100 μm, respectively. The widths and heights of the omega and L-shaped channels in designs 3 and 4 are 20 μm and 150 μm respectively. In designs 2 (a) and 2 (b), the width and height of larger rectangle channels are 80 μm and 150 μm, respectively; the width and height of inclined small rectangle channels are 40 μm and 150 μm, respectively; the channel depths of all designs were assumed to be 100 μm.

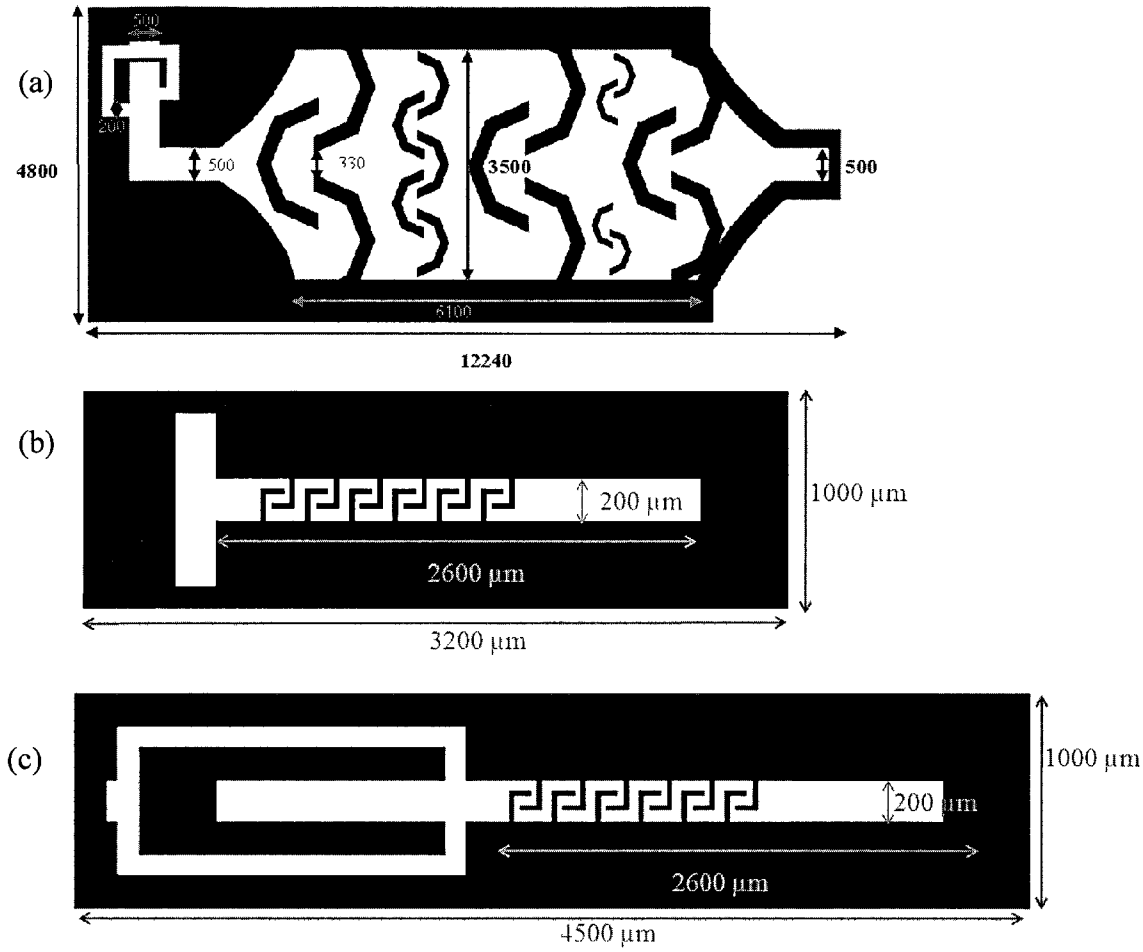

Figure 2.8 Dimensions of the simulated designs.

2.2.1.2.2 Simulation results. The boundary conditions were kept constant for all the simulated designs. Constant flow rate was applied at both the inlet section, while keeping the outlet at atmospheric pressure and assigning no slip flow (zero velocity) condition at channel walls. Water and ethanol are considered as injecting fluids for at the two inlet sections with a flow rate of 0.5 μL/min. The physical parameters of these fluids are presented in Table 2.1.

Table 2.1 Properties of water and ethanol at 20 °C

Fluids	**Viscosity (kg $\mu m^{-1} s^{-1}$)**	**Diffusivity ($\mu m^2 s^{-1}$)**	**Density (kg μm^{-3})**
Water	9.0e-10	1.2e3	9.998e-16
Ethanol	1.2e-9	1.2e3	7.89e-16

Figure 2.9 depicts the 2-D velocity contour in the middle of design 1 (a). From the figure, it is evident that the flow velocity is reaching its maximum whenever the flow converge and the flow velocity is decreasing rapidly after the split due to the backflow generated by the omega channel. It is also observed that the flow velocity is higher in the middle of the channel and is lower at the top and bottom extremes. Figure 2.10 shows the stream line traces of the zero mass particles in design 1 (a). From the figure, it is evident that the particles are trying to stay in the middle section of the reactor and some recirculation of the flow was observed in between bigger and medium sized omega channels, and this recirculation increases the probability of mixing two fluids.

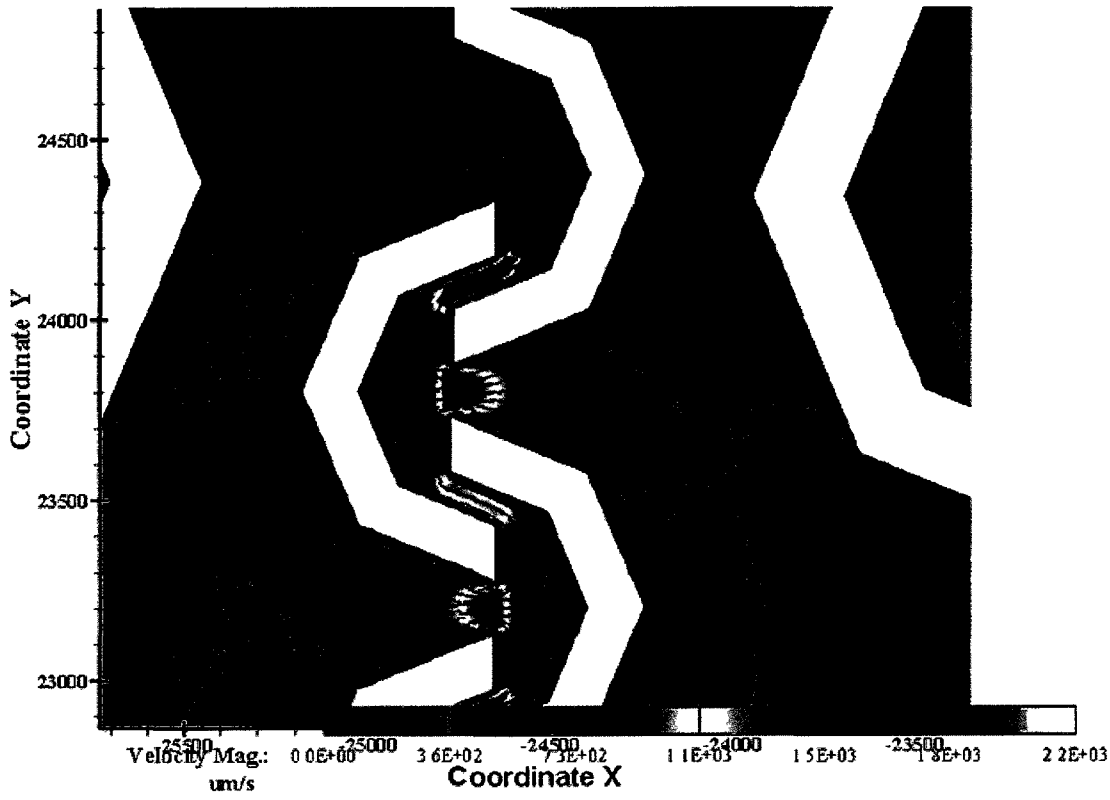

Figure 2.9 Fluid flow in omega channels.

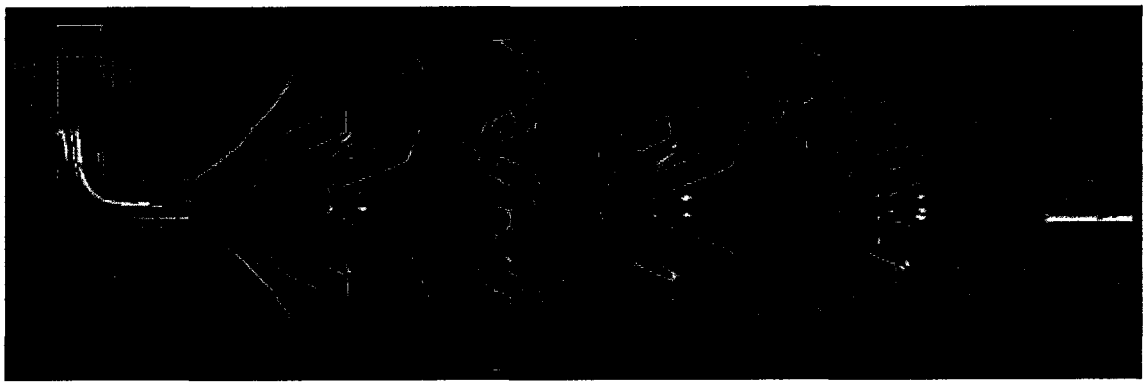

Figure 2.10 Stream line traces in omega channel micromixer.

Figure 2.11 (a and b) represents the vorticity contours of the designs 1 (a) and 1 (b), respectively. Vorticity is the curl of the fluid velocity and indicates how much swirl or shear is there in the flow and is a measure of the mixing in between the fluids. From the figure it can be observed that the vorticity is not constant through the channel length

and is fluctuating. The omega channels and the variation in the channel dimensions might be the reasons behind fluctuating vorticity. According to Figure 2.11, the vorticity of the two designs is nearly equal concluding that the variation in the channel orientation does not improve the mixing between two fluids.

(a)

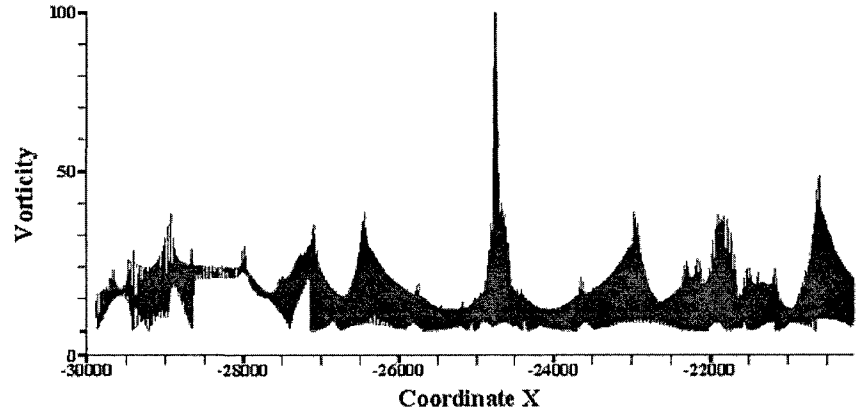

(b)

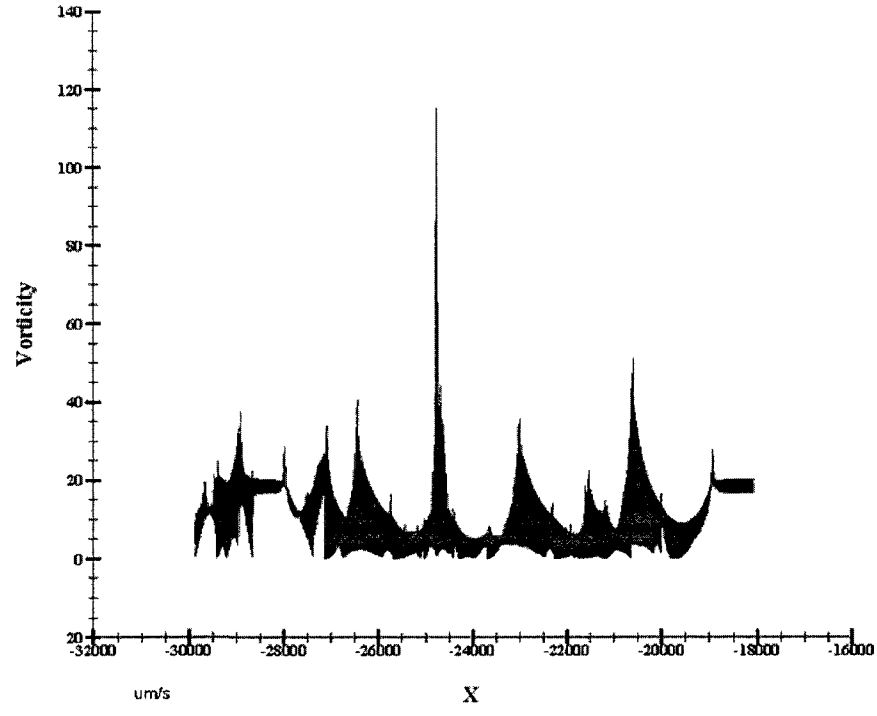

Figure 2.11 Vorticity contours of designs 1 (a) and (b).

Figure 2.12 depicts the flow velocity magnitude in design 2 (b), the red color indicates the maximum velocity, and the blue color indicates the minimum fluid velocity.

(a)

(b)

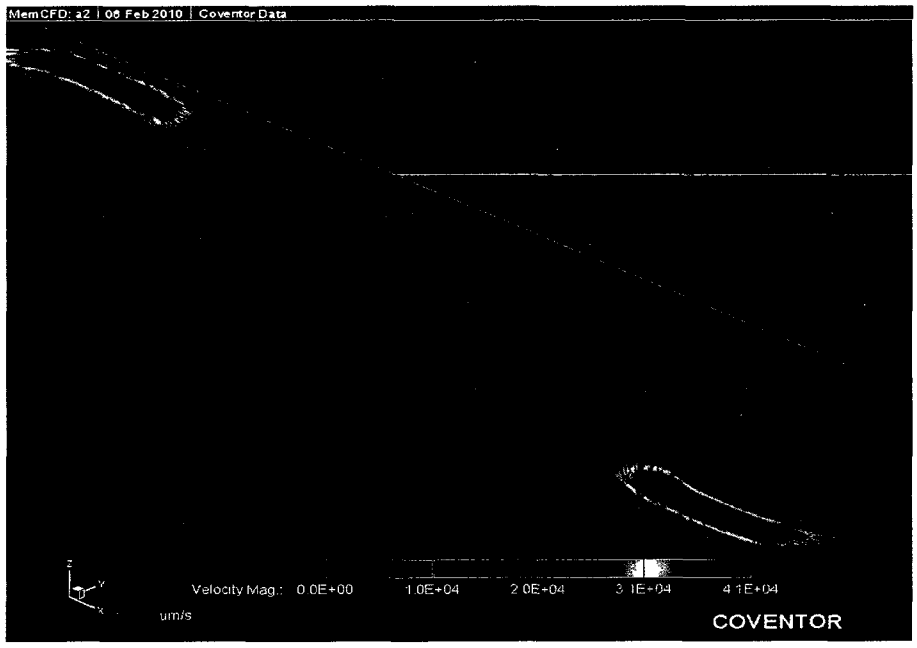

Figure 2.12 Velocity magnitude of the fluid flow in design 2 (b); (a) At the intersection of the two fluids (b) in the middle of the channel.

According to Figure 2.12, the inlet fluid streams are squeezed at the first two rectangular channels and the squeezed streams are released at the inclined channels. Again those are squeezed and released to achieve uniform mixing at the outlet section. From Figure 2.12, it is evident that the fluid flow is attaining its maximum velocity at the

narrow channel created by the vertical rectangular baffle and the inclined baffles are separating the squeezed fluids. This squeezing and separation helps in achieving mixing between the injected fluids.

Figure 2.13 depicts the mixing of two fluids in designs 2 (a) and 2 (b). The red color indicates fluid 1 and is injected through one inlet and the blue color indicates fluid 2 and is injected through the second inlet. The two colors (fluids) are interacting at the inlet junctions and the progression of the color variation from inlet to outlet indicates the progressive mixing of the fluids while moving along the channel. At the outlet section, the color is uniform concluding that the two fluids are mixing uniformly. From Figure 2.13 it is observed that the designs 2 (a) and 2 (b) are exhibiting similar mixing ability.

(a)

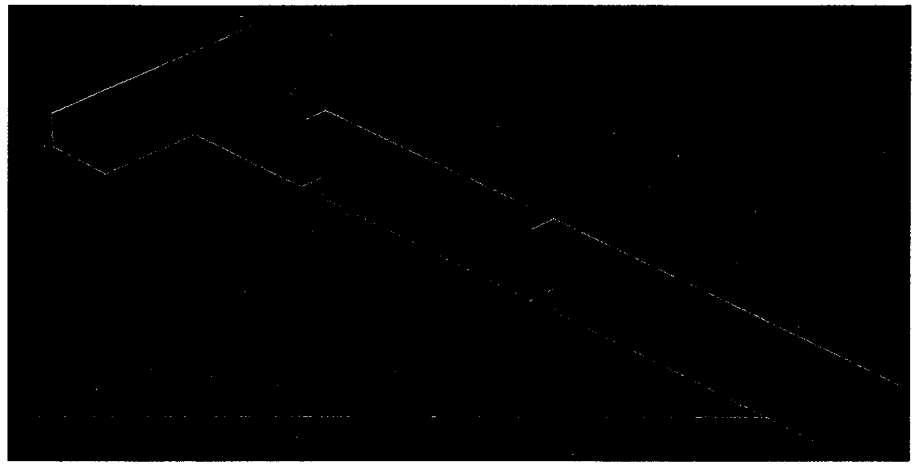

(b)

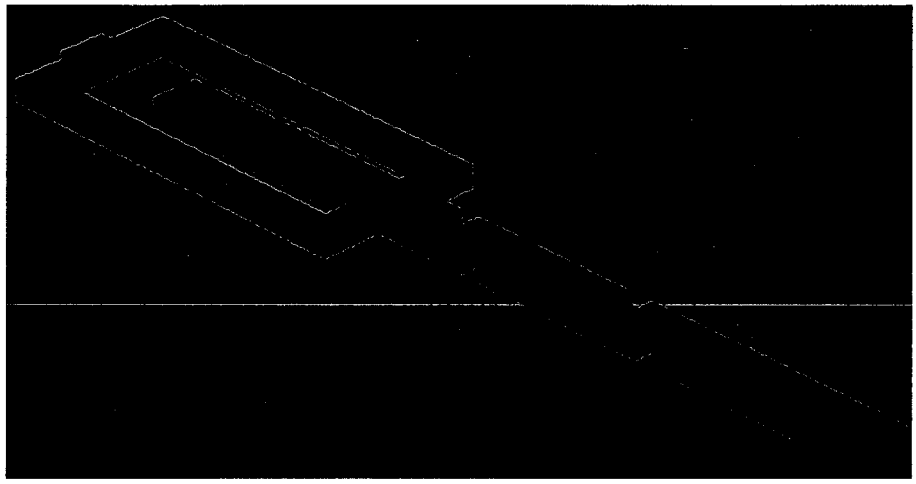

Figure 2.13 Mixing phenomenon observed in designs 2 (a) and 2 (b).

Figures 2.14 and 2.15 show the velocity of magnitude of designs 3 (a) and 4 (a), respectively. In both figures, the fluid velocity is fluctuating along the channel. This rapid variation in the flow velocity along the channel assists the fluids to mix uniformly.

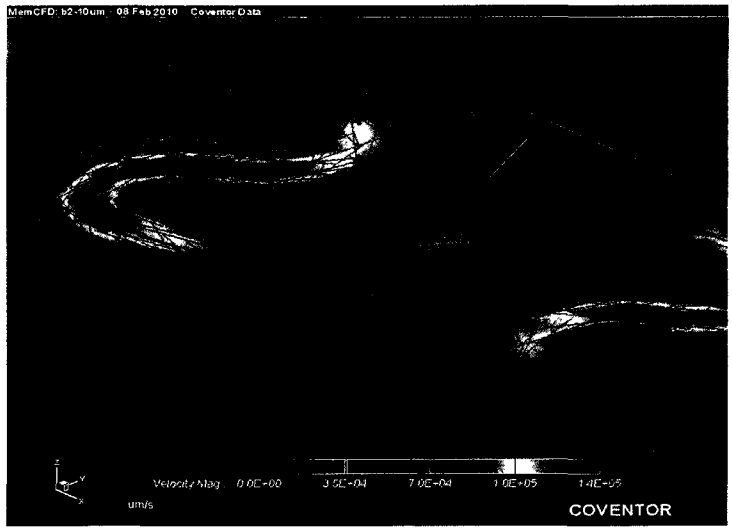

Figure 2.14 Velocity magnitude of design 3 (a).

Figure 2.15 Velocity magnitude of design 4 (a).

Figures 2.16 and 2.17 show the mixing action along the channels of designs 3 (a) and 4 (b), respectively. From the figures, it is observed that the two designs are able to provide uniform mixing at the outlet section.

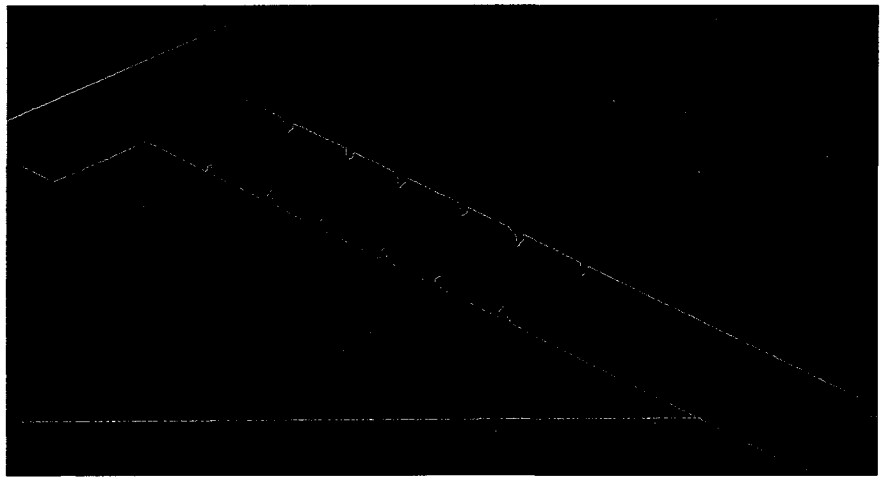

Figure 2.16 Mixing of two colors (fluids) in design 3 (a).

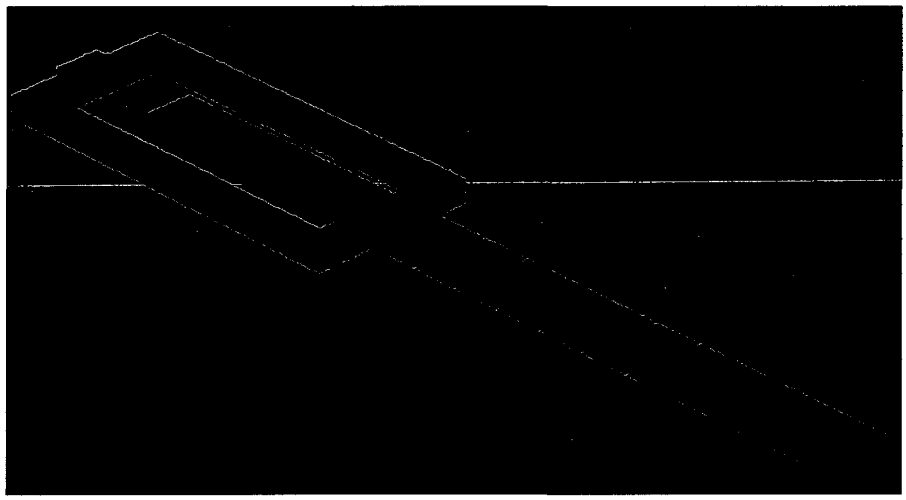

Figure 2.17 Mixing of two colors (fluids) in design 3 (b).

The progression of the fluid mixing can be clearly observed in fluidic simulation videos. The simulation videos of designs 2 (a), 2 (b), 3 (b), and 4 (b) can be found in the attached CD with file names 2 (a), 2 (b), 3 (b), and 4 (b), respectively.

2.2.2 Micromixer Fabrication

Photolithography process was used to fabricate various micromixer designs on silicon wafer. Straight channels with "binomial tree" inlet and outlet section, omega channel

with "binomial tree" inlet and outlet sections, omega channel with "T" inlet junction and omega channel with "intermediate stage" were fabricated on Si wafer. Initially, the appropriate mask was designed using L-Edit mask layout software. A <100> Si wafer with 2 μm oxide layer was used for the micromixer fabrication. The fabrication process steps are discussed below.

1) Pre-cleaning: The Si wafer was cleaned with acetone and isopropyl alcohol (IPA) followed by rinsing with DI water and drying in nitrogen air to remove organic and inorganic impurities.

2) Baking: The pre-cleaned wafer was baked on a hotplate at 200° C for 10 min to evaporate the moisture on the wafer.

3) Spin coating Primer: MCC primer 80/20 was spincoated on the front side of the Si wafer. The coated primer enhances the adhesiveness of the polymer to Si wafer. Spinning parameters are illustrated in Figure 2.18.

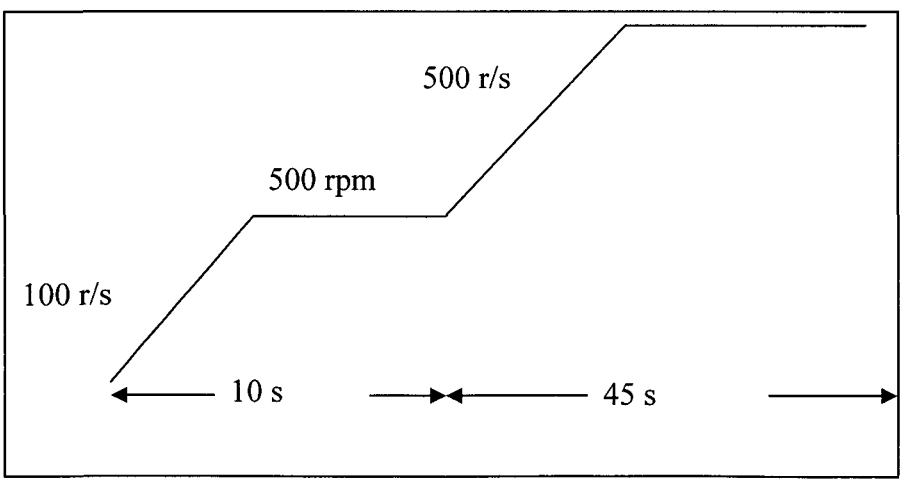

Figure 2.18 Primer spin coating parameters.

4) Photoresist coating: Positive photoresist (PR 1813) was spincoated on the front side of the Si wafer using Cost Effective Equipment (CEE 9601303). The spinning parameters are illustrated in Figure 2.19.

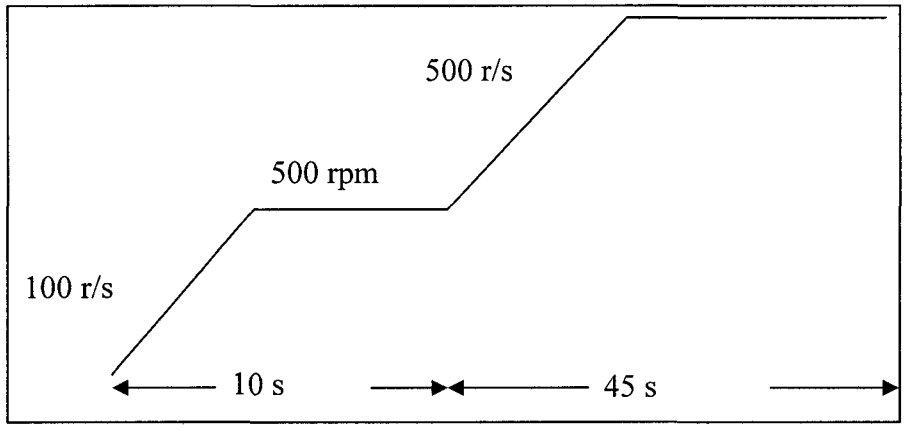

Figure 2.19 PR 1813 coating parameters.

5) Soft baking: Soft baking was done to evaporate the solvent in the coated photoresist and increase the photosensitivity of the resist layer. PR 1813 coated Si wafer was baked on a hotplate at 120° C for 30 s.

6) Backside coating: Steps 3-5 were repeated on the backside of the wafer.

7) Mask alignment and UV exposing: A Mask was loaded onto the mask aligner followed by loading Photoresist coated wafer (Polished side for microchannels). UV light of intensity 7.2 was exposed through the mask on to the Si wafer for 5.7 s. Contact printing technique was used while exposing the UV light, in which both mask and the wafer are in contact with each other.

8) Developing photoresist: MF 319 was used to develop the exposed PR 1813 resist. The exposed wafer was kept in the MF 319 solution for 30 s. After developing, the wafer was cleaned with DI water and dried in nitrogen.

9) Hard baking: The developed wafer was baked on a hot plate at 120° C for 2 min.

10) Backside patterning: Steps 7-9 were repeated on the back side of the wafer to get patterned PR 1813. During mask alignment, alignment markers on the front and back side must be aligned.

11) SiO_2 etching: 2 μm SiO_2 layer on both sides was etched using J.T. Baker's Buffer oxide etchant (BOE). The wafer was placed in BOE solution for 20 min followed by rinsing with DI water and drying in nitrogen air.

12) Baking: The SiO_2 patterned wafer was baked on a hotplate at 120° C for 2 min to evaporate the water on the wafer.

13) Si etching: ALCATEL A 601E Inductive Coupled Plasma (ICP) etching reactor was used to etch the SiO_2 patterned Si wafer. The SiO_2 layer on the wafer acts as a mask to ICP etching. Initially, the front side of the wafer was etched to 100 μm depth followed by etching the wafer on the backside to make via holes for inlets and outlet sections.

The BOSCH Big 50 process was used to achieve vertical side walls. It uses alternating etch and polymer deposition cycles. Sulfer hexafluoride (SF_6) was used for Si etching and Octafluorocyclybutane (C_4F_8) polymer was deposited to prevent the side wall etching. Table 2.2 provides the used parameters for ICP etching.

Table 2.2 ICP etching parameters.

Parameter	Value
SF_6 Flow	300 sccm
C_4F_8 Flow	50 sccm
He regulation	3.6 sccm
Pressure	38 mtorr
Pressure	7.5 mTorr
Source, RF1	1800 W
RF2	30 W
Temperature	20 C
Pressure regulation	20 Torr
Deposition & Etch cycles	5-12 s

An etch rate of 6.5 μm/min was observed for etching the front side of the wafer. After etching the front side, via holes at the inlet and outlet, sections were made by etching the SiO_2 wafer from the backside as depicted in Figure 2.20.

Si with oxide layer

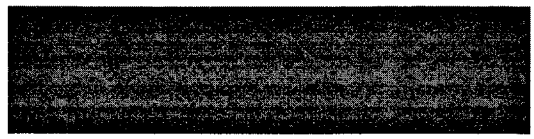

Spin coat PR 1813 resist on front side

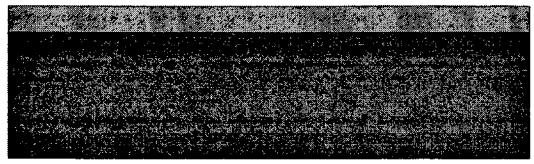

Spin coat PR 1813 resist on back side

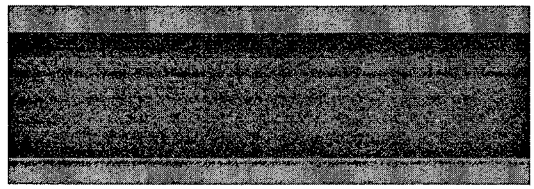

Pattern PR 1813 resist on front side

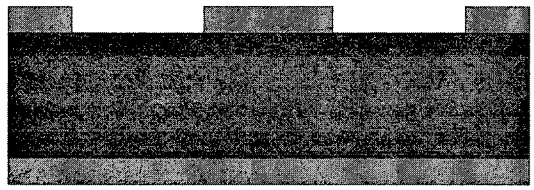

Pattern PR 1813 resist on backside

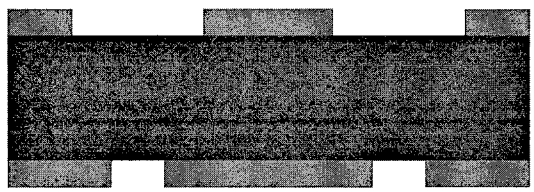

Etch SiO_2 on both sides

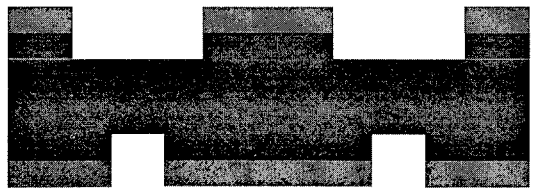

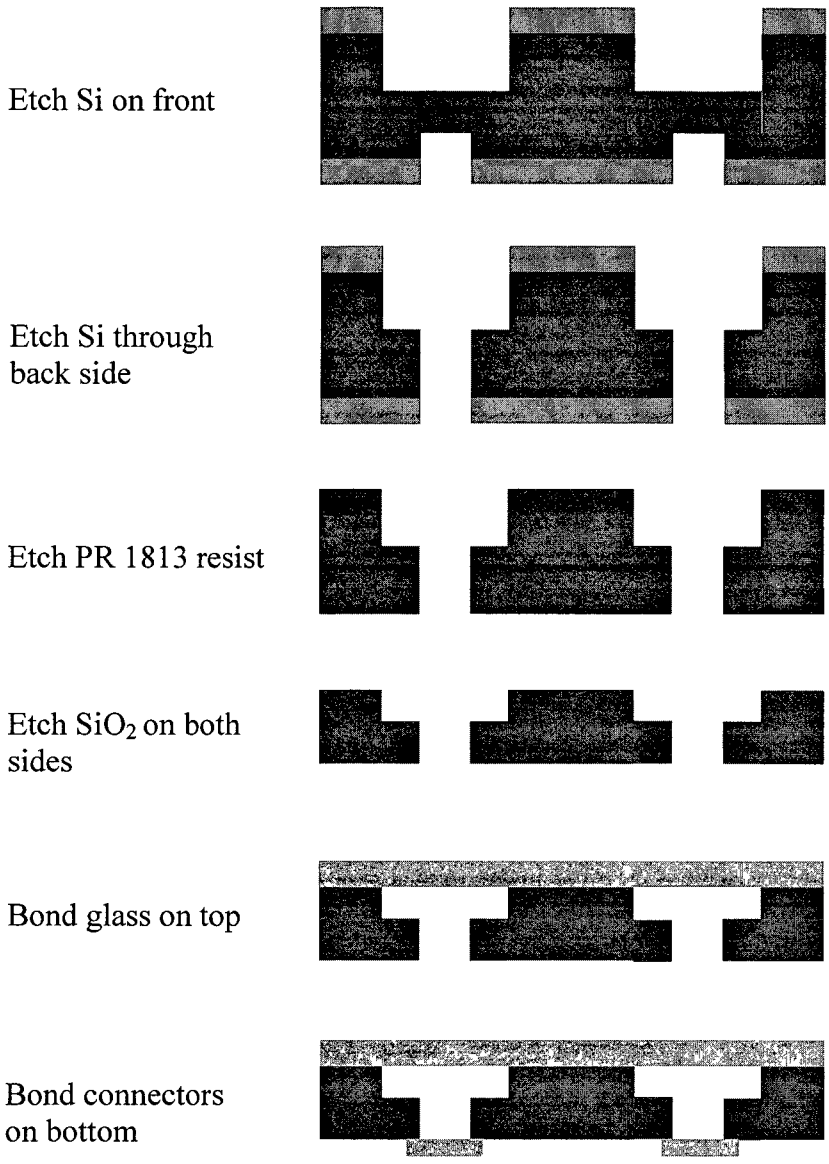

Figure 2.20 Schematic illustrations of micromixer fabrication process steps.

14) Etch PR 1813 and SiO_2: After etching Si wafer selectively, PR 1813 and SiO_2 layers were etched using acetone and BOE solutions, respectively.

15) Glass bonding and dicing: A glass wafer was bonded to the top side of the patterned Si wafer using anodic bonder. The glass and patterned Si wafers were cleaned with RCA1 and RCA2 cleaning agents thoroughly followed by rinsing in DI water and drying

in nitrogen air before bonding. After7 bonding the glass to the Si wafer, the wafer was diced into pieces using dicing instrument.

16) Bond connectors: Connectors obtained from Cole Palmer were attached on the backside at the inlet and outlet sections using epoxy. Figure 2.21 depicts the fabricated micromixers with attached connectors.

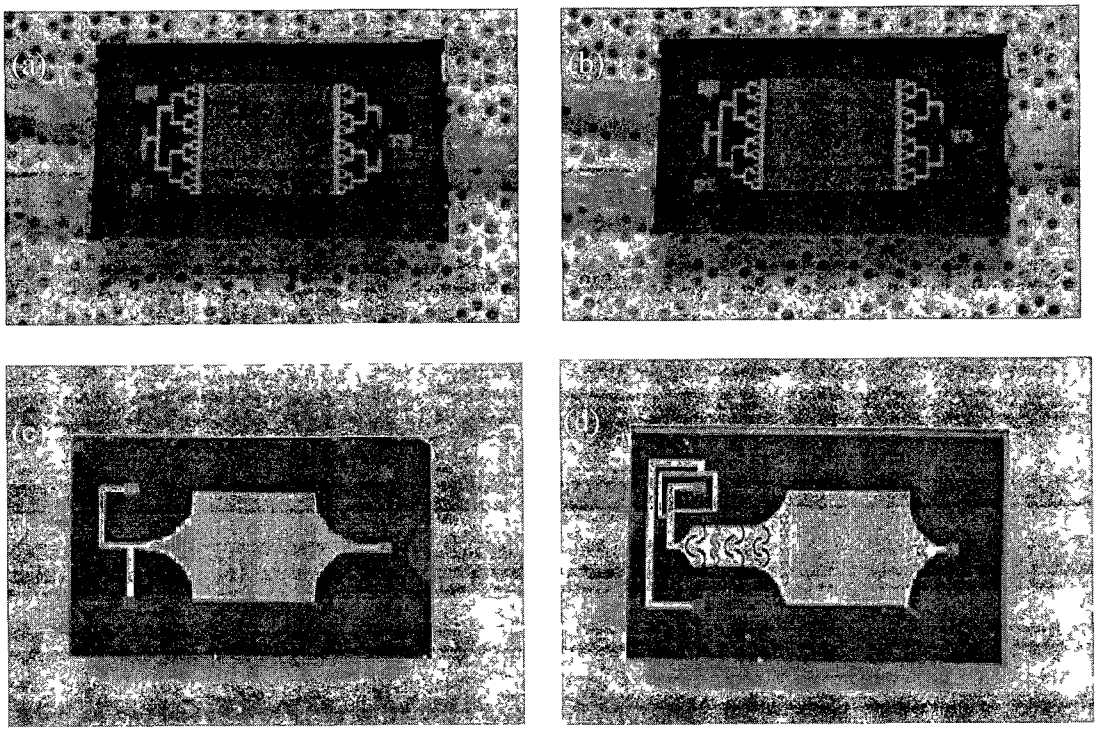

Figure 2.21 Fabricated micromixers (a) straight channels with "binomial tree" inlet and outlet section (b) omega channel with "binomial tree" inlet and outlet sections (c) omega channel with "T" inlet junction (d) omega channel with "intermediate stage".

2.2.3 Test Setup

Figure 2.22 shows the test setup of the fabricated micromixers. The two fluids were injected to the micromixer under test, using a Kd Scientific syringe pump with a defined flow rate and the effluent was collected in a small glass beaker. The fluid flow and mixing phenomenon in the microchannels were observed using the microscope. The

digital camera attached to the microscope enable in viewing the fluid flow on a computer. The images and videos of the fluid flow were observed and stored on the computer for the image analysis.

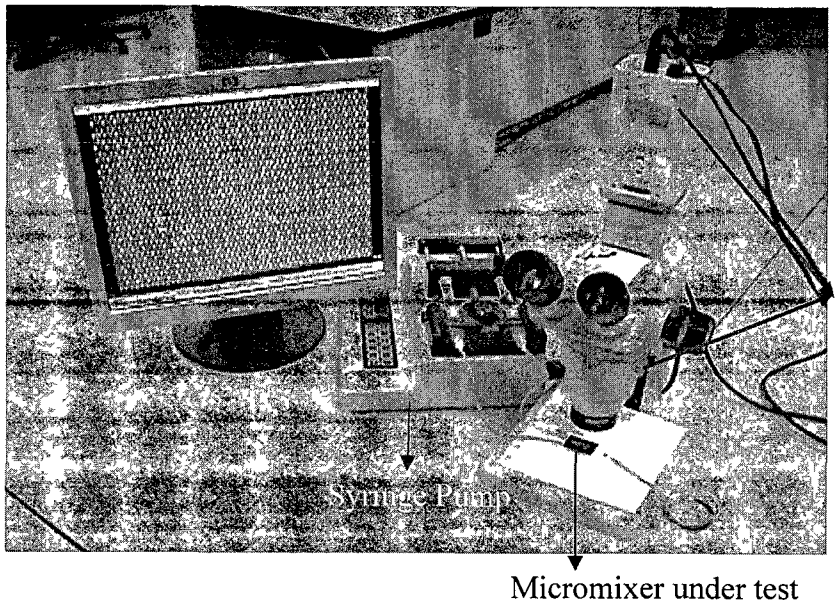

Figure 2.22 Test setup of micromixer.

2.2.4 Results and Discussion

The testing of mixing phenomenon in the micromixers was measured by, injecting two test fluids of different colors (red and blue) and collecting images using the microscope. Figure 2.23 depicts the fluid flow in straight channel micromixer. It was noticed that the flow was laminar and no mixing was observed at the outlet section.

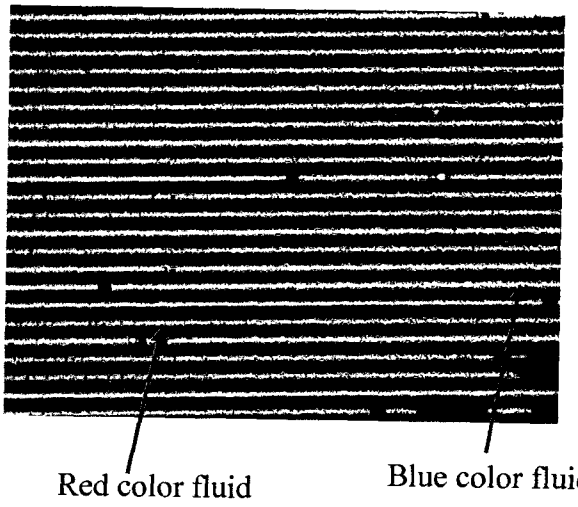

Figure 2.23 Straight channel micromixer testing results.

Figure 2.24 depicts the microscopic image of the fluid distribution in the omega channel micromixer with "binomial tree" inlet and outlet sections. It was noticed that the follow was not completely laminar and the omega channels created some rotational flow. The mixing action of the two different colored fluids was higher compared to that observed in straight channel devices.

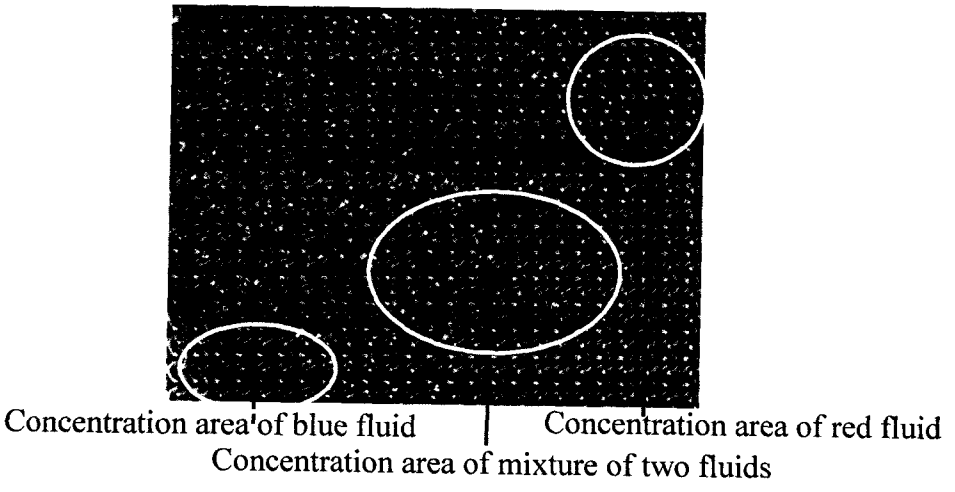

Figure 2.24 Fluid distribution in omega channel micromixer with "binomial tree" inlet section.

From Figure 2.25, it is noticeable that both the dyes still have separate domination in most part of the device, and it is due to the straight inlet channel design (Binomial tree inlet) of the micromixer as shown in the figure. The two fluids are taking different path flows in a laminar fashion into the channels to cause the domination of these fluids in separate regions of the device.

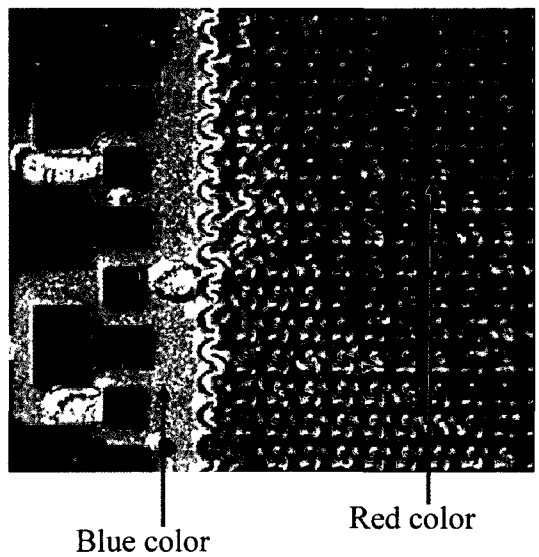

Figure 2.25 Fluid distribution in the binomial tree inlet section.

The binomial tree inlet section was modified to T-inlet section and also some omega channels were added to achieve initial mixing as shown in Figure 2.26. In the previous design, the flow is laminar until the fluids reached omega channel and mixing was observed only in middle region of the channel. In the current design, omega channels are closer to the inlet T-junction to create rotational flow and little mixing was observed even in the region that is near to the inlet section.

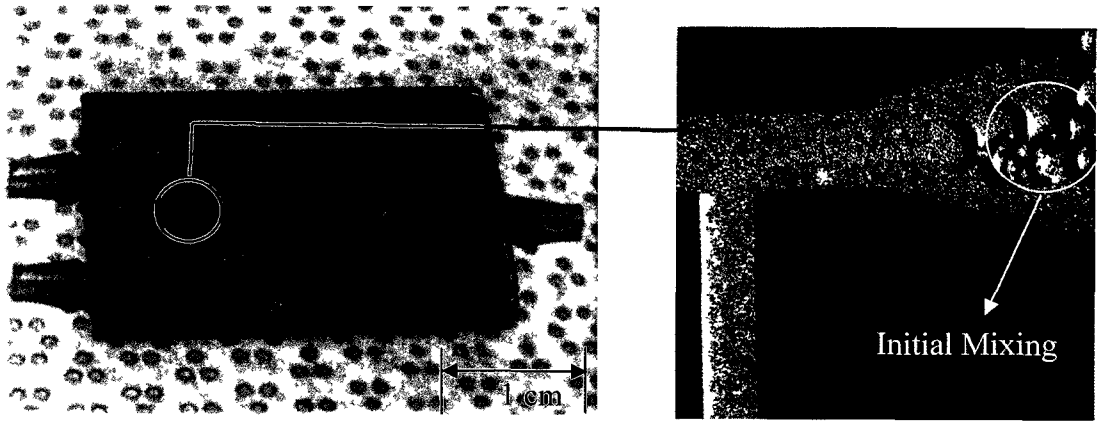

Figure 2.26 Micro-mixer with T-inlet section (left) and inlet design with more omega channel for initial mixing of the two fluids (right).

Figure 2.27 shows the fluid distribution in the omega channels. It was noticed that the mixing action of two fluids was higher in the region nearer to inlets and in the middle of the device and the fluid flow was laminar at the two extremities (edges) of the device. The laminar flow at the extremities might be due to the laminar flow of the fluids at the inlet (T-junction), which resulted in the domination of red color in the upper portion of the device and domination of blue color in the lower portion of the device.

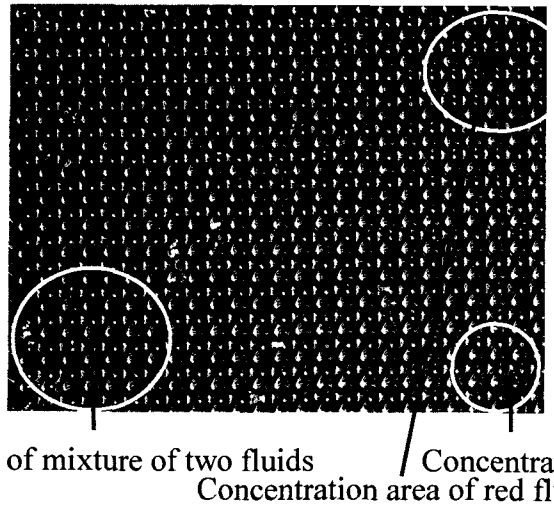

Figure 2.27 Fluid distribution in T-inlet omega channel micromixer.

The inlet section was modified as shown in Figure 2.28 to avoid the laminar flow at the inlet section and an additional intermediate stage was added to achieve initial mixing before the fluids reach the reactor.

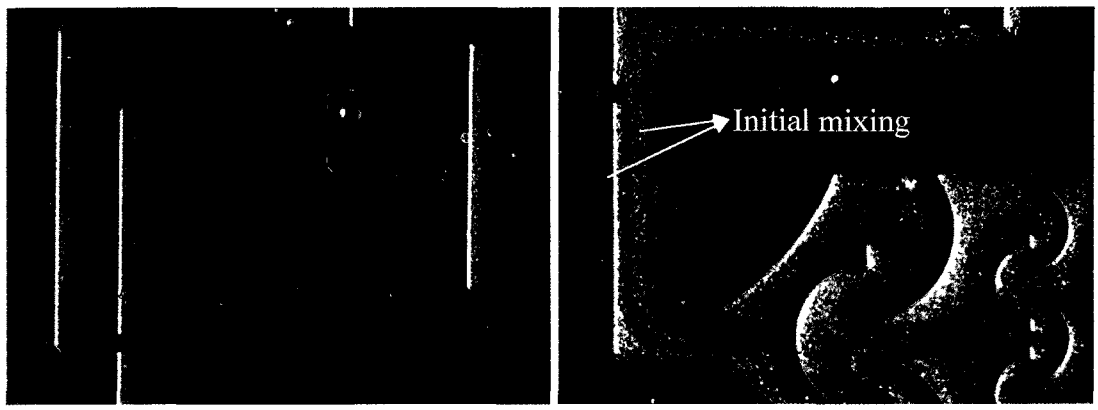

Figure 2.28 Modified inlet section (left) and initial mixing observed at the inlet section (right).

From Figure 2.29, a circular flow can be observed at the intermediate stage. The bigger omega channels are creating the circular flow to increase the mixing phenomenon. The initial mixed fluids are further mixed in the reactor to get uniform mixing at the outlet section.

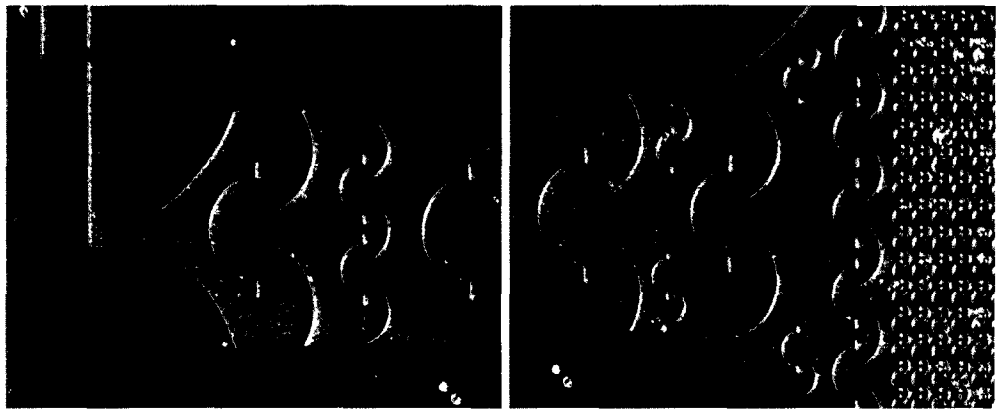

Figure 2.29 Circular flow at the intermediate stage (left) and mixing at the junction (right).

The fluid flow and fluid distribution in the microchannels can be clearly observed in the videos taken while testing the micromixer. The testing result videos of the micromixer were made into a single movie file and can be found in the attached CD with file name "Movie".

2.2.5 Quantification of Mixing Efficiency

After collecting the images from the microscope, Image Pro Analysis software version 7.0 was used to calculate the mixing efficacy of the fabricated devices by measuring the standard deviation of red, green and blue (RGB) values at the inlet and outlet sections.

Each image constitutes an array of pixels and each pixel is associated with its own RGB values. The standard deviation represents the color uniformity. Therefore, if the color is uniform at a certain location and all the pixels at the location have the same RGB values, it represents the uniform mixing zone (as the testing fluids are two food coloring dyes). From the inlet to outlet section along the channel, the standard deviation of R or G or B decrease gradually and reaches a minimum value at the outlet section [64].

Using Image Pro Analysis software, the standard deviations of RGB were obtained at certain locations on both inlet and outlet sections as depicted in Figure 2.30. The standard deviations of R, G, and B were averaged at both inlet and outlet sections to get the measure of color gradient at the corresponding section. The mixing percentage (Ø) was calculated using Eq. 2.2:

$$\phi = \left(1 - \frac{\sigma_{outlet}}{\sigma_{inlet}}\right) \times 100, \tag{2-2}$$

where σ_{inlet} is the averaged standard deviation at inlet section and σ_{outlet} is the averaged standard deviation at the outlet section or the chosen section of the device.

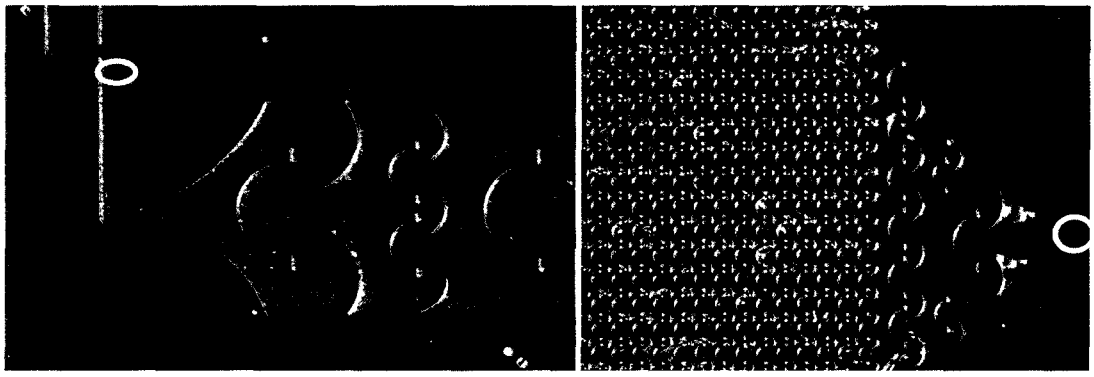

Figure 2.30 Measuring RGB values at inlet (left) and outlet (right) section.

The mixing percentages of straight channel, omega channel with binomial tree inlet and outlet sections, omega channel with T-inlet section, omega channel with intermediate stage micromixers with were observed to be 2%, 10%, 28.6% and 65.09% respectively at the outlet section.

2.3 Flexible Polymer Micromixer

A passive flexible polymer disposable micromixer was fabricated on polyester sheet using xurography (razor writing) technique. This involves a computer controlled cutting plotter to cut the films according to the specified design. The device is comprised of five consecutively alternative layers out of which three comprise the middle one, thereby defining the channel height of 350 μm. Figure 2.31 depicts the solid works model of the polymer micromixer. The micromixer body without the Polydimethylsiloxane (PDMS) ports was fabricated from scratch within 15 min, making the cutting pattern design much less labor intensive than the standard clean room processing techniques.

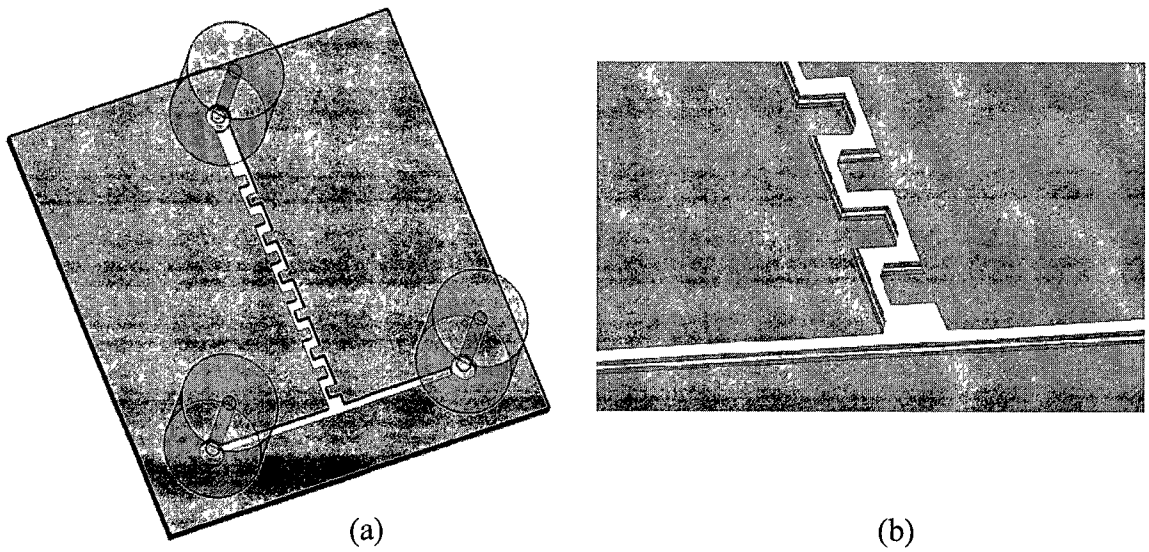

(a) (b)

Figure 2.31 (a) Solid works model of the polymer micromixer (Top view) (b) Three layered polymer patterns constitute microchannel of the micromixer (Top view).

2.3.1 Fabrication of Polymer Micromixer

Initially, the mask was designed using Adobe Illustrator CS3 vector graphics editor and the mixer fabrication steps were depicted in Figure 2.32. A 125 μm thick polyester sheet was used as the substrate material and it was cleaned with DI water and dried in nitrogen air to remove the impurities on the substrate. Two double-sided polyimide tapes with silicone adhesives were attached on both sides of the substrate to achieve a 350 μm thick polymer sheet. A computer controlled cutting plotter was used to cut the polymer sheet according to the specified mask design and the unwanted portion of the sheet was peeled off using tweezers to leave the patterned sheet with microchannels. Later, a polyester sheet was attached on the bottom side of the patterned sheet, and it was drilled at defined locations to make holes for inlet and outlet connectors. A polyester sheet was attached on the top side of the polymer sheet to enclose the channel region and this fabricated polymer mixer was heated on a hot plate at 150° C for 5 min to improve the bond strength. Polydimethylsiloxane (PDMS) prepolymer was mixed with curing agent in a 10:1 ratio and cast on the Petri dish to make the PDMS sheet for the inlet and outlet ports. Later, 1.5 mm diameter holes were made through these PDMS ports and Loctite super glue was used to fasten these ports on the inlet and outlet holes of the device.

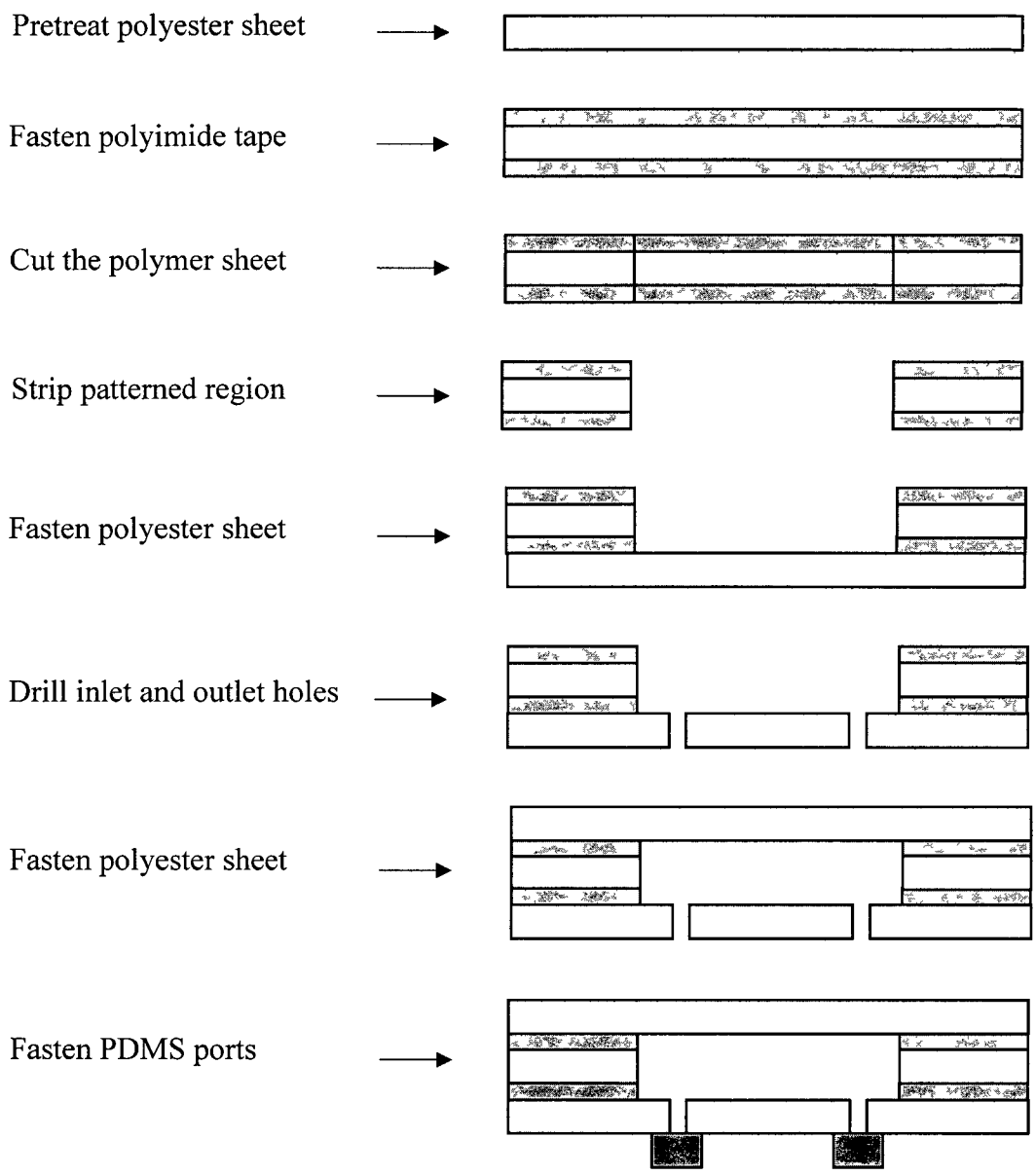

Figure 2.32 The process steps involved in polymer micromixer fabrication.

The polyimide tape silicon adhesive, present on both sides guarantees the structural integrity of the design by bonding the layers and creating a unique composite structure, yet maintaining the device's flexibility. Figure 2.33 shows the fabricated flexible polymer micromixer with inlet and outlet ports. The long inlet channels are designed facilitating device evaluation in the initial design stages and are obsolete in a final minimized design

reducing total volume and material cost. The width of the channel at the intersection of the two inlet sections is 1.2 mm. The mixing channel is comprised of twelve rectangular baffles of width 0.72 mm and height 0.84 mm separated by a distance of 0.72 mm. The total mixing channel length is 18 mm and the perfect cutting of the substrates has an ideal mixing channel volume of 5.33 μL. The total thickness of the micromixer excluding the inlet and outlet ports is 0.6 mm

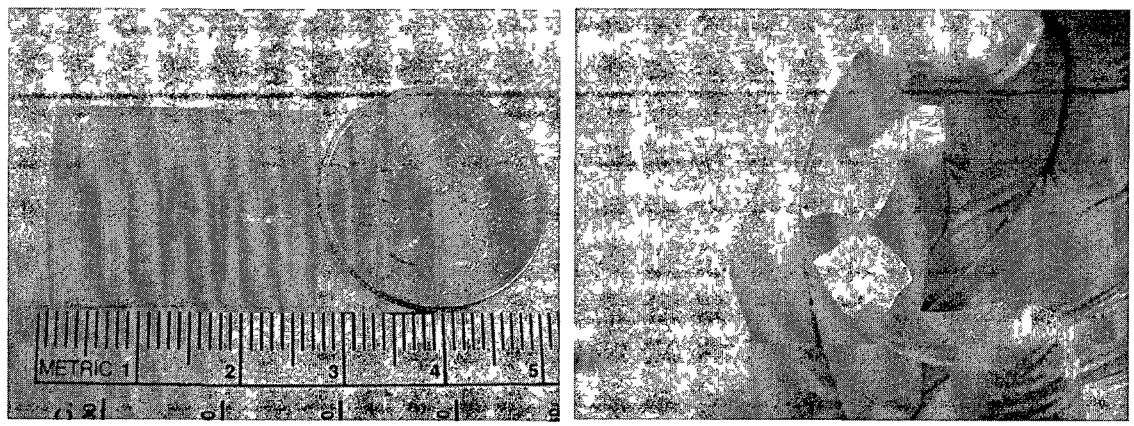

Figure 2.33 Fabricated flexible polymer micromixers.

Figure 2 34 shows the rectangular baffles at the inlet and outlet sections. After cutting the polymer with a cutting plotter, some of the baffles are found to be in exact rectangular shape while some of them have rounded corners. This deviation in the baffle shape is slightly altering the channel dimensions. However, it is not affecting the mixing performance considerably.

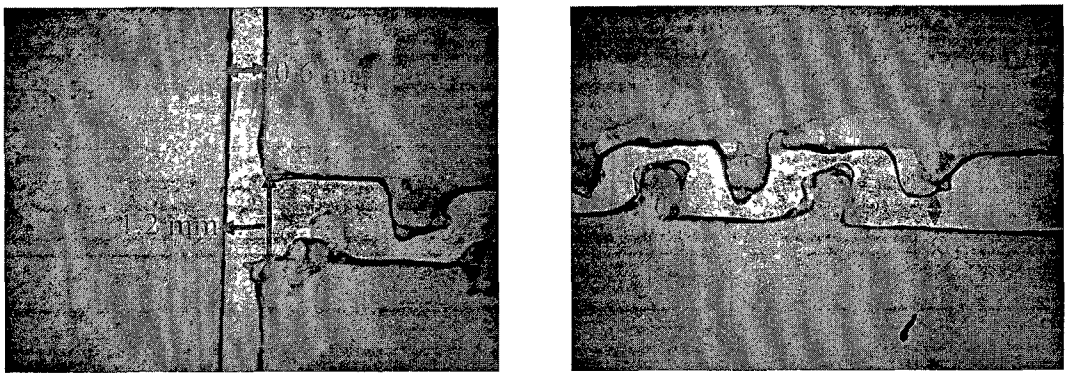

Figure 2.34 The inlet (left) and outlet (right) sections of the polymer micromixer.

2.3.2 Characterization and Mixing Analysis

The bond strength of the adhesive was measured after fabricating the device using Sebastian five tensile strength and the average bond strength was found to be 1.46 MPa, which is close to the minimum bond strength of the two PDMS layers bonded using oxygen plasma technique [65].

The mixing efficiency of the polymer micromixers were evaluated experimentally using color absorbance method and image analysis methods. Kd Scientific syringe pump was used to inject the red and blue food coloring dyes to the micromixer.

In the image analysis method, the fluid flow images at inlet and outlet sections were taken using the microscope and the mixing efficiency was analyzed according to Section 2.2.5. Two outlets were made on the device instead of one outlet to use the color absorbance method. The absorbances of the red and blue colored dyes were measured using 2000C spectrophotometer instrument (Thermo Scientific) before injecting them into the mixing chamber. Later, the absorbance of the two effluents collected at the two corresponding outlets. The mixing index (*M.I.*) was calculated using the Eq. 2.3:

$$M.I. = 1 - \left| \frac{O_1 - O_2}{I_1 - I_2} \right|, \tag{2.3}$$

where I_1 and I_2 are absorbance of the inlet colors and O_1 and O_2 are the absorbances of the outlet color products. For a uniform and complete mixing, the absorbance of the outlet color products should be equal and a *M.I.* of 1 indicates 100% mixing and *M.I.* of 0 indicates no mixing.

2.3.3 Results and Discussion

NaOH and Phenolphthalein chemical reaction was used to observe the mixing ability of the polymer micromixer in one set of experiments. 0.5 M NaOH and 0.3 M Phenolphthalein solutions were injected through the inlets with a flow rate of 40.5 μL/min. Both the liquids are colorless, separates and forms pink color upon mixing. Figure 2.35 depicts the formation of pink color product along the channel from the inlet to the outlet section.

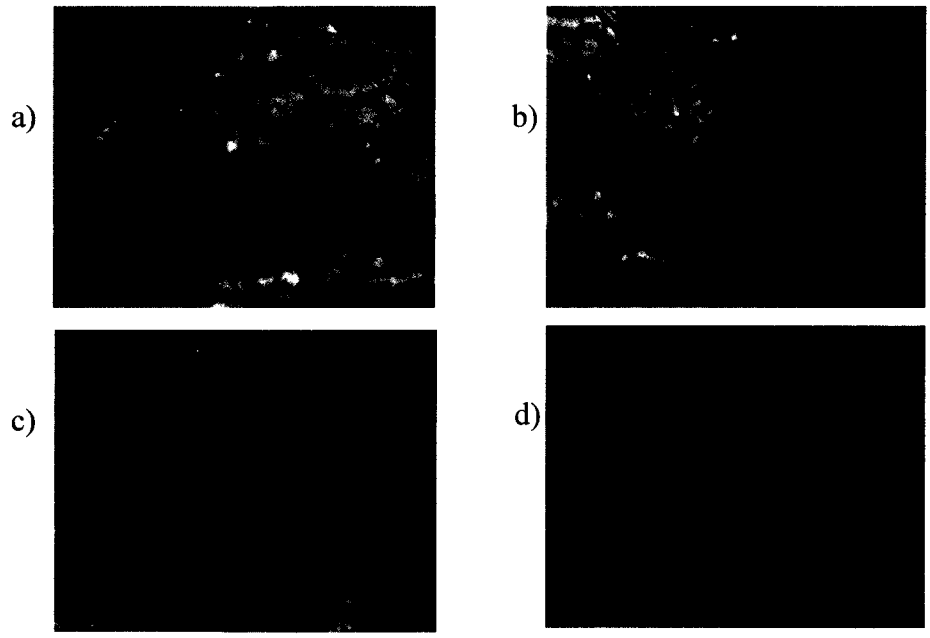

Figure 2.35 Formation of pink color product at (a) inlet T- junction (b) near inlet junction (c) middle of the channel (d) near outlet section.

The mixing performance of the fabricated polymer micromixer for different flow rates was measured by successively injecting the fluids into a micromixer channel with flow rates 4.05 μL/min, 40.5 μL/min, 405 μL/min, 805 μL/min, 1.215 mL/min, 1.620 mL/min, 2.025 mL/min, and 4.05 mL/min. (the corresponding calculated *Re* at the inlet T-junction are 0.1, 1, 10, 20, 30, 40, 50, and 100, respectively). Figure 2.36 depicts the mixing efficiency of the fabricated micromixer over a wide range of *Re* (i.e. for a wide range of flow rates). The mixing efficacy was greater than 90% from *Re* = 0.1 to *Re* = 30 and it is decreasing with higher flow rates and it was 69.7% for *Re* =100.

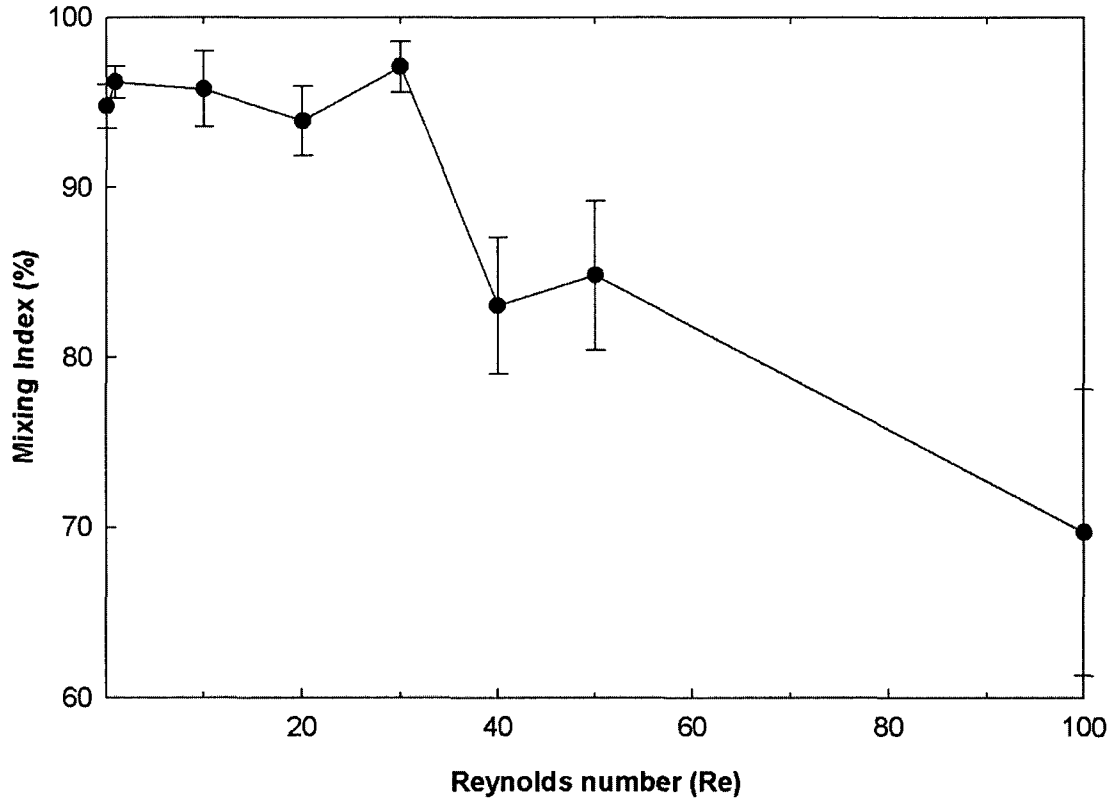

Figure 2.36 Mixing index vs Reynolds number (*Re*). The *Re* mentioned here is the *Re* calculated at the inlet T-junction.

To evaluate the reproducibility of the polymer micromixers, five mixers were tested at *Re* = 1 by measuring the absorbance of the color products and calculating the

mixing index using Eq 2.3. Figure 2.37 depicts the M.I. of five mixers and each of the mixer was tested five times for the repeatability assessment in each device. All the tested micromixers showed M.I. greater than 90% as shown in Figure 2.37 and the average M.I. was found to be 94.935 ± 2.76%.

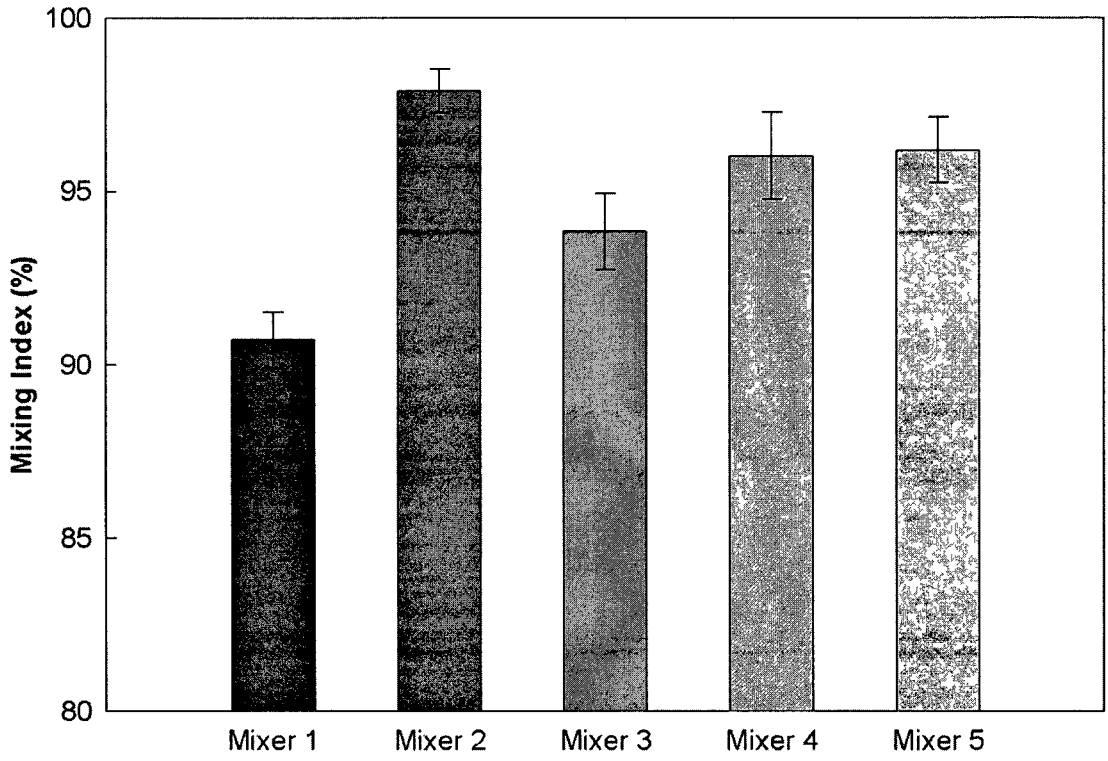

Figure 2.37 Testing results obtained from repeatability test.

Figure 2.38 depicts the M.I. of the micromixer for three bending angles and from the figure it is evident that the M.I. for the measured angles is greater than 90%. The polymer micromixer was leaking for bending angles above 60°, thus imposing a limitation on flexibility during the flow.

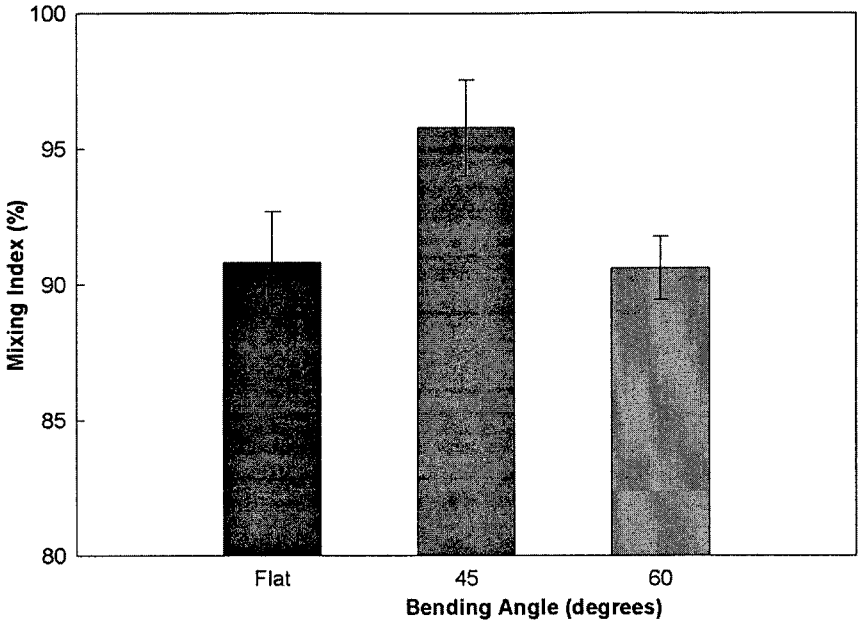

Figure 2.38 Mixing Index vs bending angle.

Biological samples such as proteins are sensitive to harsh environments. To evaluate the biocompatibility of the device, 9.52 μg/ml glucose oxidase (GOx) and 1 M glucose were injected through the two inlets of the mixer and the reaction product formed according to Eq. 2.4 at the outlet of the micromixer was collected. A 200 μg/ml horseradish peroxidase (HRP) and 160 μg/ml O-dianisidine were added to the collected reaction product at the outlet to result in a color product according to Eq. 2.5 and the absorbance of the color product was measured with a spectrophotometer. All the solutions used in this test were prepared in 1x phosphate buffer saline (PBS), pH 7.2.

$$\beta - D - Glucose + O_2 + H_2O \xrightarrow{GOx} D - gluconicacid + H_2O_2 \quad (2.4)$$

$$H_2O_2 + O - dianisidine(reduced) \xrightarrow{HRP} O - dianisidine(oxidised) + H_2O \quad (2.5)$$

Figure 2.39 presents the enzyme activity measurements for glucose oxidase enzyme that was passed through the channel along with the glucose at various flow rates. A control experiment was done using a pipette for measuring the absorbance of the product

formed. From Figure 2.39, it is evident that the enzyme is active for a wide range for *Re* and also the absorbance of the color product formed due to micromixer mixing and is higher than the absorbance of the product formed due to pipette mixing. This indicates that the reaction between GOx and glucose in micromixer was better than in that of pipette mixing. In Figure 2.39, the absorbances of the color products were decreasing from *Re* = 0.1 to *Re* = 100 indicating that the reaction mechanism between GOx and glucose was decreasing at higher flow rates due to the lower probability of mixing and this result is in agreement with the results obtained from Figure 2.36, where the M.I. was decreasing at higher flow rates.

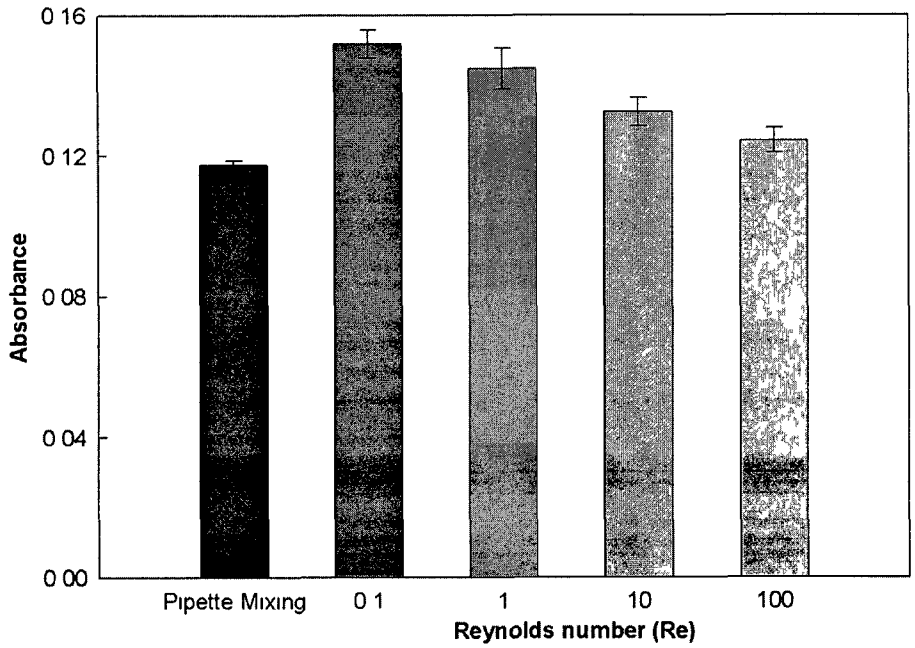

Figure 2.39 GOx activity measured in microchannels.

CHAPTER 3

PEDOT:PSS BASED ELECTROCHEMICAL TRANSISTOR

During the past two decades, a myriad of solid state electronic devices such as light-emitting diodes [66], photo diodes [67], solar cells [68], rectifiers [69], electrochemical devices, and thin film transistors [16, 17] have been explored using organic semiconducting materials such as conducting polymers by utilizing electrical, mechanical and optical properties of these materials.

3.1 Conjugated Polymers

Polymer is a material made up of repeated monomers. DNA, proteins and cellulose are examples of natural polymers. In the year 1977, Alan Heeger, Alan MacDiarmid, and Hideki Shirakawa discovered that the available plastics or insulating polymers could be made electronically conductive [15]. Twenty-three years later, they were awarded with the Nobel prize in chemistry for "the discovery and development of electrically conducive polymers" [70]. This has attracted considerable interest in the development of semiconducting and conducting materials. The physical or chemical properties of the polymers can be tailor made according to the applications as they show various electrical, optical and mechanical properties [71]. Some polymers are sensitive to high-energy radiation and lose their solubility when exposed to ultraviolet light and this principle is widely used in photolithography [72]. In addition, most polymers can be processed as liquids, thanks to

the property that makes them dissolve in water or organic solvents. This has led to the creation of polymer structures using simple manufacturing techniques such as casting, spin coating, screen printing, and moulding [73].

3.1.1 Conducting Mechanism of Conjugated Polymers

The electrical conductivity of conducting polymers is about 10^{-18} S/m, while that of doped conducting polymer can reach about 10^{7} S/m [74]. The differences in the electrical conductivity of the polymers arise due to the difference in number of atoms that the carbon has to be bind. In polyethylene, (a common material in regular plastic bag), each carbon atom binds to two hydrogen atoms and two other carbon atoms as depicted in Figure 3.1 (a), while in polyacetylene, each carbon atom binds to two adjacent carbon atoms and a hydrogen atom as shown in Figure 3.1 (b).

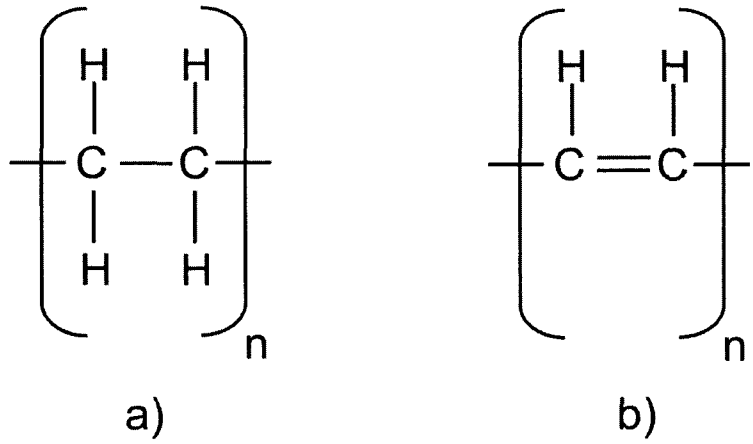

Figure 3.1 Chemical structures of (a) polyethylene (b) polyacetylene [75].

The insulating property of polyethylene can be attributed to the localization of each carbon valance electron in the bonding molecular orbital, whereas in polyacetylene, each carbon atom has an electron left in non-hybridized P_z orbital and these P_z orbitals forms a molecular π (pi)-bond [75]. This result in electron delocalization along the

backbone of the polymer to yield conjugated polymer structure with alternating single and double bonds between the carbon atoms. The electrical conductivity of these conductive polymers can be attributed to the conjugated bond (alternative single and double bond) [76].

In conducting polymers, a series of energy bands: π bond and σ bond occur due to the overlapping of molecular orbitals of repeated units in space. Delocalized electrons from their parent atoms form two molecular orbital of different energies: highest occupied molecular orbital (HOMO) and lowest unoccupied molecular orbital (LUMO). HOMO defines the high energy edge of the valence band and LUMO defines the bottom of the conduction band. Therefore, energy gap (E_{gap}) is the difference in energy between HOMO and LUMO.

A planar σ bond structure occurs, when hybrid orbitals are formed from one 2s and two 2p orbitals. The third 2p orbital on the carbon atom, i.e., $2p_z$ overlaps with a $2p_z$ orbital of neighboring carbon atom to yield two pairs of π-orbitals and the resulting π bond is parallel to underlying σ bond as shown in Figure 3.2. The electrons in the π bond can be removed easily as these are weakly bonded in π bond than in σ bond [77].

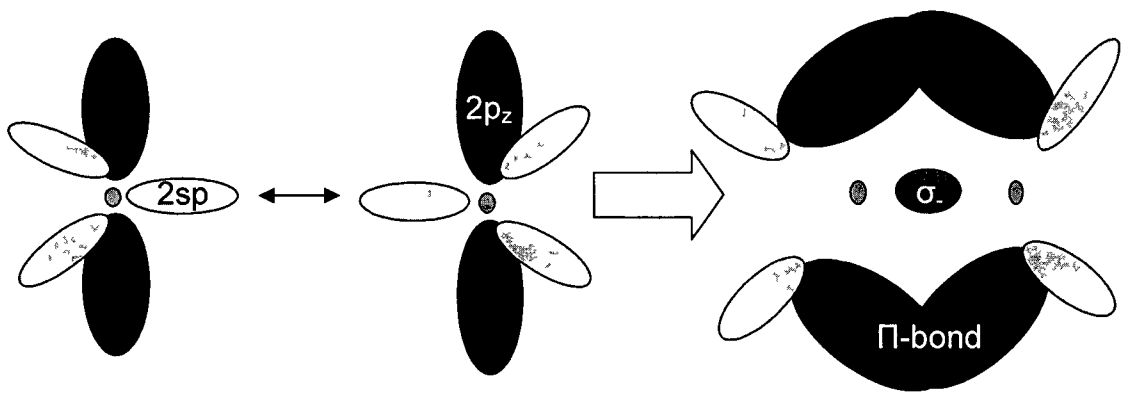

Figure 3.2 Formation of σ and π bonds due to the overlapping of $2sp^2$ and $2p_z$ orbitals [77].

Conducting polymers are divided into two groups: degenerate ground state and non-degenerate ground state polymers depending on their geometry. Single and double bonds can be interchanged in degenerate ground state without changing the ground state energy, while the interchange of these bonds leads to formation of two energy levels in non-degenerate ground state [15]. For example, polyacetylene is divided into degenerate ground state trans-polyacetyele and non-degenerate ground state cis-polyacetylene as depicted in Figure 3.3.

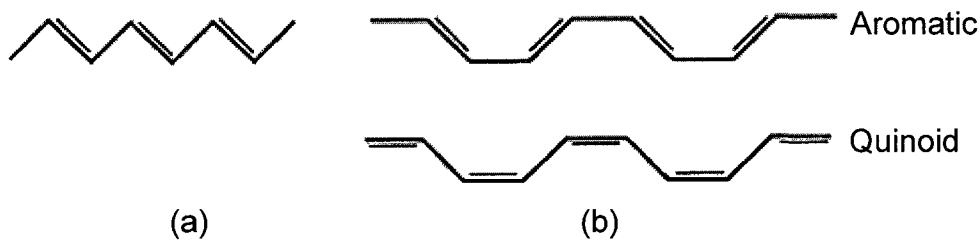

Figure 3.3 (a) Trans-polyacetylene, (b) Cis-polyacetylene [15].

The conductivity of conducting polymers in their intrinsic state is in the range between insulators and semiconductors (10^{-10} to 10^{-5} S cm^{-1}) indicating that the conjugated double bonds are not enough to make them electrically conductive. The process of making them electrically conductive by adding impurities or disrupting the bonds by oxidation (removing electron) or by reduction (adding electron) is called doping. The conductivity level of the polymer can be adjusted by varying the doping. The conductivity can be modulated in the range of (1 to 10^4 S cm^{-1}) by altering the temperature, pressure, and by using secondary dopants such as water molecules, protons and oxidizing/reducing gaseous molecules [78]. Figure 3.4 depicts the conductivities of different organic and inorganic materials.

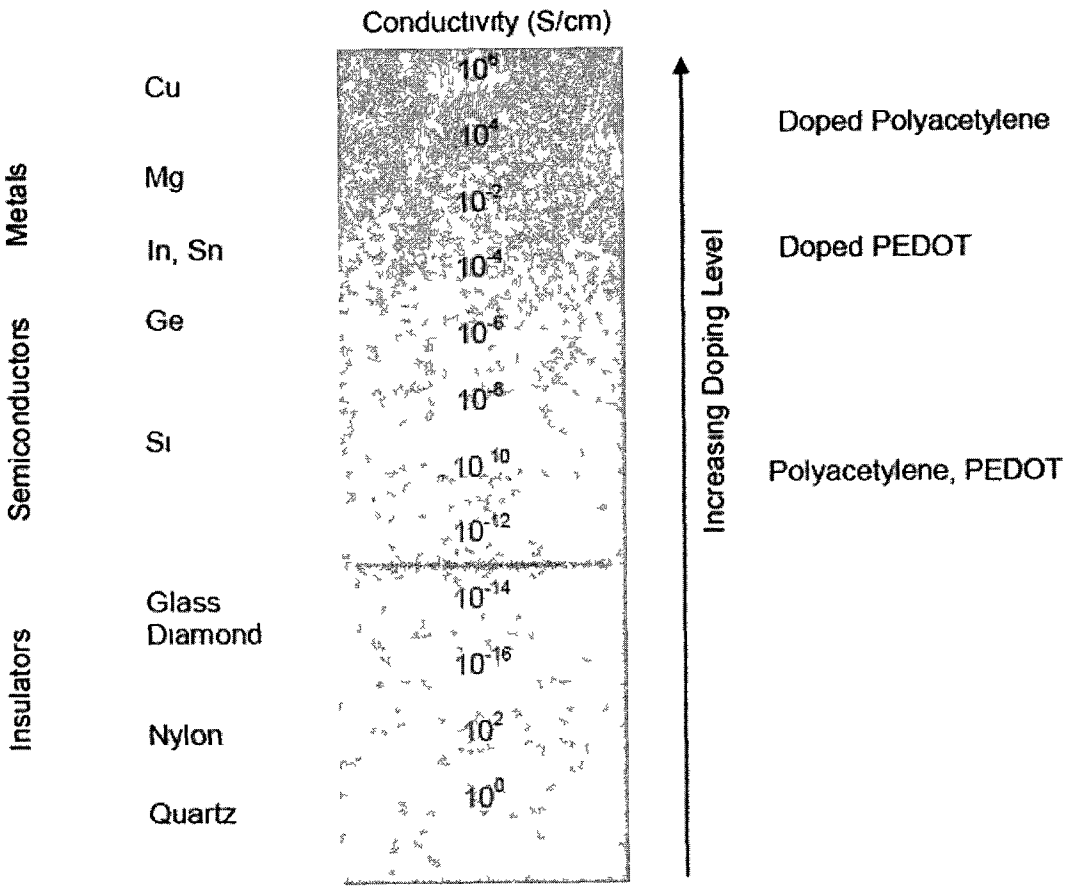

Figure 3.4 Conductivities of few organic and inorganic materials [75].

Semiconductors such as silicon and germanium need only a small fraction of donor and acceptor dopants for significant conductivity, while in conducting polymers, dopants must be occurred in high fraction to increase the conductivity. Chemical and electrochemical doping approaches are widely used among the available chemical, electrochemical, photo, and charge injection doping techniques [79]. Conductive polymers can be either positively or negatively doped. P-doping can be achieved by polymer oxidation with the injection of holes to depopulate the HOMO bonding orbital [80]. It can also be done by removing electrons from the π bond of the polymer backbone and this results in the formation of polymeric cation from neutral polymeric chain according to the Eq. 3.1:

$$P + yA^- \rightarrow P^{y+}A_y^- + ye^-, \tag{3.1}$$

where P denotes polymer chain, y is the number of counter ions, A denotes the charge-compensating counter ion, and e^- is the electron.

N-doping process involves the injection of electrons (excess donors) in the LUMO orbital. The addition of electrons to the π-system of polymer chain forms polymeric anion as described in Eq. 3.2 [81]:

$$P + ye^- + yA^+ \rightarrow P^{y-}A_y^+. \tag{3.2}$$

The addition or removal of electrons to the polymer structure through oxidative or reductive doping generates quasi-particles such as solitons, polarons, and bipolarons [82]. In degenerate systems, such as trans-polyacetylene, the combination of two conjugated polymer chain segments of different bond order creates neutral soliton, a defect in the form of unpaired electron and this unpaired electron forms a new energy level inside the band gap. Neutral solitons possess no charge and a spin of ½ and they can be detected experimentally because of their spin [82-86]. The addition and removal of electrons to the polymer chain through doping creates a negative and a positive solitons without a spin respectively as depicted in Figure 3.5.

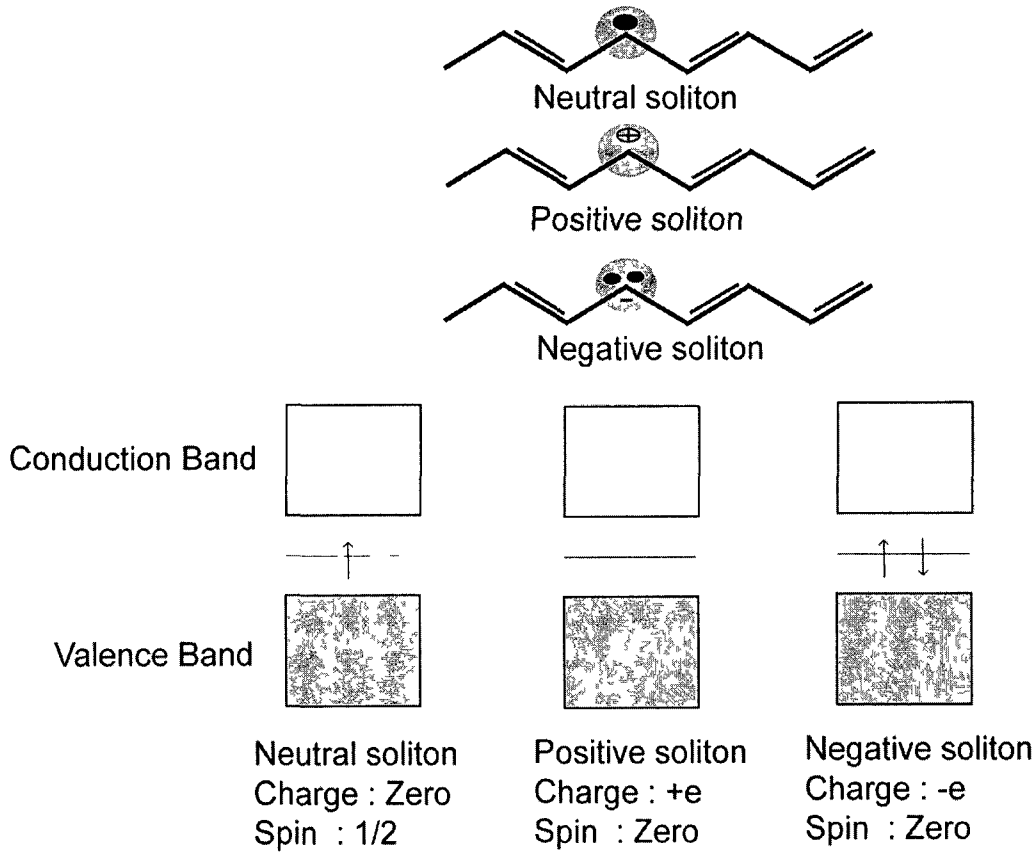

Figure 3.5 Solitons in degenerate conjugated polymers [84].

The doping of non-degenerate conjugated polymers induces a state of higher energy. The distortion in the bond order associated with the introduced charge is called a polaron. These polarons overcome energy activation barrier while moving along the polymer chain to participate in the electronic conductivity. Polarons formation in a non-degenerate conjugated polymer poly (3,4 ethylenedioxythiophene) (PEDOT) is depicted in Figure 3.6. Doping of this conjugated polymer yields a geometrically distorted quinoid form from aromatic form upon creating a polaron. Sometimes further doping forms doubly charged, spinless bipolarons, rather than two separate polarons [86]. The bipolarons will be localized over a few rings, because two charges in bipolarons repel each other due to Coulomb forces and the requirement of the elastic energy to separate two polarons.

Further oxidation of the polymer generates bipolaron energy bands in the band gap [87, 88].

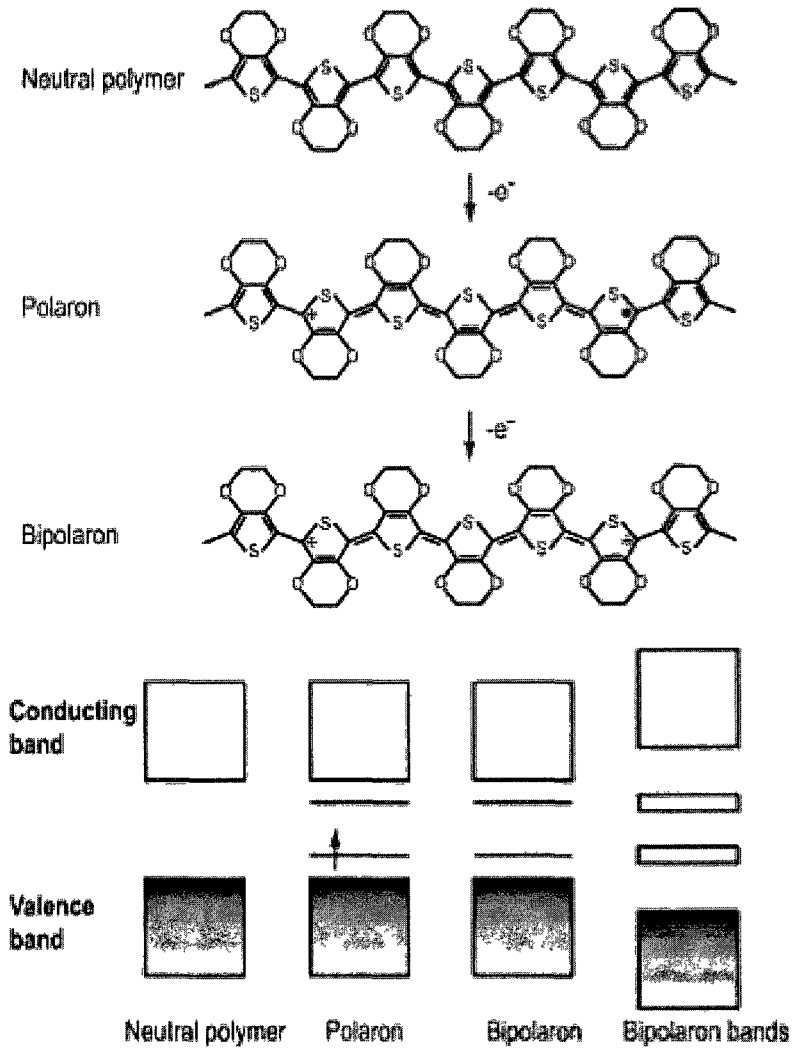

Figure 3.6 Positive polaron and bipolaron formation and energy levels of the neutral polymer, a polaron, a bipolaron, and bipolar energy bands in PEDOT [88].

The doping enhances the conductivity in conjugated polymers considerably. The conductivity σ is defined according to Eq. 3.3:

$$\sigma = ne\mu, \tag{3.3}$$

where n denotes number of charge carriers, e is the charge of an electron, and μ denotes charge carrier mobility. The enhanced conductivity in conjugated polymers can be attributed to two reasons: availability of more charge carriers and an increase in the mobility of charge carriers due to the formation of new electronic bands [89]. However, the conductivity starts to cease if the number of charge carriers reaches beyond certain a number due to the charge carrier interactions. Measurements on conjugated polymers polythophenes, polpyrroles, and polyaniline revealed that high conductivity is achievable only for a finite potential window. In polyaniline, the conductivity reaches maximum when it is oxidized to a level of 0.5 electrons per repeat unit and starts decreasing beyond this level [90].

3.1.2 Electrochromism in Conducting Polymers

Conducting polymers absorb light in the visible region (wavelength, λ=400-800 nm). Doping can also alter the optical properties of the conjugated polymers along with the electrical properties, as the absorption corresponds to difference in energy states. Introduction of new energy state through doping forces the absorption to shift towards lower energies as shown in Figure 3.7. So, the color transition can be observed visually upon doping. Several conducting polymers can be electrochemically doped in order to change both electrical conductivity and color. The phenomenon of altering color upon electrochemical switching is called electrochromism [91, 92]. Polythiophenes and its derivates are examples of common electrochromic polymers. The color of the polymer material can be modified by adding chains to the conjugated polymer or by altering the effective conjugation length. Therefore, a polymer with required color absorption can be designed to some extent by modifying the energy level configuration [93]. Electrochemical

displays [94] and autodimming windows [95] are some of the fine examples for organic electrochromic materials.

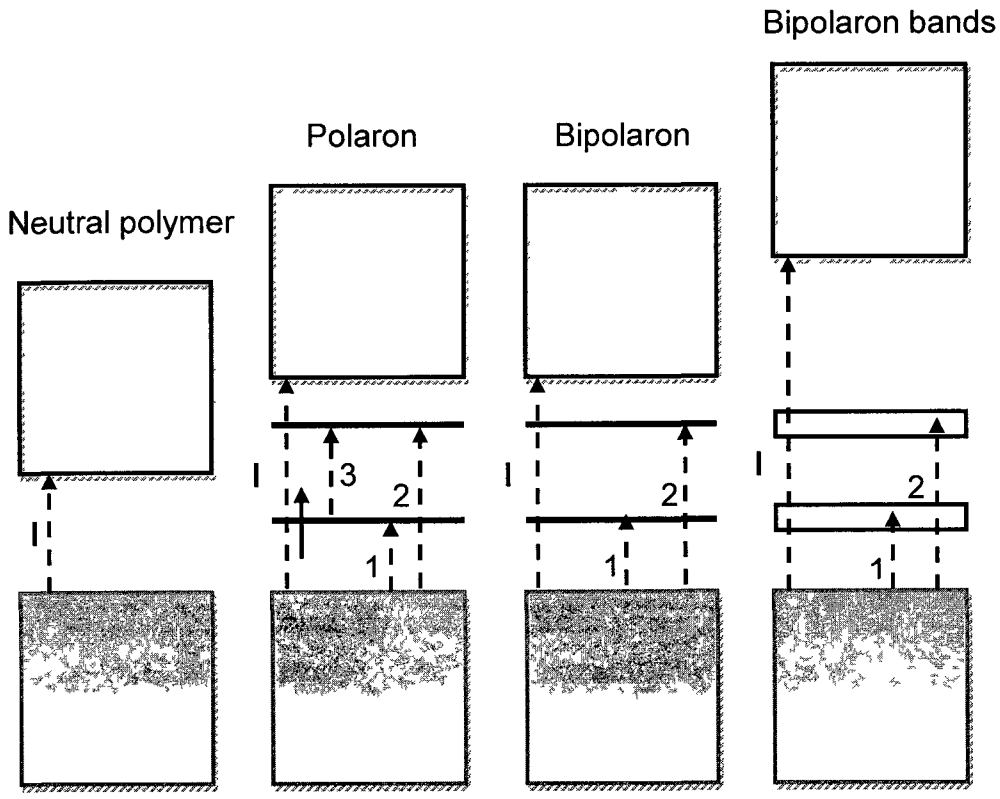

Figure 3.7 Schematic representation of optical transmission with the increasing doping level from left to right [84].

3.1.3 Ionic Conduction in Conjugated Polymers

Conjugated polymers conduct not only electrons but also ions. This makes them potential materials for applications such as ion-to-electron transducers, organic neutral electrodes, artificial muscles, sensors and drug release devices [96-101]. Ion conductivities in polymer-polyelectrolyte systems are equal or more than equal to those found in aqueous solutions [102, 103]. The polymer film swells with the arrival of ions from the aqueous solutions, therefore increasing the ion conductivity. The ion transportation mechanism can be either diffusion or electromigration, depending on applied electric field

and ion gradient [104]. Conducting polymer poly(3,4-ethylenedioxythiophene) poly(4-styrenesulfonate) (PEDOT:PSS) is a fine example of porous, phase separated material, with electronically conducting PEDOT islands separated by insulating PSS grains. Therefore, ion conduction occurs through hygroscopic PSS grains and is independent of PEDOT oxidation state [105].

3.1.4 Conducting Polymer-PEDOT:PSS

Poly(3,4ethylenedioxythiophene) (PEDOT) was developed by Bayer AG in the late 1980s and is one of the widely used, studied and characterized p-doped polythiophene derivative [106]. Figure 3.8 displays the numerous applications of PEDOT [16, 94, 107-120].

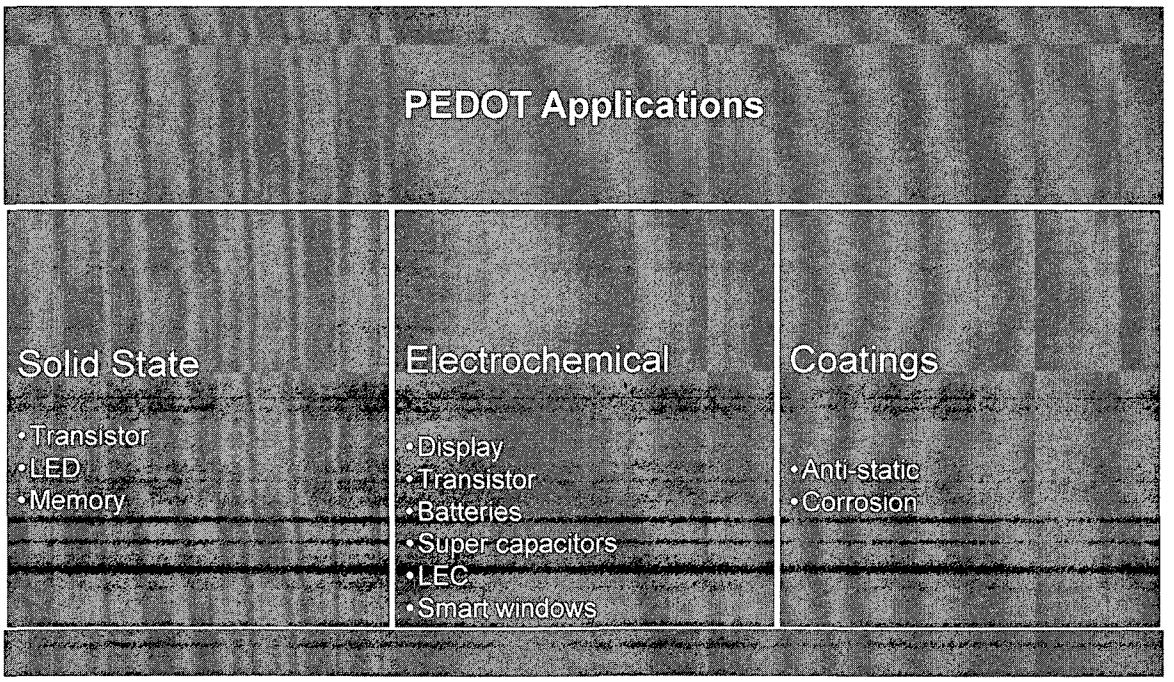

Figure 3.8 Various applications for PEDOT.

Excellent electrochemical stability in oxidized states, moderate band-gap with good stability in doped states, optical transparency in visible region and promising

conductivity due to the planar structure that allows effective π electron delocalization attributes to the abundant applications of PEDOT [121, 122]. It is made up of ehtylenedioxythiphene (EDOT) monomers and insoluble in many common solvents and is unstable in its neutral state due to its rapid oxidizing property in air. The insoluble PEDOT is mixed with a charge balancing polyelectrolyte counter ion poly(styrenesulfonate) (PSS^-) to form a water soluble Poly(3,4ethylenedioxythiophene) poly(4-styrenesulfonate) (PEDOT:PSS). Ionic interactions link PEDOT and PSS chains strongly to form ionic polymer complex. As depicted in Figure 3.9, each monomer styrene ring has one acidic SO_3H group. PEDOT carries the positive charge and part of the sulfonate groups carry the negative charge [123].

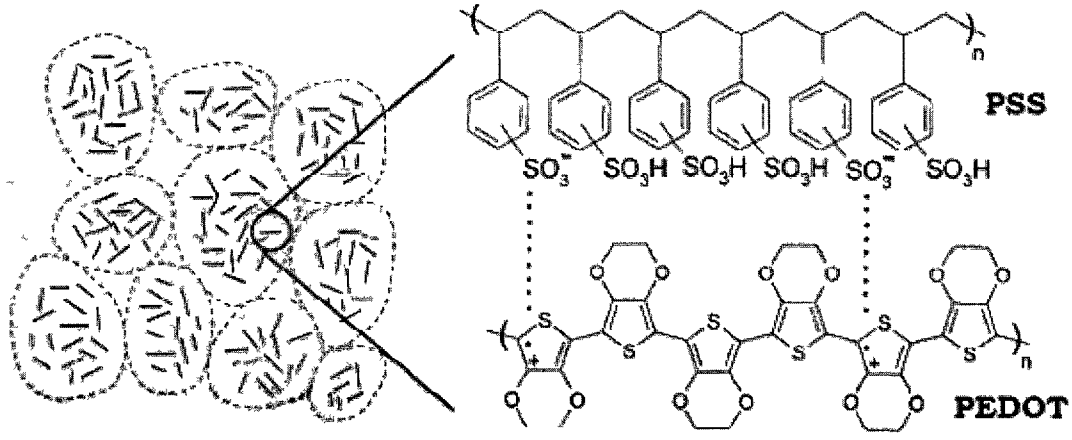

Figure 3.9 Chemical structure of PEDOT:PSS [124].

The PEDOT:PSS film morphology is a phase segregated conductive PEDOT:PSS grains bounded by insulating PSS boundary of 40 Å thickness. The PEDOT:PSS grains show electrical conductivity similar to metals, but they are surrounded by PSS ion conductors as illustrated in Figure 3.9, i.e. the charge transporters freely move along the grains; however, they are obstructed by grain boundaries [105].

Aqueous PEDOT:PSS forms films with a conductivity in the range of 10 S/cm. However, it can be improved up to several orders of magnitude upon doping. Addition of ethylene glycol (EG) to aqueous solution of PEDOT:PSS yield a conductivity enhancement by two orders of magnitude. This high conductivity enables this polymer to use as electrode material and J. Oouyang et al. reported that devices made of EG-PEDOT:PSS anodes showed similar performance to those of indium tin oxide (ITO) anodes [125]. The conductivities of untreated PEDOT:PSS, ethylene (E) treated PEDOT:PSS, ethylene glycol treated PEDOT:PSS and ITO films were illustrated in Table 3.1.

Table 3.1 Conductivities of ITO, PEDOT:PSS, and treated PEDOT:PSS films [125].

Materials	**Conductivity (S/cm)**
PEDOT:PSS	0.4
EG-PEDOT:PSS	160
E-PEDOT:PSS	155
ITO	155

PEDOT:PSS is dark blue in its neutral semiconductor state and is transparent in oxidized dope state. The high conductivity, good electrochromic properties along with excellent chemical and mechanical stability make it an ideal candidate in developing all-organic electrochemical devices. The applications of PEDOT:PSS extends to light emitting diodes [123, 126, 127], solar cells [128, 129], electrochromic displays [94],

electrochemical transistors, logics [16, 130], sensors [80, 99, 131], and bio-electrodes [132, 133].

3.2 Organic Thin Film Transistors

Organic thin film transistors (OTFT) use conjugated polymer films as active material, while daily used semiconductor devices such as filed effect transistors (FET) and light emitting diodes (LED) use silicon as active material. OTFTs can be fabricated on flexible substrates at low temperatures using simple fabrication techniques such as casting, spin coating, and printing. OTFTs can be divided into organic field effect transistors (OFET) and organic electrochemical transistors (OECT) and has potential applications in biosensors, electrochemical displays, logic circuits, ion selective membranes, electrochemical circuits [107, 108, 134].

3.2.1 Organic Field Effect Transistor (OFET)

OFETs are fabricated using thin film technologies and Figure 3.10 illustrates the schematic architecture of OFET. Source (S), drain (D), and gate (G) electrodes can be made of either metals or highly conducting polymers such as PEDOT:PSS. Flexible substrates such as polyester, polyethylene, and polyimide can be used as carrying substrates and thin films of polyimide or polymethacrylate serve as dielectric layer between gate and the polymer channel [135, 136].

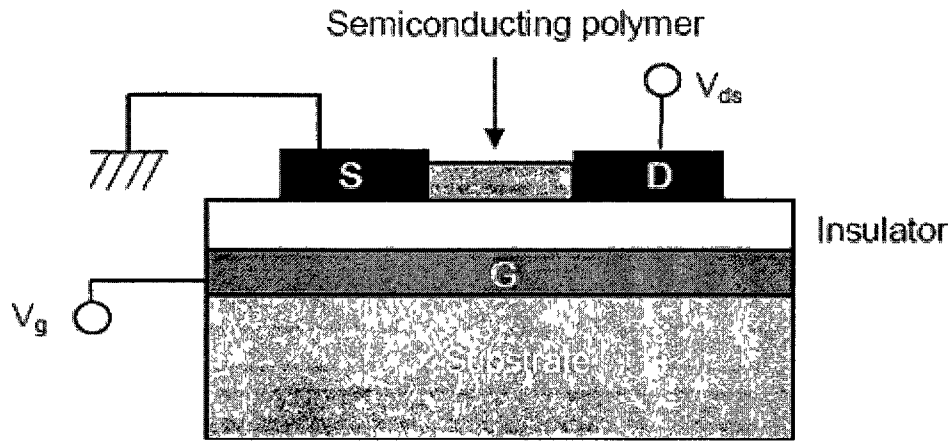

Figure 3.10 Typical architecture of organic field effect transistor (OFET) [22].

The basic principle of FET involves the modulation of charge carrier density through the capacitive coupling between gate and transistor channel. The application of gate voltage (V_g) accumulates charge carriers at the insulator-semiconductor interface. The relationship between drain voltage (V_d) and drain current (I_d) is linear at lower V_d and the thickness of the conducting channel ceases to zero at one end of the polymer as V_d reaches saturation voltage (V_{dsat}). This is denoted as the pinch off and beyond this pinch off voltage I_d essentially saturates and the transistor acts as an amplifier. The drain current (I_d) can be controlled by varying V_g by altering the density of accumulated charges at the insulator-semiconductor interface as illustrated in Figure 3.11.

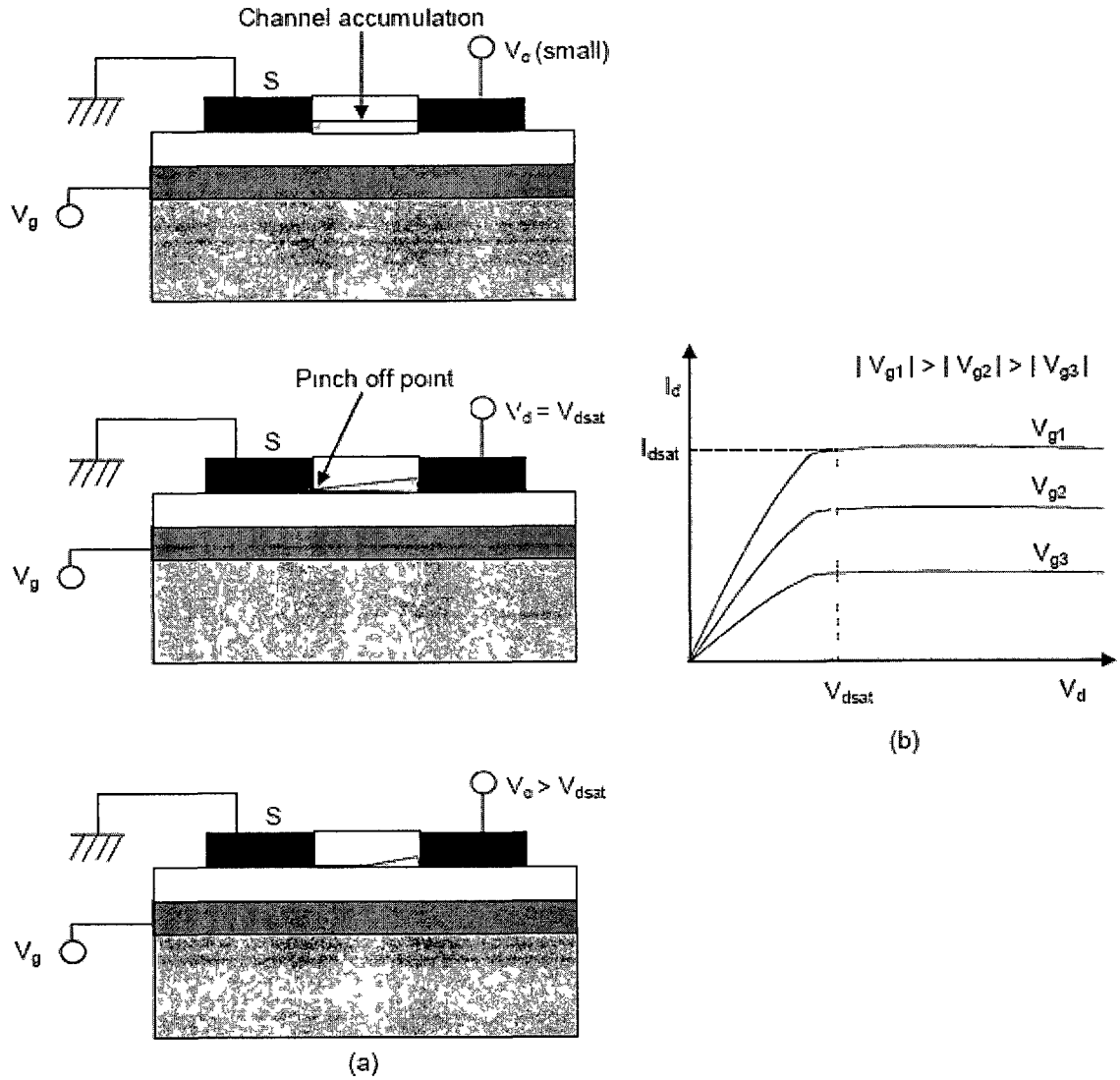

Figure 3.11 (a) FET operation with the application of gate and drain voltages (b) Transistor characteristics of FET [22].

3.2.2 Organic Electrochemical Transistor (OECT)

Wrighton et al. [137] reported first organic electrochemical transistor (OECT) in 1984 using polypyrrole as active material. Recently, these devices have gained a significant attention due to their simplified structure, low operating voltages and aqueous environment compatibility [73]. Many conjugated polymers such as polythiophene and polyaniline derivatives have been explored for OECTs besides polypyrrole [23, 138, 139].

Polymer based OECTs can be fabricated using standard photolithography, screen printing, soft embossing, microcontact printing and inkjet printing techniques [8-14].

A typical OECT consists of source (S), drain (D), and gate (G) electrodes; a thin film of semiconducting/conducting polymer in its doped state and an electrolyte medium in contact with gate and channel as depicted in Figure 3.12. If the polymer is highly conductive, all the electrodes and the channel can be made using the same polymer without using any metals for electrodes resulting in all polymer electrochemical transistor. Depending on the application, the electrolyte can be a liquid, a solid or a gel [80, 140-142].

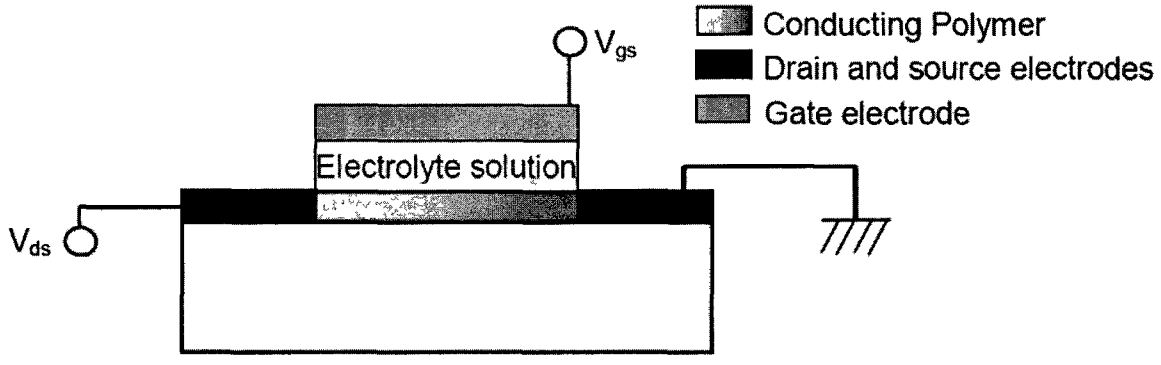

Figure 3.12 Schematic illustration of typical OECT [73].

In OECTs, the application of gate voltage (V_{gs}) through the electrolyte medium modulates the conductivity of polymer film due to the migration of ions between electrolyte and semiconducting polymer film. More specifically, ions from the electrolyte jump into the polymer film with the application of gate voltage and migrate back into the electrolyte upon the removal of applied gate voltage altering the doping level of the active area. This doping and dedoping effects the channel current (I_{ds}) that can be measured by simple current measurement setup [143].

3.3 PEDOT:PSS based OECT

High conductivity, stability in a wide pH range and commercial availability of the conducting polymer PEDOT:PSS are the driving forces behind developing a complete PEDOT:PSS based OECT. The device was fabricated using a simple, inexpensive and rapid fabrication process that involves xurography technique to make physical tape masks.

3.3.1 Fabrication Process

The fabrication process uses a Kapton tape as a physical mask material to pattern the polymer on the substrate. A computer controlled cutting plotter was used to cut the tape according to the desired window dimensions followed by removing the tape in the region of interest. The fundamental fabrication process involves the following steps and is depicted in Figure 3.13.

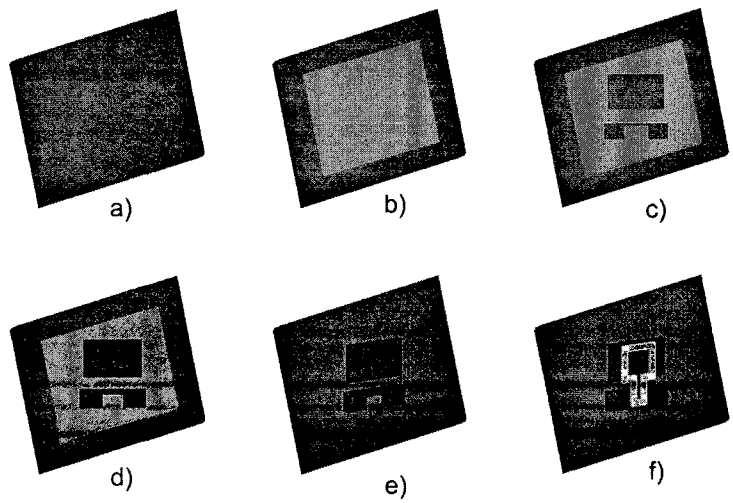

Figure 3.13 Schematic illustration of OECT fabrication (a) Pretreat substrate (b) fasten patterned polyimide tape (c) strip patterned region (d) spin coat PEDOT:PSS (e) peel unwanted tape (f) fasten polymer well (g) final device with electrolyte solution.

3.3.1.1 Substrate cleaning

Fisher Scientific plain microscope glass slides of dimensions 76.2 mm × 25.4 mm × 1 mm and 3M Ink Jet transparency polyester sheet of approximate thickness 100 μm were used as two substrate materials for OECT. The substrate was cleaned using an alconox detergent solution (10 g/L) followed by treating it with acetone, isopropyl alcohol (IPA) to remove organic and inorganic impurities. Later, it was rinsed off with deionized water and dried in nitrogen air and the excess moisture on the surface was removed by drying it on a hotplate at 150° C for 2 min.

3.3.1.2 Mask preparation

A computer controlled cutting plotter was used to cut the physical tape mask according to the specified design. This tape was attached onto the substrate followed by removing the tape in the regions of interest using tweezers. This leaves a polyimide tape on the substrate with certain openings as depicted in Figure 3.13 (c). Later, it was heated on a hotplate at 150° C for 2 min to improve the bond strength of the tape with the substrate.

3.3.1.3 Oxygen plasma treatment

The substrate was subjected to oxygen plasma treatment for 1 min to hydrophilize the surface using Technics Micro-RIE Series 800 with the parameters illustrated in Table 3.2.

Table 3.2 Micro-RIE parameters for oxygen plasma treatment.

Gas	Flow rate (sccm)	Power (W)	Pressure (mTorr)	Time (min)
Oxygen	30	300	300	1

3.3.1.4 Polymer deposition

A 4 mL of PEDOT:PSS (Clevios^{TM} P from H.C. Stark Inc.) was mixed with 1 mL of ethylene glycol (anhydrous 99.8%) (Sigma-Aldrich) and 10 μL of linear alkylbenzene-sulfonic acid (97%) (Alfa Aesar) to enhance the conductivity and film formation, respectively [144]. The dispersed PEDOT:PSS solution was spin coated on the oxygen plasma treated substrate using Specality Coating Systesms G3P-8 Spin coat. Figure 3.14 depicts the spin coating parameters for polymer solution.

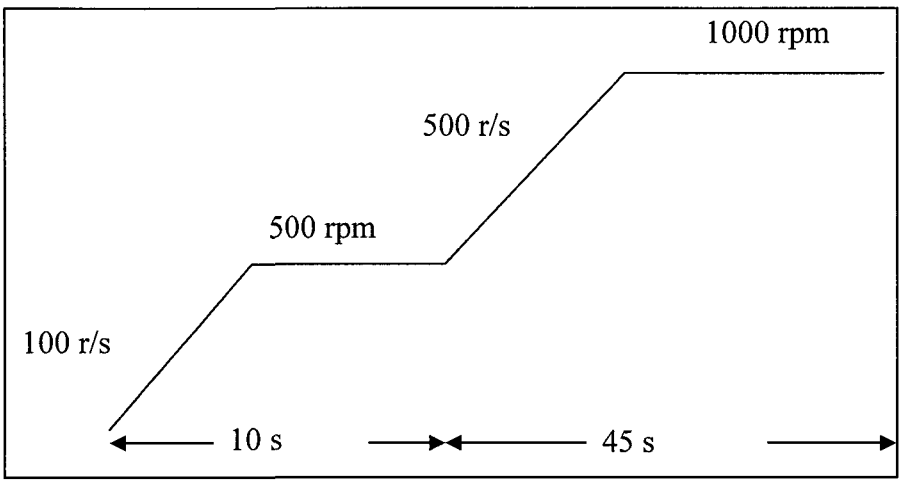

Figure 3.14 Parameters for polymer coating.

3.3.1.5 Polymer annealing and stripping

After spin coating the polymer solution, the substrate was annealed in air at 150° C for 30 min. The annealing was carried out under a hood, as the polymer solution releases mild toxic fumes during the heating process. These toxic fumes were due to the presence of DBSA in the dispersed polymer solution. The subsequent stripping of excess tape left two patterned PEDOT:PSS stripes on the substrate as depicted in Figure 3.13 (e). The film thickness was measured to be 200 nm using a KLA Tencor surface profiler. Figure 3.15 depicts the surface roughness profile of the film measured using atomic force

microscopy (AFM). The film is relatively smooth and some PEDOT:PSS nanoclusters were found on the surface.

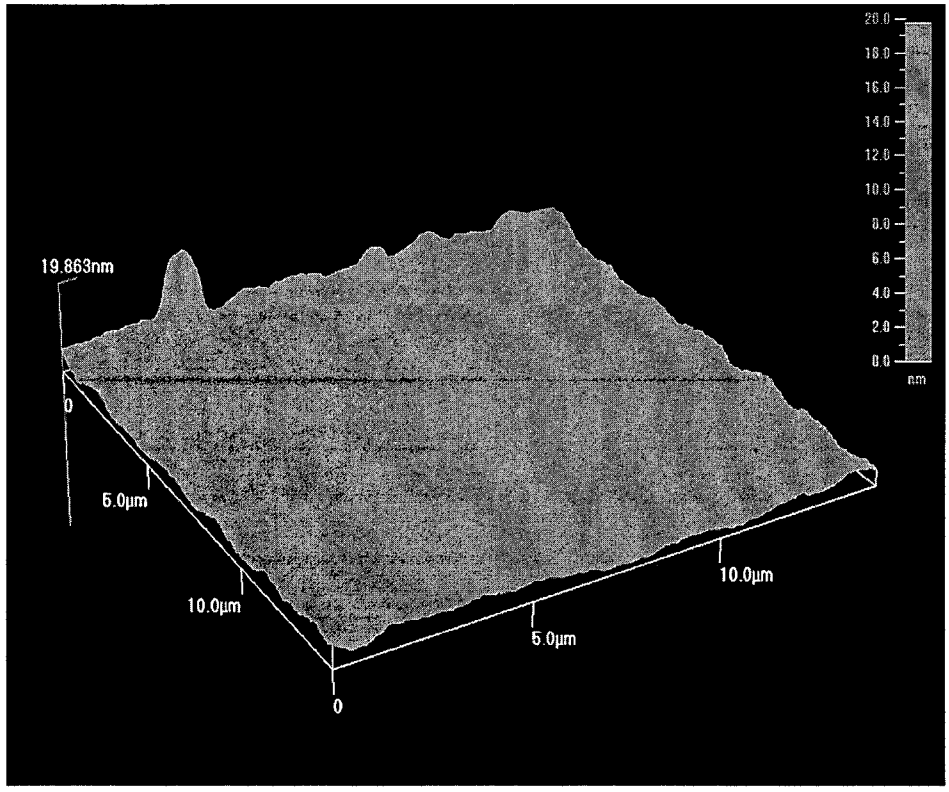

Figure 3.15 PEDOT:PSS film surface profile.

3.3.1.6 Preparing polymer wells

A polyester sheet of approximate thickness 120 μm was attached to an 80 μm double sided tape resulting in a 0.2 mm thick polymer sheet. It was cut by a computer controlled cutting plotter according to the mask design, followed by stripping of the unwanted regions to make polymer wells. Figure 3.16 depicts the polymer well preparation. Three of these wells were stacked together and attached onto the PEDOT:PSS stripes. The stack of these polymer wells accommodates electrolyte, enzyme, and analyte solutions and thus is the home to enzymatic reactions. Care has to be taken while stacking the

polymer wells on the polymer stripes, as misalignment in the stacking may cause solution leakage through the gaps, thus affecting the device characteristics.

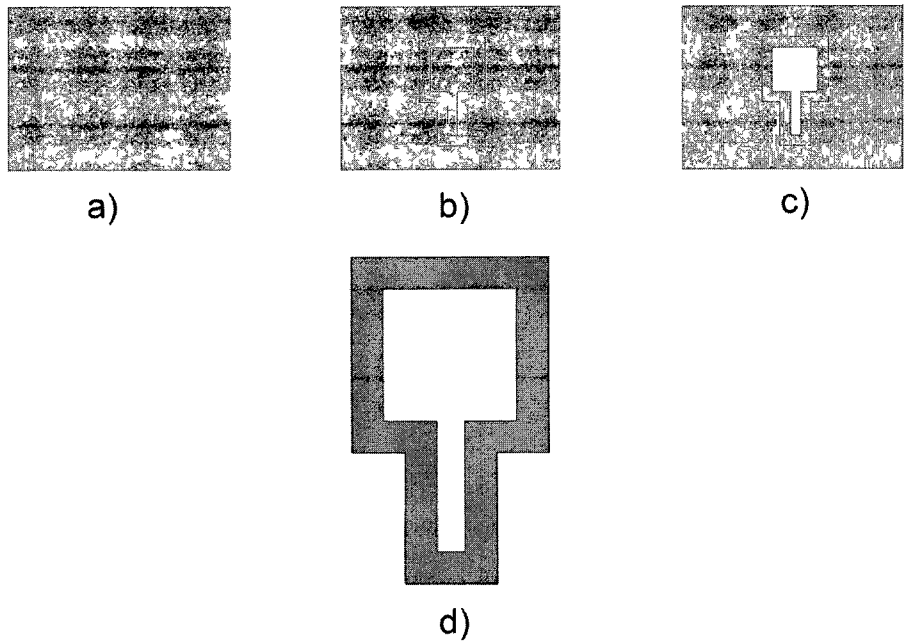

Figure 3.16 Polymer well preparation (a) attach double sided tape to polyester sheet (b) pattern the polymer sheet (c) remove unwanted region (d) strip the well from polymer sheet.

3.3.2 OECT Device Description and Dimensions

The patterned PEDOT:PSS stripes along with confined electrolyte solution constitutes organic electrochemical transistor (OECT). Figure 3.17 depicts the OECTs fabricated on both glass and flexible polyester sheets.

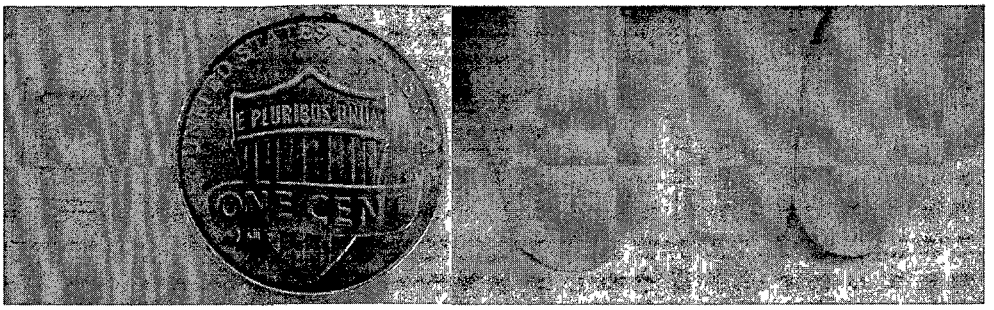

Figure 3.17 Fabricated organic electrochemical transistor on glass slide (left) and polyester sheet (right). The overall dimensions of the device are 9 × 11 mm.

Three dimensional schematic of the final device after loading electrolyte solution was shown in Figure 3.18. The overlap of the electrolyte with the area of the PEDOT:PSS film in between source and drain electrode defines the transistor channel. The channel and gate areas are 0.8 × 0.8 mm^2 and 8 × 6 mm^2 respectively and the distance between the gate and channel stripe is 2 mm. The active surface area of the device after attaching the well is 4.8 × 4 mm^2. The number of available oxidation sites of the gate electrode must be equal to or exceed the number of available reduction sites in the channel to achieve maximum reduction of the channel which was achieved by making the gate area larger than the channel area. The dimensions of the gate and transistor channel and the distance between them greatly determine the device properties including the extent of gating, transient response time, On/Off ratio, switching speed and sensitivity [145, 146]. Highest On/Off ratio was achieved with a square shaped transistor channel.

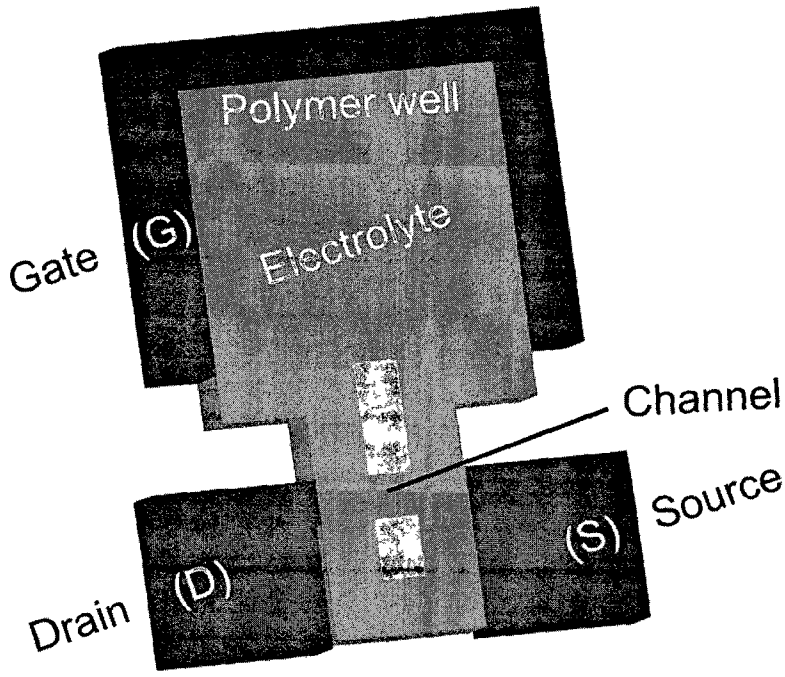

Figure 3.18 Three-dimensional schematic of final device.

3.3.3 Polymer Well Effect on Film Conductivity

The effect of polymer well on the film conductivity was measured by measuring the drain current for various drain potentials at a constant gate potential of 0.2 V before and after attaching the polymer well to PEDOT:PSS film stripes. The deviation in the drain current was very small in the presence of the polymer well as shown in Figure 3.19. Therefore polymer wells were used to confine the electrolyte solution.

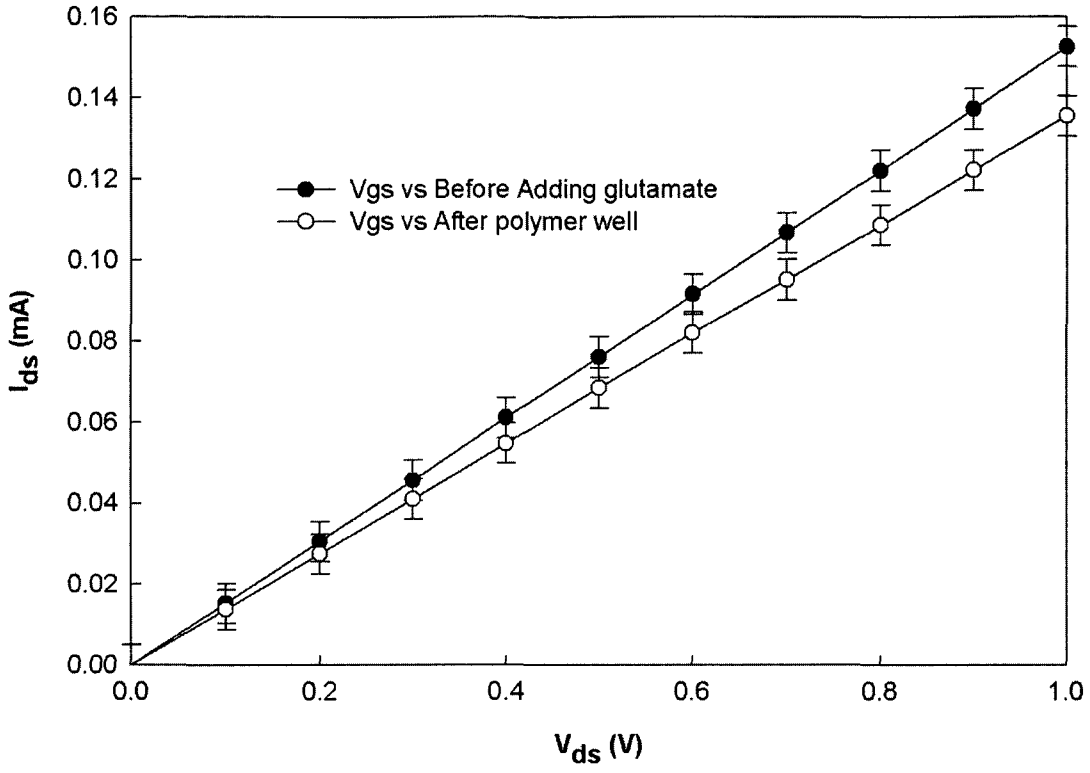

Figure 3.19 Deviation in drain current for various V_{ds} at V_{gs} = 0.2 V.

3.3.4 OECT Characteristics

The device characteristics were measured using two Keithley 236 Source meters controlled by Interactive Characterization Software (ICS). The three Tungsten probes depicted in Figure 3.20 were used to apply the potentials and measure the currents. Drain and gate potentials (V_{ds} & V_{gs}) were applied through two probes on the left side and source was connected to ground terminal using the probe on the right side as depicted in the inset of Figure 3.20.

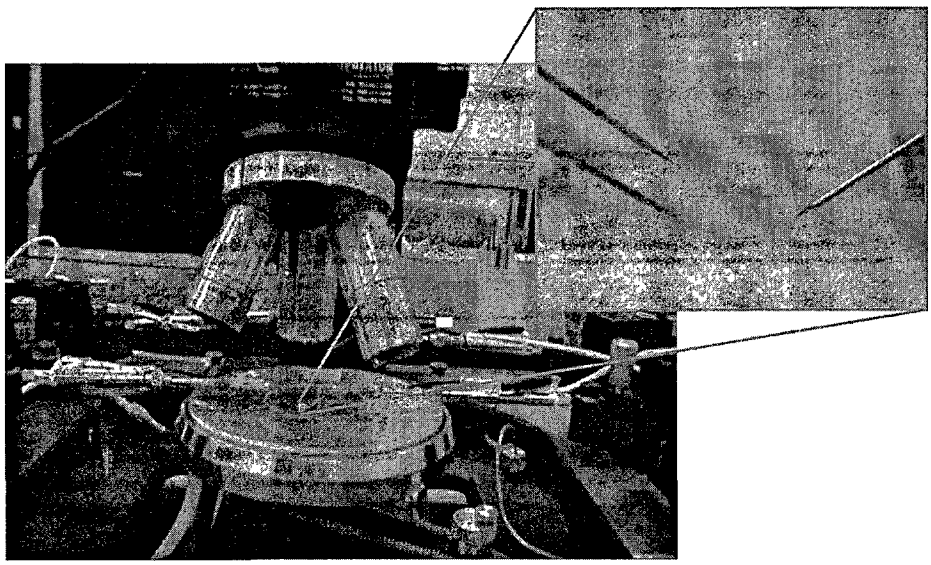

Figure 3.20 Micromanipulator electrical probe station and OECT measurement setup (inset).

Phosphate buffered saline with calcium chloride and magnesium chloride (PBS) (Sigma–Aldrich) and Tris-Hcl (Tris) were used as liquid electrolyte solutions for OECT under consideration; 15 μL of electrolyte solution was loaded into the transistor well and was allowed to sit for 2 min to allow the electrolyte ions to cross link with PEDOT:PSS film. Voltages were applied to the drain and gate terminals by keeping the source terminal at ground potential. The device response was measured by determining the drain current (I_{ds}) that flowed between drain-source terminals and gate current (I_{gs}) current that flowed between gate-source terminals.

Mobile holes in PEDOT:PSS film are compensated by the negatively charged sulfonate groups. The PEDOT:PSS transistor is in the "on" state at zero gate voltage, at which the channel current is high. Application of positive gate voltage turns "off" the transistor as cations from the electrolyte solution were driven into the polymer channel. The migrated ions cause electrochemical de-doping of the PEDOT, thus decreasing the drain current. PEDOT reduction from its highly conductive oxidized state to less conduc-

tive neutral state is reversible and is described according to the electrochemical reaction described in Eq. 3.4: [147].

$$PEDOT^{+}:PSS^{-} + M^{+} + e^{-} \leftrightarrow PEDOT^{0} + M^{+}:PSS, \quad (3.4)$$

where $PEDOT^{+}$ is in its highly conductive oxidized state, $PEDOT^{0}$ is in its less conductive neutral state, M^{+} is a cation in the electrolyte medium, and e^{-} is the electron from the source electrode. Application of the positive gate potential causes the migration of M^{+} ions in the channel, thus reducing the PEDOT:PSS film. These migrated ions diffuse back into the electrolyte medium upon the removal of the gate potential, thus retaining the original conductivity of the channel. The PEDOT:PSS channel can be switched between its oxidized and neutral states with the application of only a few volts.

Figure 3.21 depicts the transfer characteristics of the OECT with 1× tris electrolyte solution. Drain current was measured by sweeping gate voltage from 0 V to 0.8 V with a step size of 0.2 V and a delay of 10 s after each measurement at a drain potential of -0.4 V. The drain current has been decreasing with higher gate voltage, which indicates the gating action of the transistor and can be attributed to the migration of H^{+} ions from tris solution into the PEDOT:PSS channel.

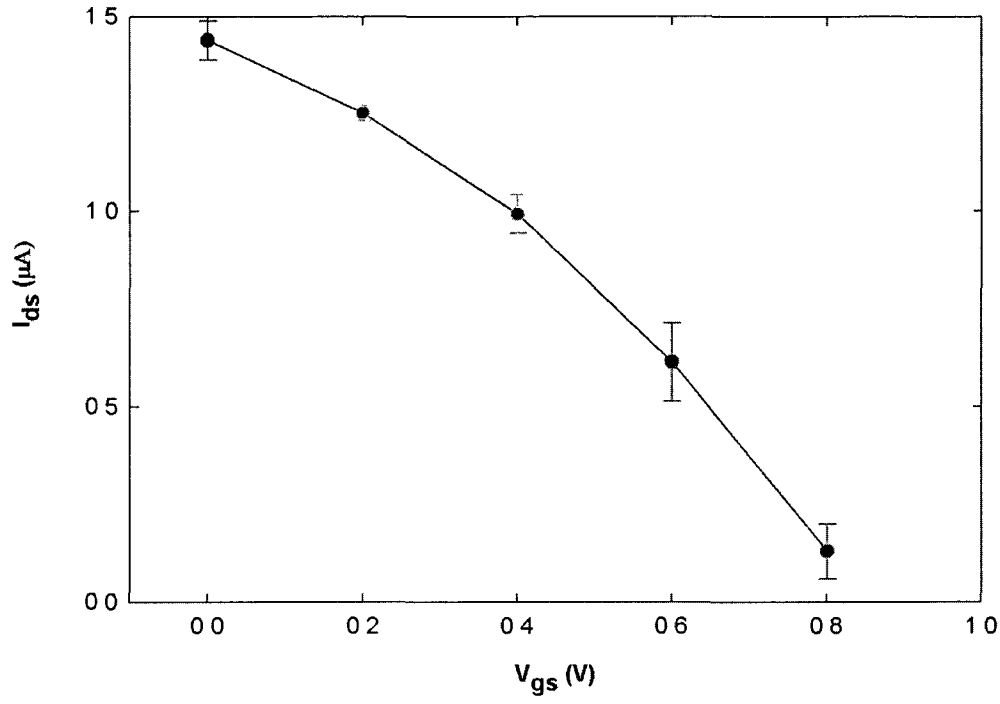

Figure 3.21 Transfer characteristics (I_{ds} -V_{gs}, V_{ds} = -0.4 V) of OECT measured in 1 × tris electrolyte solution.

Figure 3.22 represents the I-V characteristics of the OECT. Drain voltage was swept from -1 V to 1 V with a step size of 0.25 V and a delay of 10 s for each measurement, while varying gate voltage from 0 V to 0.8 V with a step of 0.2 V and a delay of 10 s for each measurement. Drain and gate currents were measured simultaneously with the application of both gate and drain potentials.

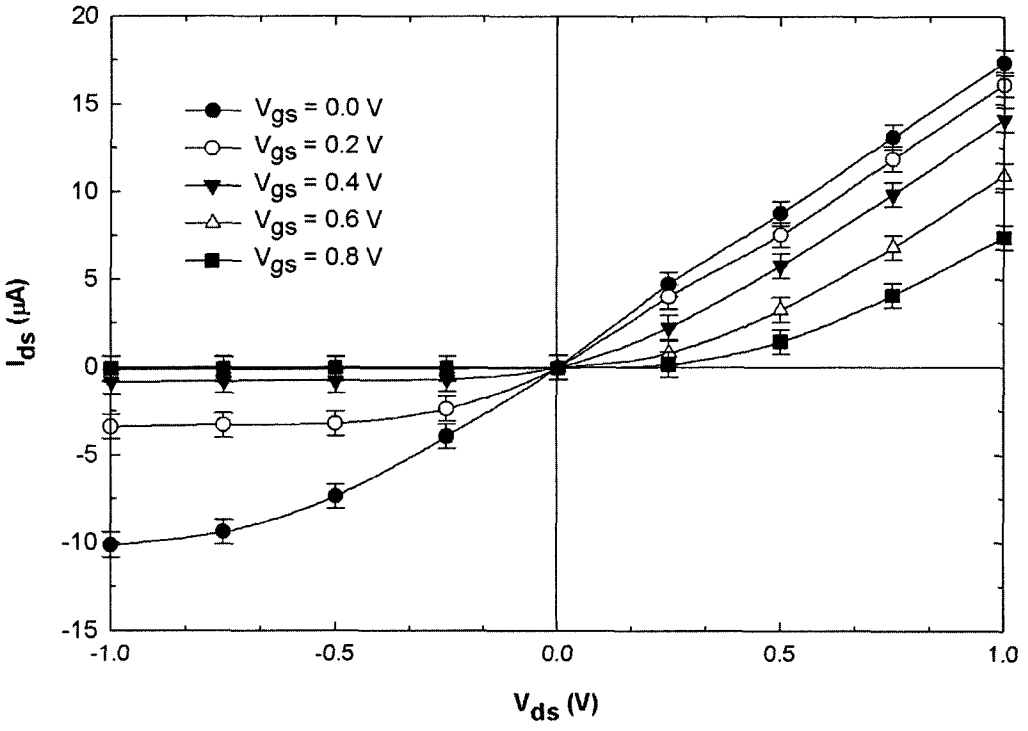

Figure 3.22 Output characteristics of OECT measured at various gate potentials.

From Figure 3.22, it can be observed that there is a linear relation between I_{ds} and V_{ds} for all the gate voltages at lower drain potential in both quadrants. In the first quadrant (upper right), over-oxidation of PEDOT:PSS active area occurs with the application of higher positive V_{ds} which is an irreversible state. In the third quadrant (lower left), the drain current starts to remain constant and eventually saturates. In the third quadrant, the application of V_{gs} = 0.2 V resulted in about 50% reduction in the drain current compared to V_{gs} = 0 V, although the exact percentage depends on the drain voltage, which is in agreement with the earlier reports [148]. The device characteristics are similar to p-type MOSFET, as PEDOT:PSS is a p-type conducting polymer.

3.3.5 Device Stability Test

The OECT characteristics were measured over 30 days to observe the stability of the device characteristics. Drain current was measured by sweeping drain voltage from 0-1 V with a step of 0.2 V, by keeping gate potential at 0.4 V. The device was enclosed in a glass box and kept at room temperature after each measurement. As shown in Figure 3.23, the drain current has been decreased by half in the second day. Later, the reduction in the drain current is small and after 30 days the drain current was decreased by 10-fold. The reduction in the drain current is due to the effect of humidity and environment on PEDOT:PSS film.

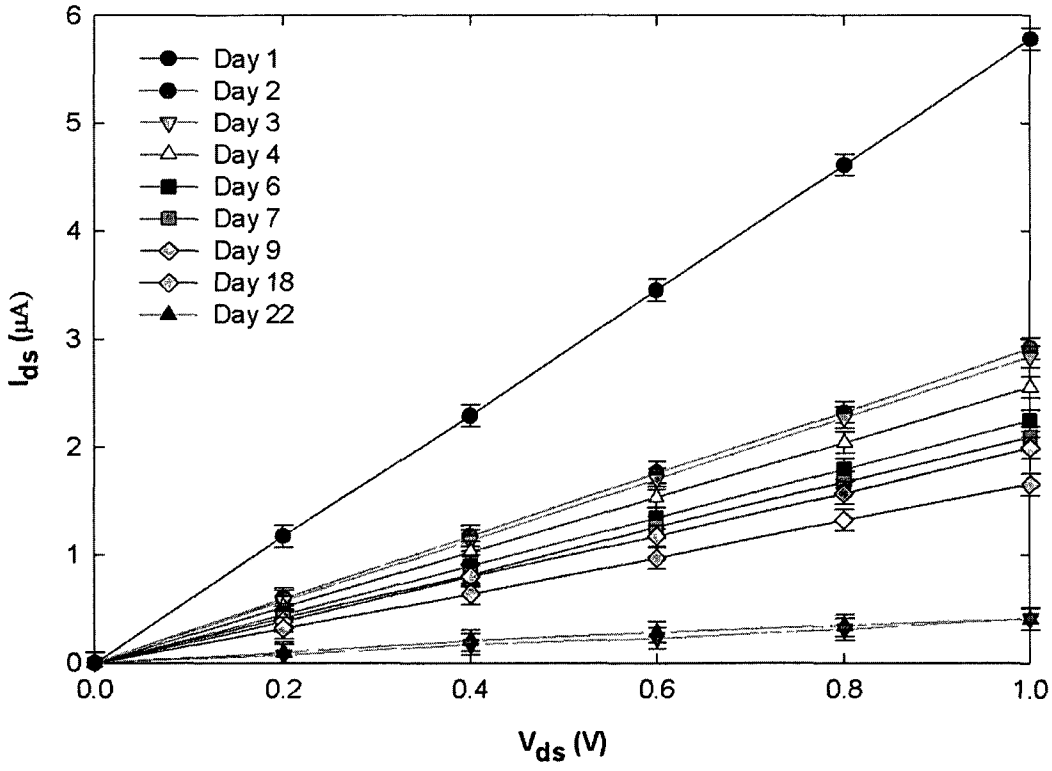

Figure 3.23 OECT drain current as a function of drain potential over several days.

3.3.6 Effect of pH on OECT Characteristics

The effect of pH on the OECT response was monitored using different buffer solutions with different pH values ranging from pH 4 to pH 9. Buffer solutions with different pH values were successively added to the polymer well and the drain currents (I_{ds}) were measured after the addition of each solution by sweeping gate voltage (V_{gs}) from 0.2 and 0.8 V with a step of 0.2 V at a drain voltage (V_{ds}) of -0.4 V. The drain current was decreasing with higher gate voltages, which confirmed the transistor behavior of the device and the change in pH value did not affect the drain current curve considerably as depicted in Figure 3.24. This stable device responses over a wide pH range can be attributed to the stability of PEDOT:PSS polymer over a wide pH range [149].

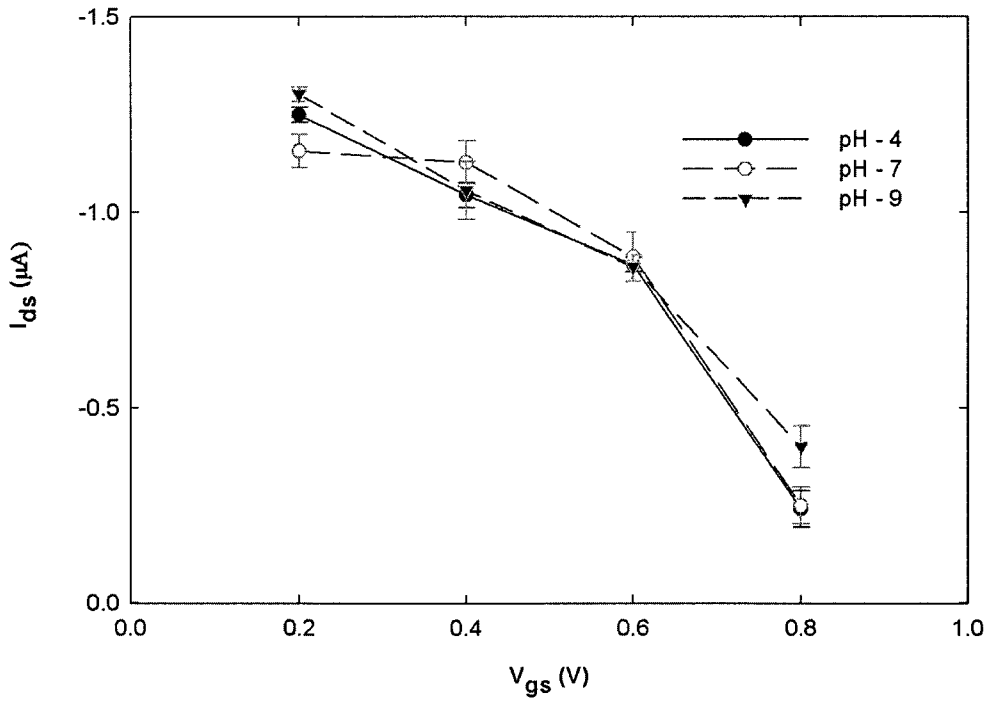

Figure 3.24 Transistor response vs pH. The pH sensitivity of the drain current curve (y-axis) at different gate potentials (V_{gs}) , is shown for three different pH values.

CHAPTER 4

OECTS FOR BIOSENSOR APPLICATIONS

The aim of this project is to develop biosensors using organic electrochemical transistor technology. A glucose sensor and a glutamate sensor were developed using the fabricated OECTs described in Chapter 3. The developed glucose sensor is able to detect glucose concentrations from 1 μM-10 mM and is able to detect glucose levels in the range of those found in human saliva. The developed glutamate sensor showed a linear response from 1-100 μM glutamate concentrations. The glutamate released from astrocytes and glioma cells after stimulating with ATP, KCl and cystine was detected using the developed sensor and the results were compared with standard fluorescent spectrophotometer results. The developed biosensors are simple, inexpensive, and disposable, require very small amounts (5 μL) of enzyme and analyte, does not require enzyme immobilization techniques, and showed a stable response in a wide pH ranging from pH 4 to pH 9.

4.1 Introduction to Biosensors

Biosensors have several applications in biological, chemical, health care, environmental monitoring, and food industries [150]. The modern concept of biosensor dates back to 1962 when the enzyme was immobilized on the electrochemical detectors to sense specific analytes [151]. A biosensor is comprised of interconnected biological sensing element and transducer, as shown in Figure 4.1, to generate electric signal that is proportional to the concentration of a specific or set of analytes. The added analyte diffuses

through the biological sensing element and reaches the reaction site. The transducer picks up the signal generated from the biochemical reactions and translates it mostly to electrical domain [152].

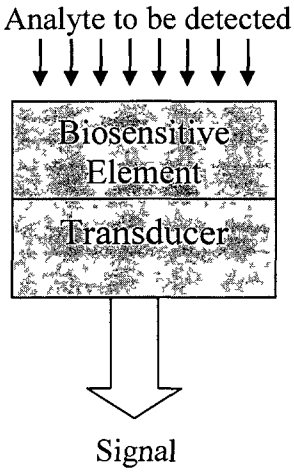

Figure 4.1 Schematic diagram of biosensor.

4.1.1 Classification of Biosensors

Biosensors are classified into three generations depending on the level of integration. The first generation biosensors entrap the biocatalyst in a membrane that is attached on the transducer surface. In the second generation biosensors, biological active component is covalently adsorbed on the surface of transducer and does not require semi-permeable membrane. In the third generation biosensors, biocatalyst is directly bound to an electronic device for the detection and amplification of the signal [152].

Biosensors can be classified based on the biosensitive element and transduction phenomenon. The biosensor may use different biosensitive elements such as an enzyme, protein, antibody, cell, tissue, receptor, and whole organ to detect specific analytes. According to the transduction phenomenon, they are divided into calorimetric, optical, piezoelectric, and electrochemical biosensors [153].

4.1.1.1 Calorimetric biosensors

Calorimetric biosensors measure the analyte concentration by measuring the amount of heat generated from the enzymatic reactions. Generally, the enzyme was directly immobilized on the thermistor and the generated heat is directly measured using the thermistor. The sensitivity of the calorimetric biosensors was observed to be low as the majority of the generated heat is lost to its surrounding solution before reaching the thermistor. Calorimetric biosensors are difficult to handle and cannot be employed to measure very little heat changes [154].

4.1.1.2 Optical and piezoelectric biosensors

Optical biosensors measure the absorbed or emitted light as a result of biochemical reaction. Optical fibers are used to guide the light waves to suitable detectors. Although these optical biosensors are very sensitive, they cannot be employed in turbid media [155]. In piezoelectric biosensors, the mechanical stress on the crystal generates electric dipoles. The added analyte increased the crystal mass and changes the oscillation frequency and these type of biosensors are used to measure ammonia, carbon monoxide, hydrogen, nitrous oxide, and some organophosphorus compounds [156].

4.1.1.3 Electrochemical biosensors

Electrochemical biosensors are widely used as they possess comparable instrumental sensitivity, can be used in turbid media and are amenable to miniaturization. Biochemical reaction produces or consumes electrons, and this generates an electrochemical signal that can be detected by electrochemical detector. The electrochemical biosensors are further classified into conductometric, potentiometric, and amperometric biosensors [151].

4.1.1.3.1 Conductometric and potentiometric biosensors. The change in the conductance between two metal electrodes in the presence of analyte was measured in conductometric biosensors while potentiometric biosensors measure the working electrode potentials with respect to reference electrode and measure the charge accumulation at zero current generated by the biological binding [152, 157].

4.1.1.3.2 Amperometric biosensors. In amperometric biosensors, the change in the current at the working electrode that is generated from the enzymatic reactions is measured. Biochemical redox reactions produce O_2 and H_2O_2 and these were used for amperometric estimation [158]. Amperometric biosensors generally produce a linear dependence in between the analyte concentration and measured change in the current. These electrochemical biosensors may or may not use electron mediators for electron transfer and the schematic of the electron transfer is depicted in Figure 4.2 [159].

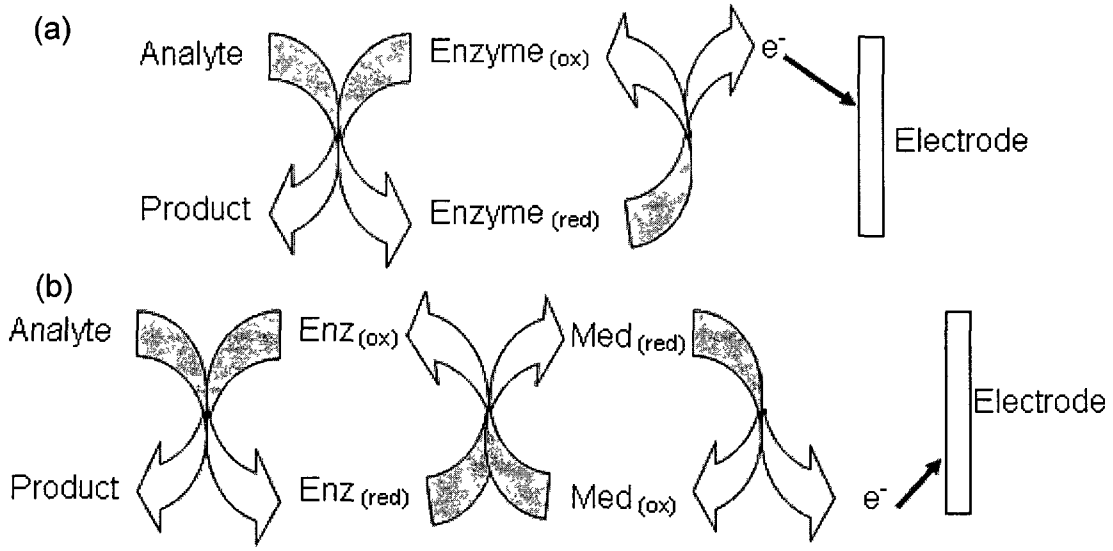

Figure 4.2 Schematic of electron transfer in electrochemical biosensors (a) non-mediated (b) mediated electron transfer [151].

4.2 Glucose Sensor

4.2.1 Literature Review

In the year 2007, an estimated 23.6 million people in the U.S.A. suffered from diabetes mellitus, a group of metabolic disease characterized by defects in insulin production, insulin action, or both [160]. A recent analysis projects that one in three American adults may have diabetes by the year 2050, increasing financial toll to the US economy in the subsequent years [161]. Current commercially available glucose sensors determine glucose levels in blood stream. The linear dependence between blood and saliva glucose levels opened doors to develop non invasive glucose monitoring schemes thus avoiding painful finger sticks assays [162]. Typical human saliva glucose level is between 8 μM and 210 μM [162] and the current available sensors in the market cannot detect such small concentrations.

During the past two decades, various types of glucose sensors have been developed to detect human glucose levels. First generation glucose sensors utilized electrochemical detection to detect glucose. In these types of sensors, glucose oxidase (GOx) was coated onto the electrode and upon the addition of glucose; hydrogen peroxide is released from the enzymatic reactions [163]. The amount of hydrogen peroxide generated is measured by the electrode, which reflects glucose concentrations. However, this method of detection requires higher oxidation potentials and also the glucose analysis at higher concentration is difficult. To overcome these issues, electron mediators were employed in the second generation glucose sensors to shuttle the electrons between enzyme and electrode. Ferrocene and quinine derivatives have been used as common electron mediators for the conventional glucose sensors [164]. Cass et al. showed that 1,1'-dimethyl ferrocene showed good response among all the ferrocene derivatives they have tested [165].

Recently, D. J. Macaya et al. [166] developed a glucose sensor using OECT technology that utilizes PEDOT:PSS source (S) and drain (D) electrodes and platinum (pt) wire as a gate (G) electrode to detect glucose in micromolar range. In their method H_2O_2 generated from the enzymatic reactions was oxidized and later catalyzed by the working platinum electrode. However, the incorporation of Pt electrode complicated the device fabrication and increased the cost.

Although N. Y. Shim et al. [167] developed a glucose sensor based on OECT technology. They have employed tedious clean room processes such as chemical vapor deposition and photolithography techniques to fabricate the devices and also ferrocene (bis (n^5-cyclopentadienyl) iron) (Fc)/ferricenium ion couple was used as an electron mediator to achieve a decent response for micromolar glucose levels [167].

4.2.2 Micromolar Glucose Sensor

The OECT described in Chapter 3 was used to detect the glucose concentrations ranging from 1 μM to 10 mM that include the glucose levels found in human saliva. After fabricating the OECT, glucose oxidase (GOx) and glucose were loaded in to the polymer well successively to undergo electrochemical reactions as depicted in Figure 4.3. GOx catalyzes D-glucose oxidation into D-gluconol, 5-lactone and generates hydrogen peroxide (H_2O_2) according to Eq. 4.1:

$$\beta - D - Glucose + O_2 + H_2O \xrightarrow{GOx} D - gluconicacid + H_2O_2 . \qquad (4.1)$$

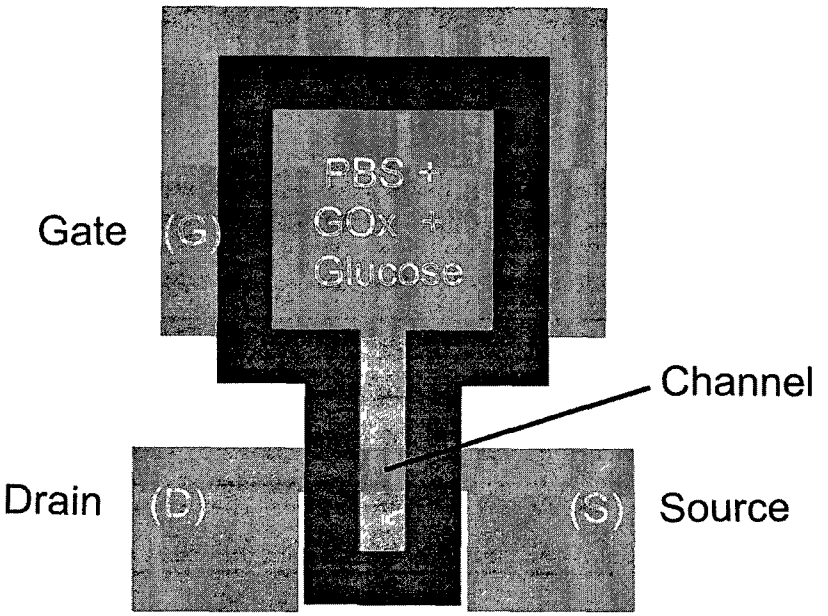

Figure 4.3 Schematic of OECT based glucose sensor (top view).

4.2.2.1 Materials and methods

A 4 mL of PEDOT:PSS (Clevios^{TM} P from H.C. Stark Inc.) was mixed with 1 mL of ethylene glycol (anhydrous 99.8%) and 10 μL of linear alkylbenzenesulfonic acid (97%) to fabricate PEDOT:PSS based OECT. GOx solution was prepared by dissolving 5.0 mg of GOx in 1 ml of 1X phosphate buffer (PB), pH 7.2, and glucose solutions ranging from 1 μM to 10 mM concentrations were prepared in PB for evaluating the sensor. Table 4.1 shows the concentrations and volume of each of the chemicals used in the glucose sensor (same concentrations and volume were used in all the experiments unless otherwise specified).

Table 4.1 Chemicals used in OECT based glucose sensor.

Material	Concentration	Volume	Purpose
PBS , pH 7.0	1X	15 μL	Electrolyte for OECT
PB, pH 7.2	1X	-	Solvent for GOx & glucose
GOx	5 mg/ml	5 μL	Enzyme
Glucose	1 μM-10 mM	5 μL	Analyte

Phosphate buffered saline with calcium chloride and magnesium chloride (PBS) obtained from Sigma-Aldrich was used as an electrolyte for the OECT and 15 μL of it was loaded into the transistor well and was allowed to sit for a minimum of 2 min before adding GOx to allow the electrolyte ions to cross link with the PEDOT:PSS film. For glucose sensing experiments, 5 μL of GOx was loaded into the well followed by adding 5 μL of glucose solution with concentrations from 1 μM to 10 mM. The sensor characteristics were measured using two Keithley 236 Source meters controlled by Interactive Characterization Software (ICS).

4.2.2.2 Glucose sensor working principle

The addition of glucose to the GOx containing well reduces the enzyme and generates H_2O_2. The oxidation of H_2O_2 is catalyzed at the PEDOT:PSS gate electrode further reducing the PEDOT:PSS channel and this reduction is proportional to the glucose concentration as shown by the reaction cycle in Figure 4.4.

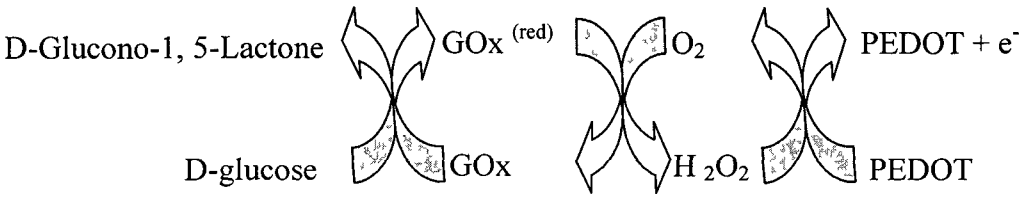

Figure 4.4 Reaction cycle of PEDOT:PSS based glucose sensor.

4.2.2.3 Results and discussion

Figure 4.5 depicts the OECT response for various gate potentials as a function of time at constant drain potential. The polymer well was preloaded with PBS and GOx solutions into which 5 μL of 10 mM glucose was added. V_{ds} was kept at -0.4 V and V_{gs} was increased from 0 V to 0.4 V with a step of 0.1 V and later it was forced to 0 V instantly. In Figure 4.5, x-axis represents time in seconds, left side y-axis represents applied gate potential, and right side y-axis represents the measured drain current. With the application of higher gate voltage, the reduction in the drain current was higher. When the gate potential was decreased from 0.4 V to 0 V instantly, the drain current tried to regain its original value. This indicates that the device is working as a transistor even in the presence of GOx and glucose. The drain current is reaching 90% of its value within 5 s, when there is a shift in the gate potential. So, it is conclusive that the response time of the glucose sensor is 5 s. The reversible reduction in the drain current is due to the application of the higher gate voltage and the magnitude of reduction is associated with the glucose concentration present in the well, i.e. higher the glucose concentration, the more will be the drain current reduction.

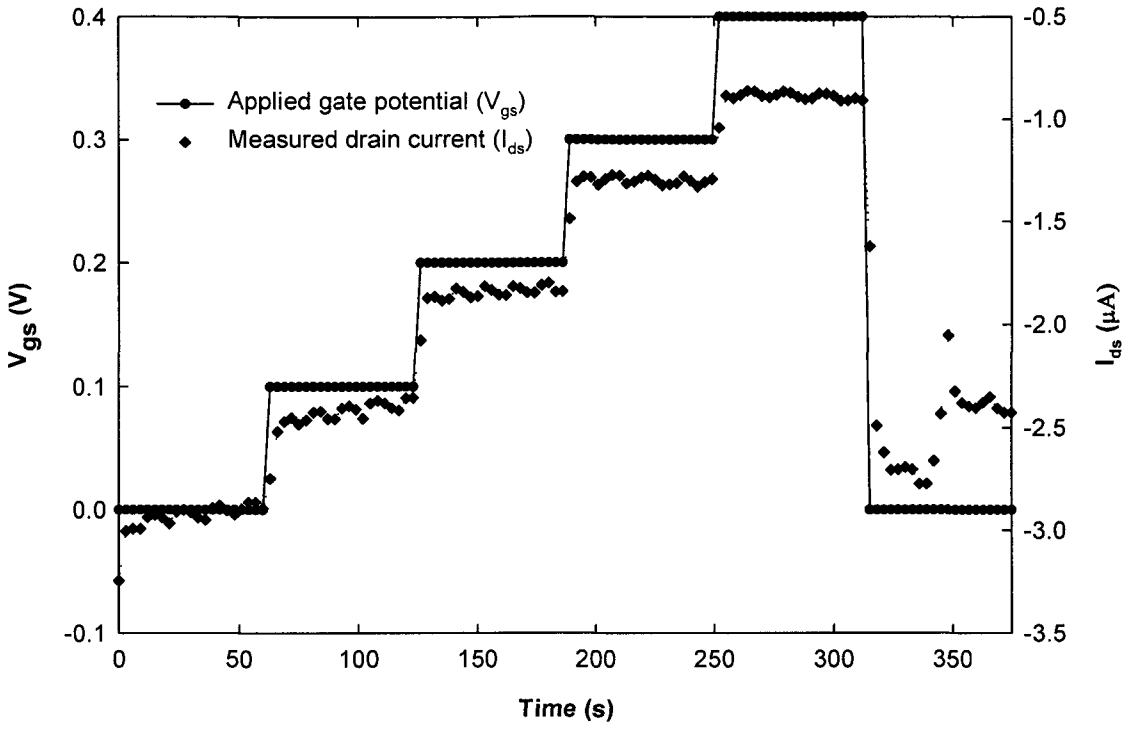

Figure 4.5 Application of gate bias (solid line) resulted in reversible modulation in drain current (I_{ds}) (dotted line).

The relative response of the transistor under various drain voltages in the presence of 0 μM (phosphate buffer), 5 μM, 500 μM, and 5 mM glucose is shown in Figure 4.6. Initially, GOx was loaded into the PBS contained well. Drain current (I_{ds}) was measured by sweeping the drain voltage from 0 V to -1 V with a step of -0.2 V, by keeping the gate voltage at 0.4 V after loading glucose solutions (increasing concentrations) successively to the same well. Initially, 0 μM glucose was added into the GOx contained well followed by adding 5 μM, 500 μM, and 5 mM glucose solutions successively, and the drain current was measured after the addition of each concentration. Upon the addition of higher glucose concentration, the drain current was decreasing as the amount of H_2O_2 generated from the enzymatic reactions is higher in higher glucose concentrations, which further generates a higher number of electrons. The movement of electrons to the PEDOT:PSS

film reduces the channel current, as PEDOT:PSS is a p-type semiconductor [147]. From Figure 4.6, a downward shift in the drain current can be clearly observed as the glucose concentration is increased from 0 μM to 5 mM, and also the amount of shift is higher at higher drain potentials. According to Figure 4.6, the drain current is getting saturated at a drain voltage of -0.4 V and a gate voltage of 0.4 V. Therefore, the drain current was measured at these potentials for glucose sensing experiments.

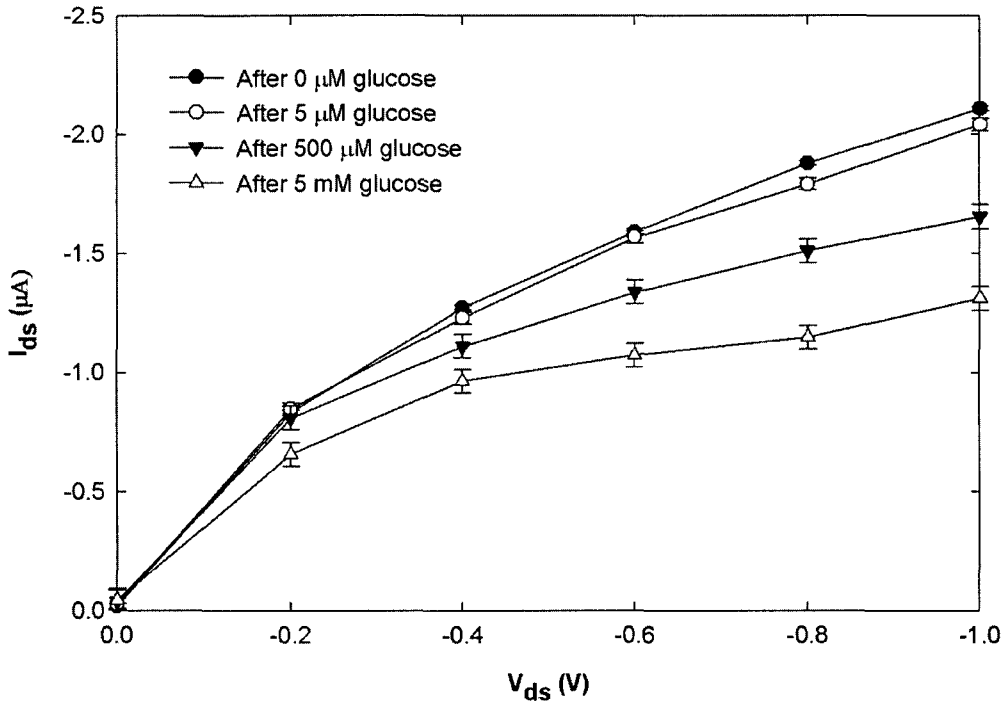

Figure 4.6 Relative response of I_{ds} as a function of V_{ds} under different glucose concentrations.

The drain current was measured in the presence of glutamate in order to test the selectivity of the sensor. Initially, GOx was added to the PBS contained well, followed by adding 1 mM glutamate and 1 mM glucose and measurements were taken after the addition of each solution. The drain current was measured by sweeping the drain voltage from 0 V to -1 V at a gate voltage of 0.4 V. After adding 1 mM glutamate to the GOx

contained well, the drain current was increased and it was decreased after the addition of 1 mM glucose to the same well as depicted in Figure 4.7.

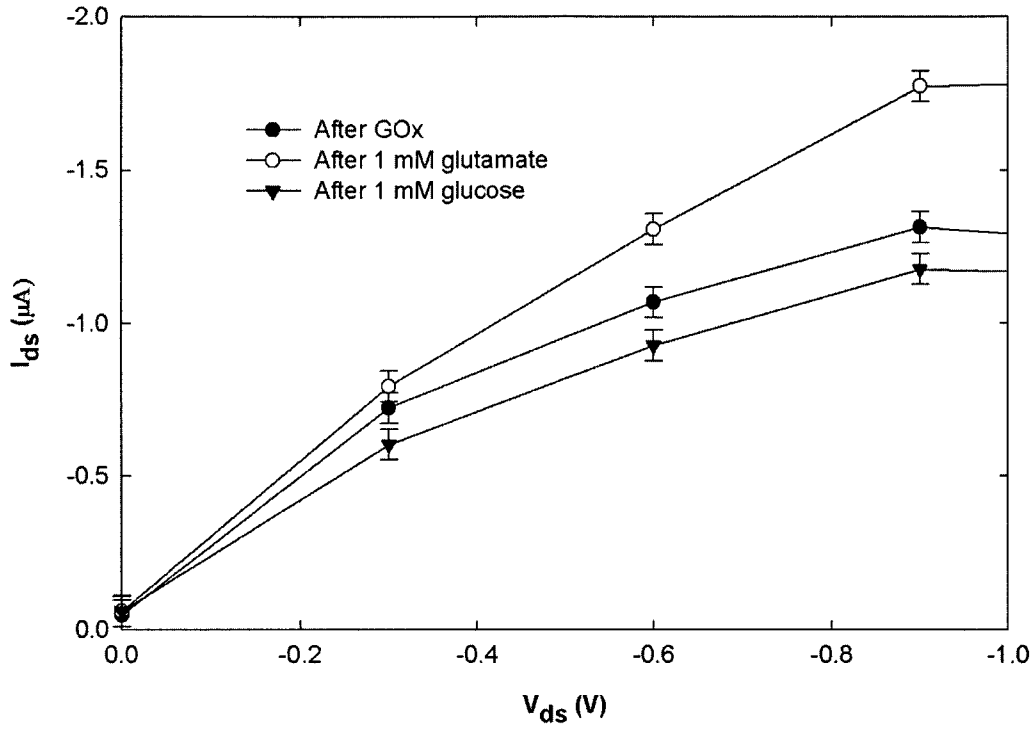

Figure 4.7 Selectivity test to observe the drain current deviation in the presence of glucose and glutamate.

The increase in the drain current with the addition of glutamate can be attributed to the availability of higher electrolyte (PBS + Tris-HCl) solution, as glutamate is dissolved in Tris-HCl buffer solution, while the decrease in the drain current in the presence of glucose is due to the reaction cycle depicted in Figure 4.4. This indicates that the added glutamate is not interfering with the sensor response, as the downward shift in the drain current is only possible, if there is an enzymatic reaction that produces H_2O_2.

Figure 4.8 depicts the sensor normalized response (NR) to various glucose concentrations ranging from 1μM-10 mM at gate and drain potentials of 0.4 V and -0.4 V respectively. A new device has been used for each measurement and in a typical batch

fabrication, the mean drain current (I_{ds}) of 15 devices after loading GOx (before adding glucose to the well) into the wells was found to be -2.12 ± 0.26 μA. So, normalization was done relative to the device base current to facilitate the comparison between different devices in accordance with Eq. 4.2. This normalized response (*NR*) provides a response from zero to one with various glucose concentrations.

$$NR = \frac{(I_0 - I_C)}{I_0}, \tag{4.2}$$

where I_0 is the drain current before adding glucose to the GOx contained well and I_C is the drain current after adding glucose (concentration of interest) to the same well.

Figure 4.8 depicts repeatable sensor response to various glucose concentrations with a coefficient of determination (R^2) of 0.9642. NR starts at 0.112 for 1 μM glucose and increases to 0.414 for 1 mM solution and reaches 0.581 for 10 mM solution. From Figure 4.8 it can be observed that the NR's of 5 mM, 10 mM are close and NR's of 10 mM and 20 mM are almost equal. This illustrates that the sensor response is saturating after 10 mM glucose concentration. The sensitivity of the sensor was found to be 0.01 NR per 1 μM glucose concentration and it showed adequate change in 1-200 μM glucose concentration range, which is relevant for glucose detection in human saliva. The results are in agreement with the reaction cycle shown in Figure 4.4 according to which oxidation of H_2O_2 catalyzed at the PEDOT:PSS gate electrode occurs.

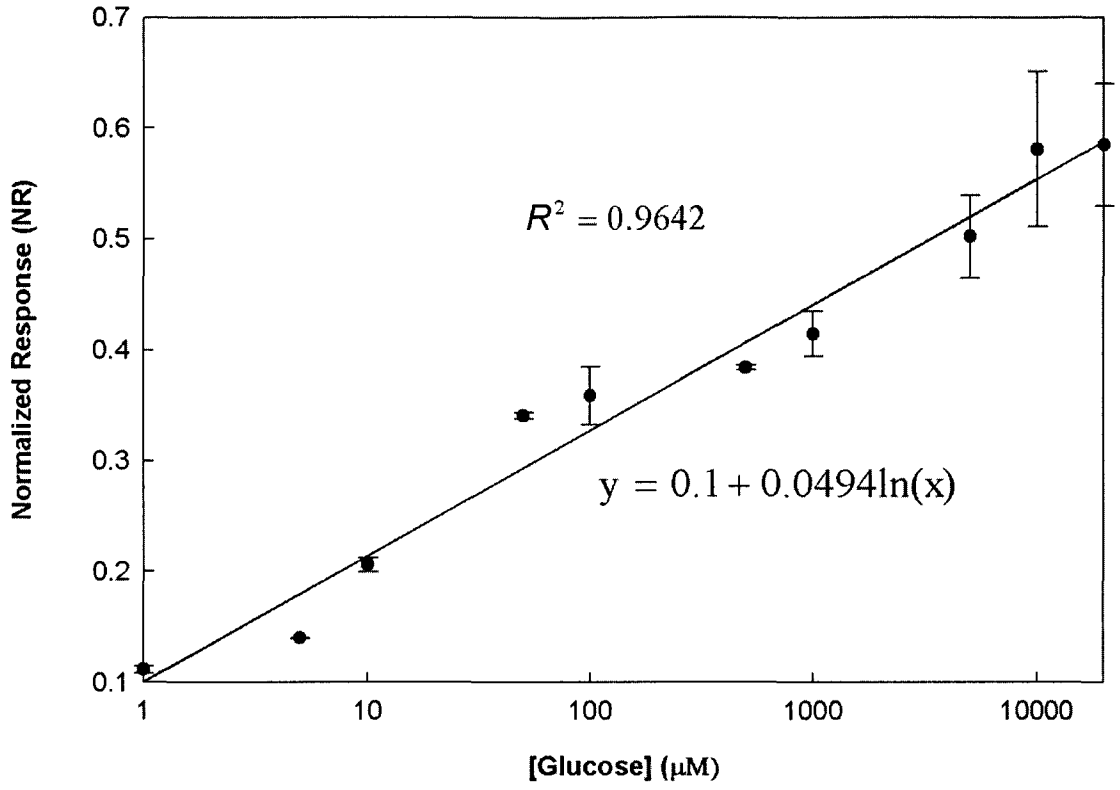

Figure 4.8 Normalized response (NR) of the device for various glucose concentrations. NR is getting saturated after 10 mM glucose concentrations.

4.3 Glutamate Sensor

4.3.1 Literature Review

L-Glutamate is one among 20 standard amino acids and is considered as a source of energy and nitrogen in eukaryotic and mammalian cells [168, 169]. It was recognized as the primary excitatory neurotransmitter in the mammalian central nervous system in the late 1970s, although its excitatory action in the mammalian brain and spinal cord has been known since the 1950s [170-172]. Glutamate works as the primary neurotransmitter for approximately 60% of the neurons in the brain and its reuptake and recycling mechanism is related to up to 2/3 of brain energy metabolism [173, 174]. Neurologists show particular interest to glutamate because of its involvement in neuronal differentiation,

migration, and survival in the developing brain [175]. It also plays a vital role in synaptic plasticity, neuronal development, degeneration, long term potentiation, and long term depression [176, 177].

The defects in cellular reuptake and/or excess production and secretion results in elevated glutamate concentrations. The glutamate concentration in extracellular space is in between 4-350 μM [178]. An overwhelming and uncontrolled extracellular level of glutamate is strongly implicated to retinal dysfunction, neuronal and non-neuronal cells death leading to pathophysiological syndromes and diseases such as multiple sclerosis, Parkinson's disease, Alzheimer's disease, Huntington's disease, cerebral ischemia, epilepsy, and stroke [179-182]. Moreover, L-glutamate is a common food ingredient in Chinese food in the form of L-monosodium glutamate. The excessive intake of the glutamate flavor enhancer results in headache and stomach pain and is linked to Chinese Restaurant Syndrome (CRS) [183, 184]. Hence, glutamate measurement is important for biological and food industries.

Several analytical methods have been developed for glutamate sensing including mass spectroscopy, liquid chromatography, capillary electrophoresis, microdialysis, electrochemiluminescent, and optical methods [185, 186]. However, most of them require time for derivatization and separation. Recently, electrochemical methods have been used widely for glutamate measurement through enzymatic reactions which require smaller sample volume, provide rapid response, show accurate readings, and are easy to handle [169, 185].

Various electrochemical glutamate schemes have been designed over the last decade by L-glutamate oxidase immobilization on electrodes, and entrapment in polymer or carbon paste [178, 187-192]. These different sensors were categorized into first and

second generation glutamate sensors depending on the redox reactions and electron transfer mechanisms at the electrodes. In the first generation glutamate sensors, an enzyme is immobilized on the electrode and the addition of glutamate reduces the glutamate oxidase enzyme and produces α-ketoglutarate and hydrogen peroxide (H_2O_2). At certain potentials, the electrode gains the electron from H_2O_2 and converts it into H_2O and O_2 [193]. The second generation glutamate sensors use a secondary redox enzyme and the reduction/oxidation reaction of this redox mediator detects the analyte [194].

First generation glutamate sensors are simple in structure and faster in glutamate detection. However, they require high glutamate oxidase concentrations ranging from 100-200 U/ml and a high potential is needed for the redox reactions to occur, whereas the second generation glutamate sensors can be operated at lower potentials and use lower concentration of enzyme (~ 1 U/ml). They suffer from difficulty in reproducing the fabrication process and in less precise detection of glutamate [195].

Recently, several glutamate sensors have been developed based on different techniques such as smart-biochips, floating gate transistors, flow injection analysis, electrochemical sensor array and carbon fiber electrode. However, most of these sensors need tedious clean room processing techniques for the fabrication, require high enzyme concentrations, enzyme immobilization techniques, and importantly, pH of the solutions affect the sensor performance [190, 196-201]. Therefore, there is a need for developing a simple, efficient, and low cost glutamate sensor that requires small sample volumes, uses lower glutamate oxidase concentrations, can be operated at lower potentials, and is stable for a wide pH range.

4.3.2 Micromolar Glutamate Sensor

The glutamate sensor depicted in Figure 4.9 was developed using the fabricated OECT to detect glutamate concentrations ranging from 1 μM to 100 μM. The sensor showed a linear response from 1 μM to 100 μM glutamate with a R^2 of 0.9817 and a sensitivity of 0.003 NR/μM. Astrocytes and glioma cells were treated with stimulating agents such as Adenosine-5'-triphosphate (ATP), potassium chloride (KCl), and cystine. Glutamate released from these stimulations was measured with the biosensor under consideration and the results were compared to a fluorescent assay for glutamate. The sensor response followed the fluorescent assay response and demonstrated differential glutamate release from astrocytes and glioma cells in culture.

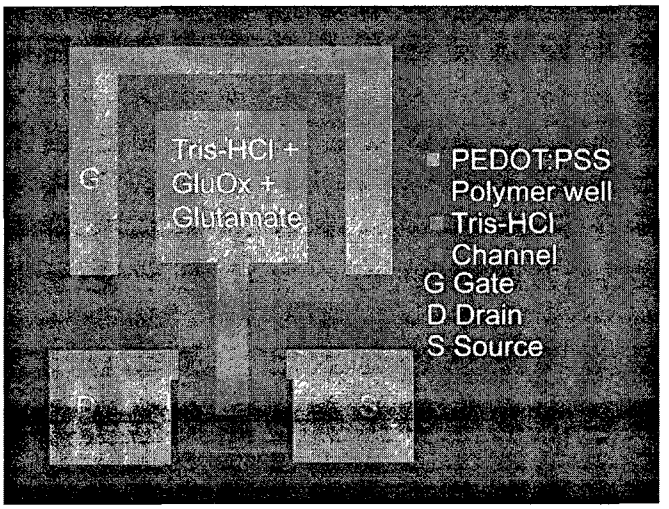

Figure 4.9 OECT based glutamate sensor (top view).

4.3.2.1 Materials and methods

4.3.2.1.1 Reagent preparation. PEDOT:PSS polymer solution was prepared to fabricate OECT. L-glutamate oxidase (GluOx) solution was prepared by dissolving 0.5 units of GluOx in 1 ml of 1X tris(hydroxymethyl)aminomethane-HCl (tris-HCl) buffer (pH 7.5)

and was used as an enzymatic solution for all the glutamate sensing experiments. A stock solution of 0.5 U/mL GluOx was prepared in 1X Tris-HCl buffer (pH 7.5) and was used as an enzymatic solution for all the experiments presented here. Glutamate concentrations ranging from 1-100 μM were prepared in the same buffer solution for sensor evaluation.

4.3.2.1.2 Cell culture. Astrocytes were obtained from a newborn rat's brain and were cultured in 25 cm^2 flasks at 90% humidity and 5% CO_2 according to G. Wang et al. [202]. Astrocytes were maintained in Ham's F-12K containing horse serum, 5% fetal bovine serum, and 5% penicillin and streptomycin. The brain tumor cell line CRL 2303 was purchased from ATCC (Manassas, VA) and was maintained according to vendor specifications in Dulbecco's Modified Eagle's medium containing 5% fetal bovine serum and 5% penicillin and streptomycin and 0.5 ml of cell cultures were plated in 24 wells culture plate and incubated for 24 hours. For both astrocytes and brain tumor cells, the cells were plated at a density of 30,000 cells/ml, and after the 24 hours of culture, the plates were washed with 0.5 ml of Locke's solution before the cells were treated with stimulating chemicals (100 μM ATP, 50 μM KCl, or 200 μM cystine). The samples were collected from the cell media after 5 min of treatment.

Table 4.2 shows the concentrations and volume of each of the chemicals used in glutamate sensor experiments (same concentrations and volume were used in all the experiments unless otherwise specified).

Table 4.2 Chemicals used in OECT based glutamate sensor.

Material	Concentration	Volume	Purpose
Tris-HCl, pH 7.5	1 X	15 μL	Electrolyte for OECT and solvent for GluOx and glutamate
GluOx	5 mg/ml	5 μL	Enzyme
Glutamate	1 μM-100 μM	5 μL	Analyte
ATP	100 μM	-	Stimulating agent
KCl	50 μM	-	Stimulating agent
Cystine	200 μM	-	Stimulating agent
Astrocytes	30,000 cells/ml (before incubation)	-	To measure glutamate release
Glioma Cells	30,000 cells/ml (before incubation)	-	To measure glutamate release

4.3.2.1.3 Methods. Initially, the sensor was evaluated using various glutamate concentrations. Later, it was used to measure the glutamate released from astrocytes and glioma cells after treating with stimulating agents. For glutamate sensing experiments, the OECT well was preloaded with 5 μL GluOx solution, followed by adding 5 μL of L-Glutamic acid solution (concentration of interest).

According to previous reports, astrocytes and glioma cells release glutamic acid with cystine stimulation [203, 204]. The glutamate that is released from stimulations reported here was measured using both a spectrofluorometer assay and the developed glutamate sensor. For fluorometric measurements, 50 μL of the sample was collected from the corresponding plate (after stimulation), and it was warmed up with 50 μL of

fluorometric working solution for 30 min according to the methods specified by the Invitrogen Amplex Red Glutamic Acid/Glutamate Oxidase Assay kit. The fluorescence was measured with a BioTek FLx800 fluorescence microplate reader with excitation and emission wavelengths of 540 nm and 600 nm, respectively. For OECT based glutamate sensor measurements, 5μL of the sample was collected from the plate (after stimulation) and was added to the GluOx contained well and the electrical characteristics of the sensor were measured using two Keithley 236 Source meters controlled by (ICS).

4.3.2.2 Glutamate sensor working mechanism

With the addition of L-Glutamic acid to GluOx containing well, GluOx catalyzes the oxidation of L-glutamate in the presence of oxygen and produces α-ketoglutarate, NH_4^+ and H_2O_2 [205]. The potential applied to PEDOT:PSS gate electrode catalyzes the H_2O_2 oxidation and produces H_2O, O_2 and electrons according to Eqs. 4.3 and 4.4: These oxidation current (generated electrons) is directly proportional to the glutamate concentration in the solution. The transistor channel gains the electrons from these enzymatic reactions, and the overall conductivity of the channel is decreased as the channel is made up of p-type conductive polymer. The higher the glutamate concentration, the more the number of electrons generated and the higher is the decrease in the channel current.

$$\text{L} - \text{glutamate} + \text{O}_2 \xrightarrow{\text{GluOx}} \alpha - \text{ketogluatarate} + \text{H}_2\text{O}_2 + \text{NH}_4^+ \tag{4.3}$$

$$\text{H}_2\text{O}_2 \xrightarrow{\text{PEDOT}} 1/2\,\text{O}_2 + \text{H}_2\text{O} + 2\text{e}^- \tag{4.4}$$

4.3.2.3 Results and discussion

The transistor response was measured by pulsing V_{gs} in between 0 V to 0.4 V with a step of 0.1 V at a drain voltage of -0.4 V after adding 5 μL of 100 μM L-glutamate to the GluOx contained OECT well. In Figure 4.10, the x-axis represents the time in

seconds, left side y-axis represents the applied gate voltage, and right side y-axis represents the measured drain current, the solid line depicts the applied gate voltage, and the dotted line reflects the measured drain current (I_{ds}). Figure 4.10 depicts the transistor response with the application of four continuous cycles. The first half of the cycle involves increasing the gate voltage from 0 V to higher voltage (0.1 V, 0.2 V, 0.3 V, 0.4 V), and the second half of the cycle involves reducing the gate potential from higher value to 0 V. The drain current is decreasing in the first half of all four cycles due to the migration of H^+ ions from the electrolyte, which dedope the PEDOT:PSS channel and the charge transfer reactions at the gate electrode determines the exact amount of dedoping [206]. The drain current is gaining its initial value only in the second half of the first cycle due to the complete migration of diffused H^+ ions from the PEDOT:PSS channel to electrolyte, while the drain current is gaining a small threshold value, instead of reaching its initial value in second half of the remaining cycles due to the partial migration of diffused H^+ ions from the PEDOT:PSS channel to electrolyte. From Figure 4.10, it is evident that the application of a positive gate voltage is causing a reversible decrease in the channel current (I_{ds}). The magnitude of which depends on the glutamate concentration present in the well, i.e. the higher the glutamate concentration, the higher is the decrease in the drain current.

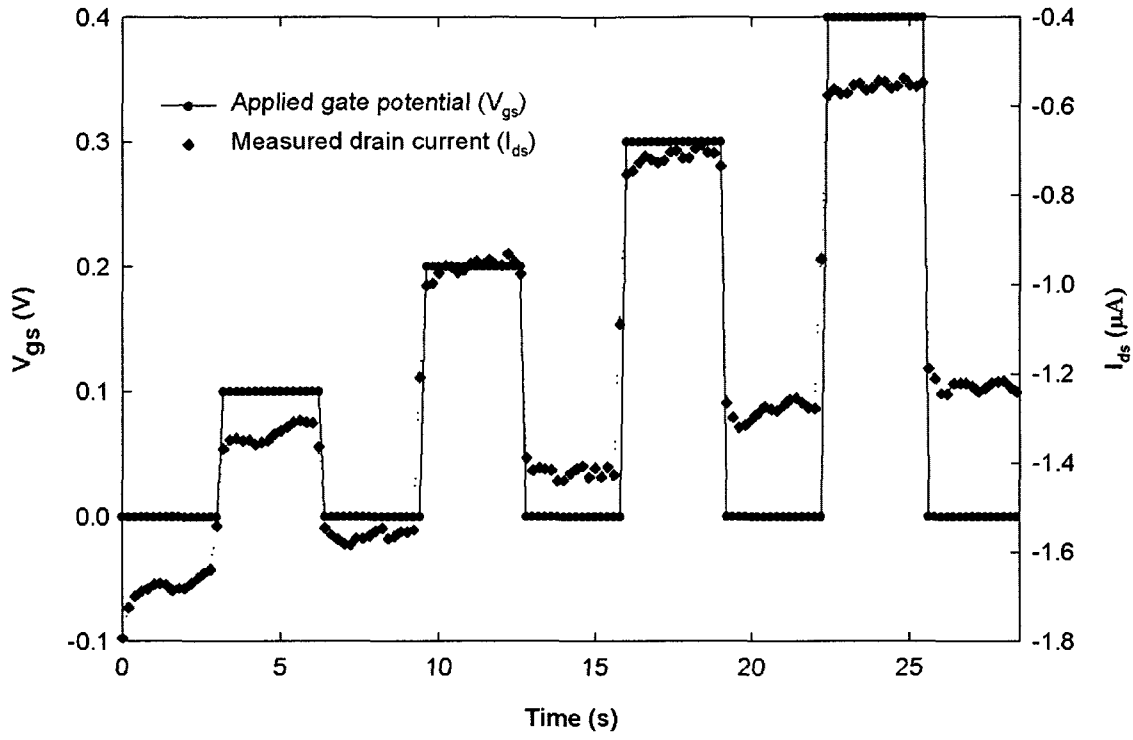

Figure 4.10 Applied gate bias (solid line) causes reversible modulation in drain current (dotted line).

4.3.2.3.1 Control tests. The transistor response in the absence of enzyme indicated that the drain current does not decrease in the absence of the enzyme. The transfer characteristics of the device were depicted in Figure 4.11. The drain current was measured by sweeping the gate potential from 0.2 to 0.8 V with a step of 0.2 V by keeping the drain voltage at -0.4 V. Tris-HCl buffer solution, 100 μM glutamate and GluOx were added successively to the same well and the drain current was measured after each measurement. There is no considerable downward shift in the drain current curve with the addition of glutamate to the polymer well containing tris-HCl and there is a considerable downward shift in the drain current curve with the addition of GluOx to the well as shown in Figure 4.11. From the following Figure 4.11, it is evident that the decrease in the drain

current is only possible in the presence of both GluOx and glutamate, i.e. the drain current is reducing only due to the enzymatic reactions described in Section 4.3.2.2.

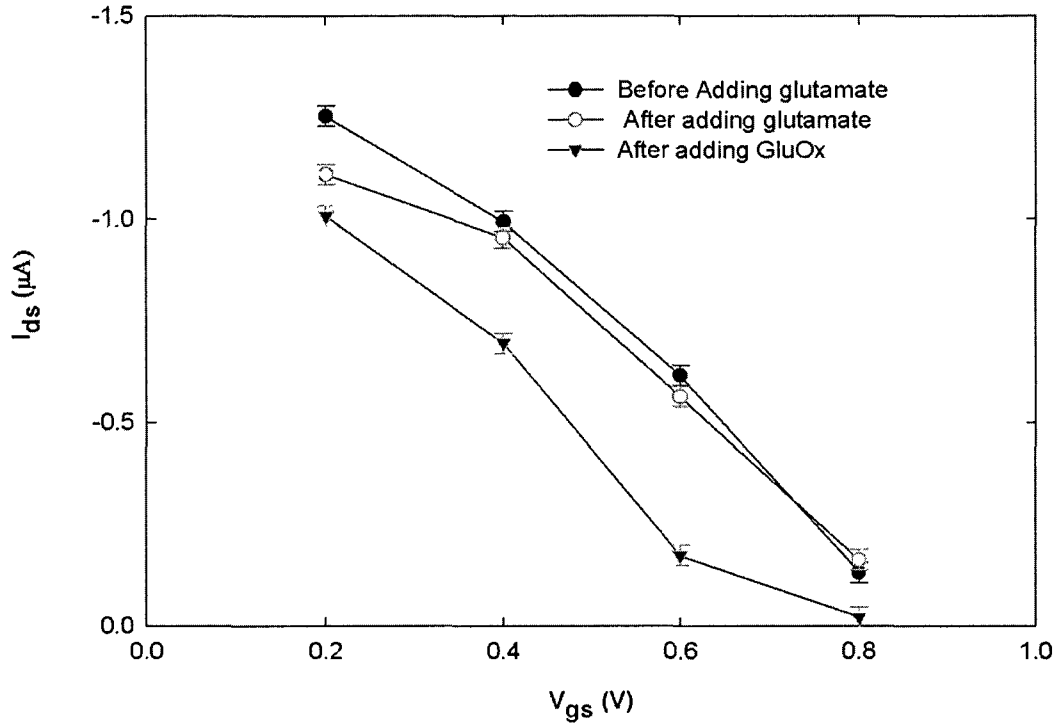

Figure 4.11 The shift in the drain current curve with the addition of GluOx to the glutamate containing well at various gate potentials.

In another set of experiments, the drain current was measured as a function of time by keeping drain potential at -0.4 V and gate potential at 0.4 V. The device response was measured by adding tris-HCl, 100 μM glutamate and GluOx successively at certain intervals successively to the same well. Tris-HCl was added at 0 s, 100 μM glutamate was added at 30 s that contained tris-HCl buffer solution, and GluOx at 80 s. From Figure 4.12, it can be observed that there is little or no change in the drain current with the addition of glutamate to tris-HCl containing well and the addition of GluOx resulted in a significant reduction in the drain current, and this can be attributed to enzymatic reactions,

i.e. the drain current decreases (at constant gate and drain potentials) only in the occurrence of enzymatic reactions.

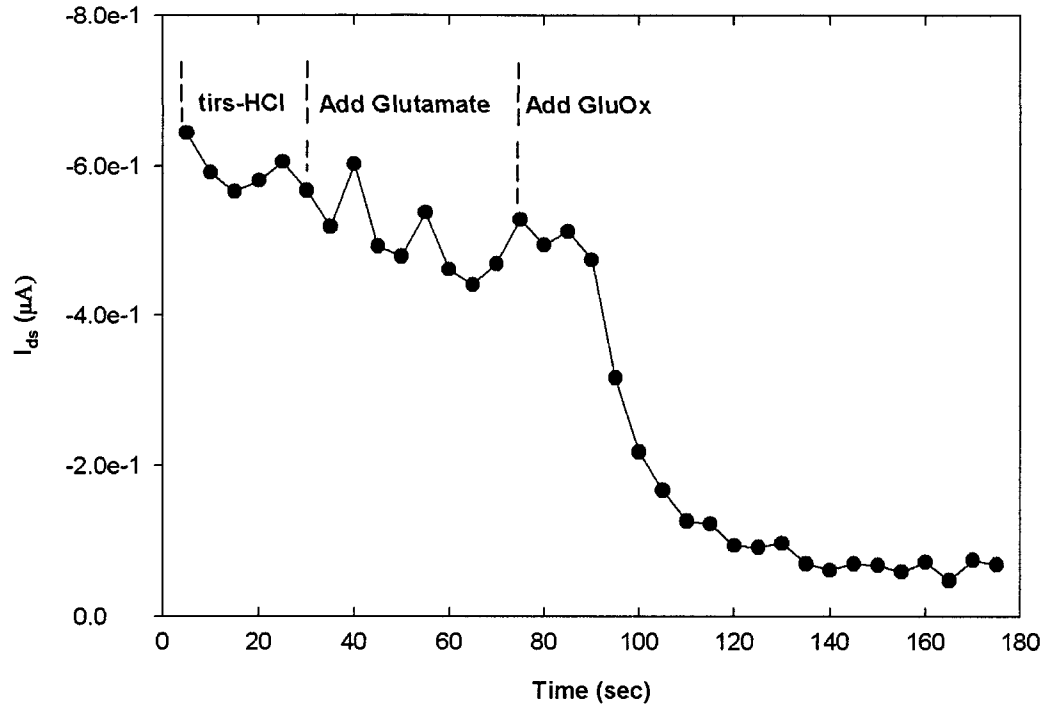

Figure 4.12 The deviation in the drain current with the successive addition of glutamate and GluOx as function of time.

The output characteristics of the OECT for various glutamate concentrations were measured at a gate potential of 0.4 V by varying drain potential from 0 V to -1 V with a step of -0.2 V. The drain current was measured before loading GluOx to the well, after loading GluOx to the well, and after loading 0 μM (tris-HCl buffer), 10 μM, 50 μM, and 100 μM glutamate concentrations successively to the same well. Figure 4.13 illustrates the shift in the drain current curve with the addition of different glutamate concentrations to the polymer well. The addition of GluOx to the polymer well did not affect the drain current, while with the addition of 0 μM glutamate (buffer) there is a minute deviation in the drain current. With the addition of 10 μM glutamate solution, the reduction in drain

current is clearly evident from the Figure 4.13 and the drain current curve has been shifting downwards with the addition of higher glutamate concentrations. This is due to the generation of H_2O_2 from enzymatic reactions, which is higher in higher glutamate concentrations. According to Figure 4.13, the drain current is getting saturated at a drain voltage of -0.4 V and a gate voltage of 0.4 V. So, the drain current was measured at these potentials for glutamate sensing experiments.

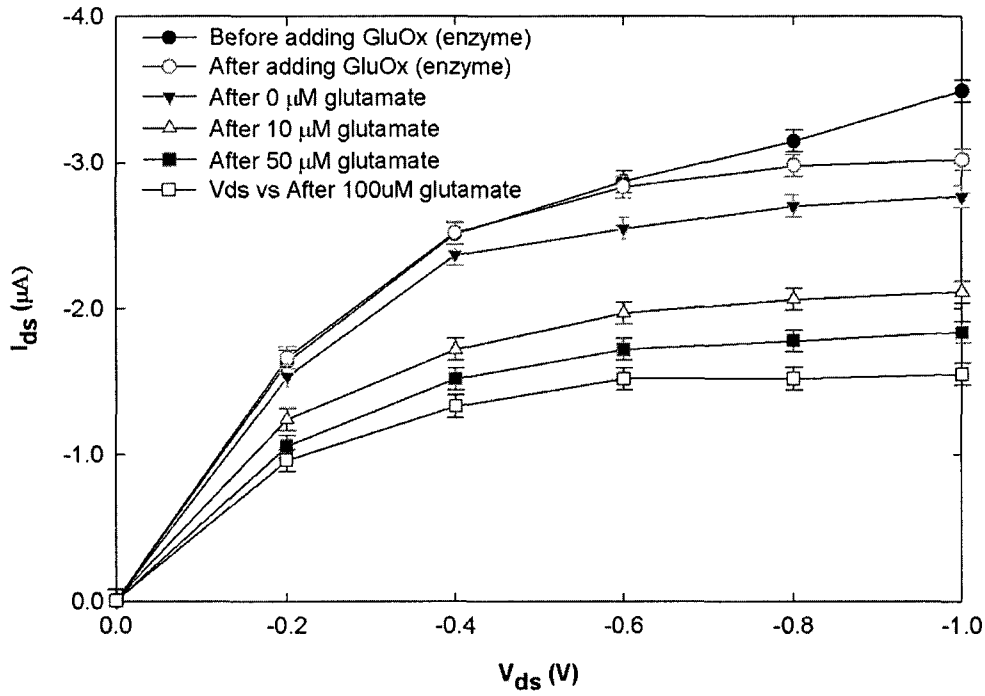

Figure 4.13 Downward shift in the drain curve with the successive addition of higher glutamate concentrations to the same device as a function of drain voltage.

4.3.2.3.2 Glutamate sensing. L-glutamic acid (concentration of interest) was added to the GluOx contained well and a new device was used for each new measurement to evaluate the sensor response for various glutamate concentrations. The drain current was measured before adding glutamate to the GluOx contained well and was measured again after adding glutamate to the same well. Normalization of the drain current was done

according to Eq. 4.5 to minimize the effects associated with the device base currents thus facilitating comparison between different devices.

$$NR = \frac{(I_B - I_A)}{I_B}, \tag{4.5}$$

where NR is the normalized response of the drain current, I_B is the drain current before adding glutamate to the GluOx contained well, and I_A is the drain current after adding glutamate (concentration of interest) to the same well.

Figure 4.14 depicts the plot of normalized response (NR) as a function of L-Glutamic acid concentration. NR starts at 0.0587 for 1 μM glutamate, increases to 0.2018 for 50 μM glutamate, reaches 0.3643 for 100 μM glutamate concentration and the linear response yielded a coefficient of determination (R^2) of 0.98 and a sensitivity of 0.003 NR/μM. The results are consistent with the reaction cycle as shown in Eqs. 4.3 and 4.4, according to which the H_2O_2 oxidation is catalyzed by the PEDOT:PSS gate electrode.

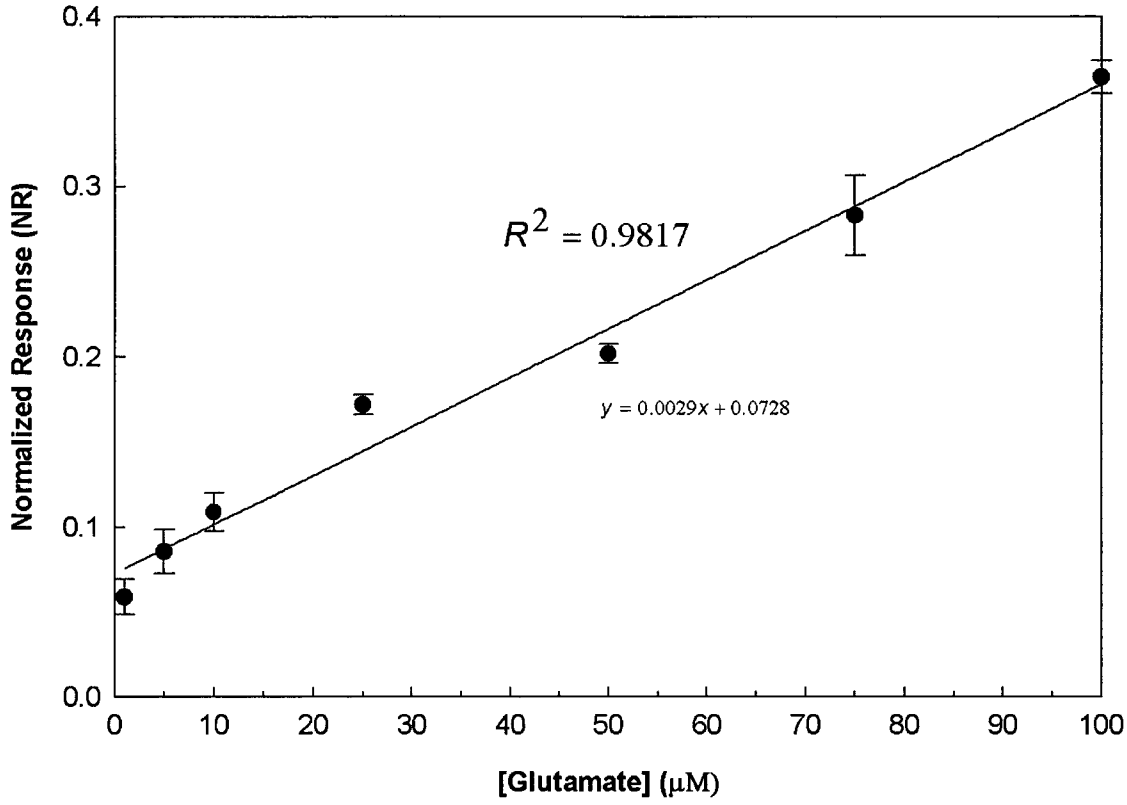

Figure 4.14 Normalized response of the sensor as function of glutamate concentration.

4.3.2.3.3 Glutamate release from brain cell stimulation. Glutamate release from glioma cells and astrocytes were measured using the sensor under consideration and the results were compared with fluorescent spectrophotometer response as explained in Section 4.3.2.1.3. Samples were collected after 5 min of the stimulation treatment to measure the glutamate released from both glioma cells and astrocytes.

Control experiments were done on different devices to measure the response of the sensor with the addition of KCl, ATP and cystine into the GluOx contained transistor well. Drain current was measured by keeping gate potential at 0.4 V and sweeping the drain potential from 0 V to -1.4 V with a step of -0.2 V before adding the solutions and measured again after the addition of solutions to the same well. From Figure 4.15 (a), (b)

and (c) it is evident that the sensor is not showing or showing little response in the presence of ATP, KCl and cystine, respectively, i.e., the stimulating agents are not affecting the sensor response significantly. Therefore, if the sensor shows any response after stimulation, that should be only due to the enzymatic reactions between released glutamate and GluOx that was present in the well.

(a)

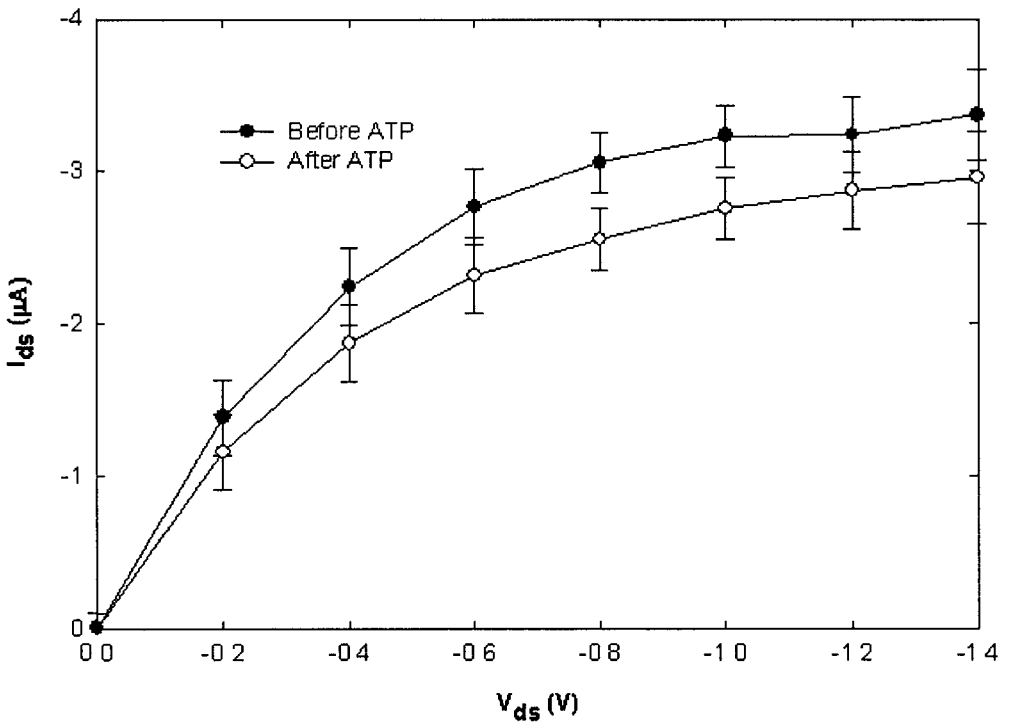

(b)

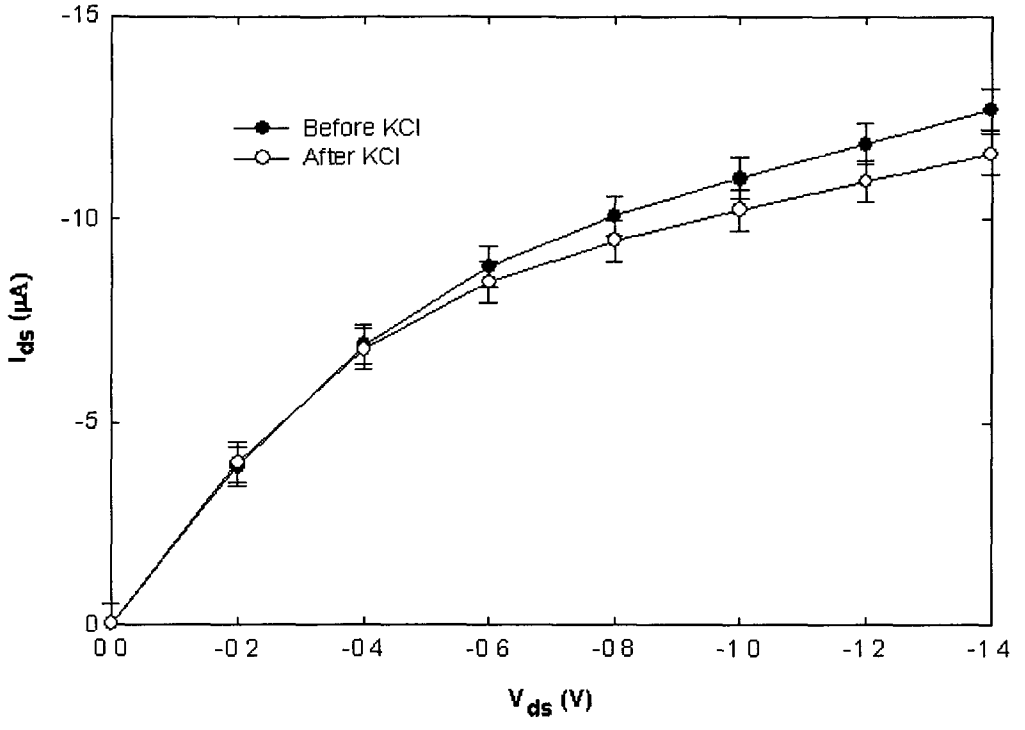

(c)

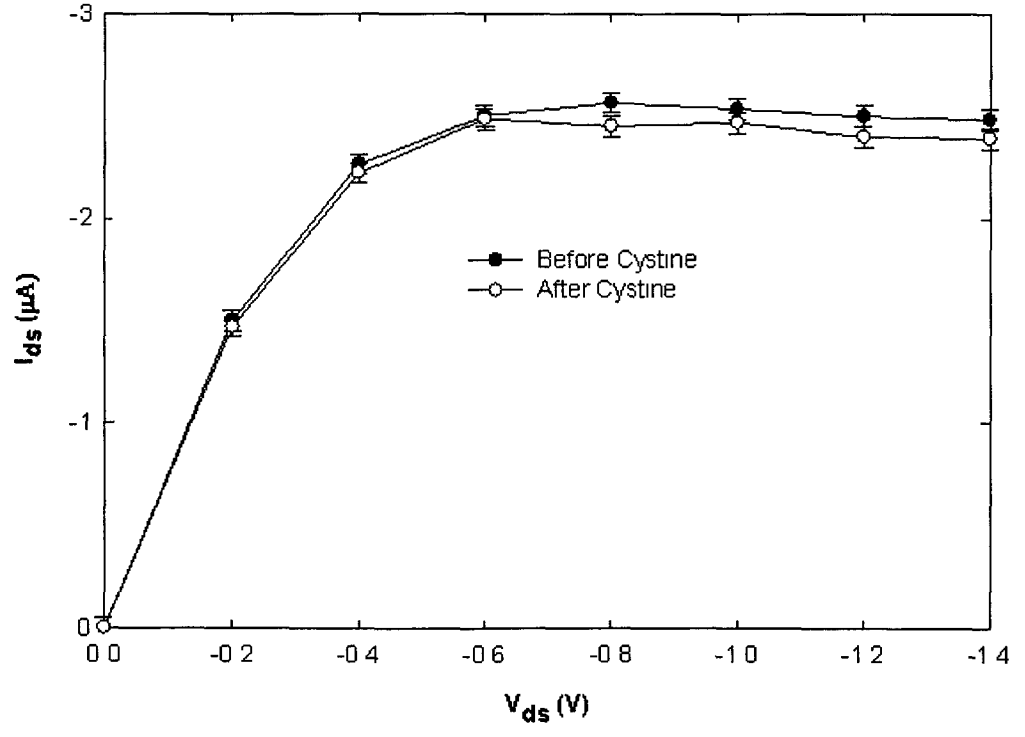

Figure 4.15 Effect of stimulating agents on drain current. Minimal downward shift in the drain current in the presence of (a) ATP, (b) KCl and (c) cystine.

Figure 4.16 depicts the normalized response (NR) of the device under the influence of 100 μM glutamate, ATP, KCl, and cystine. The average responses shown for ATP, KCl, and cystine are all at least 5-fold less than the response to 100 μM glutamate.

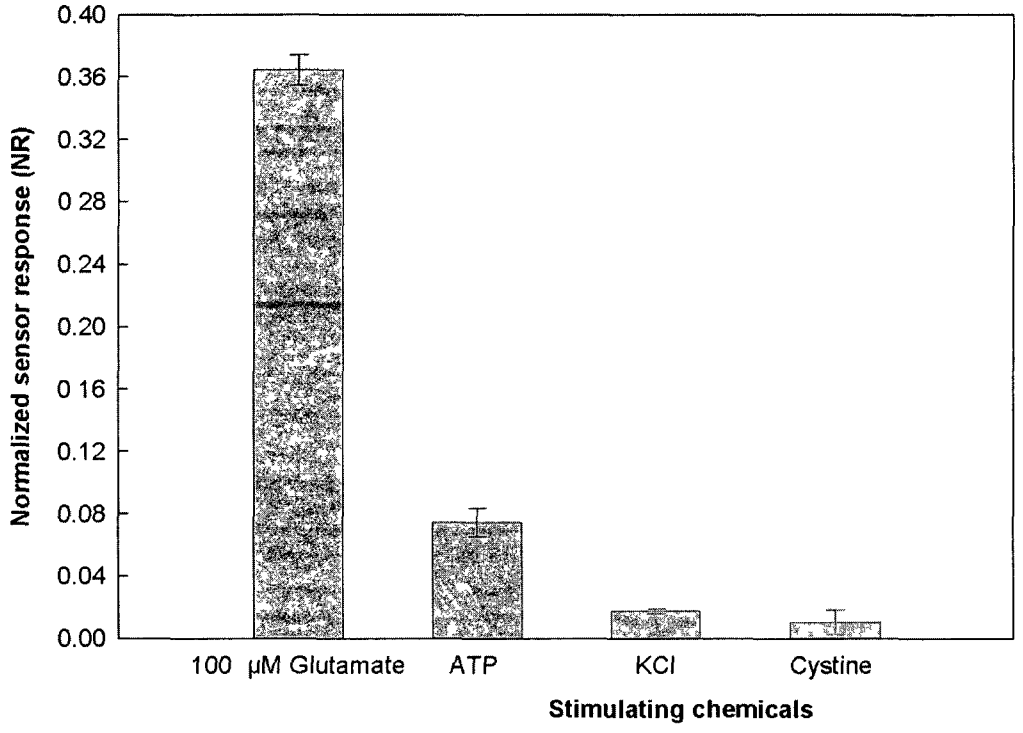

Figure 4.16 The minimal OECT response for stimulating chemicals (negative controls).

Figures 4.17 and 4.18 depict the OECT response and fluorescent spectrophotometer response of the collected samples after treating glioma cells and astrocytes with stimulating agents, respectively. Control tests were done to measure the glutamate from the cells without stimulation. The left side axis represents the normalized response of the glutamate sensor under consideration and the right side axis represents the response measured from the fluorescent glutamate assay. It is evident that the OECT glutamate sensor response trend is following that of fluorescent spectrophotometer response for various stimulating agents.

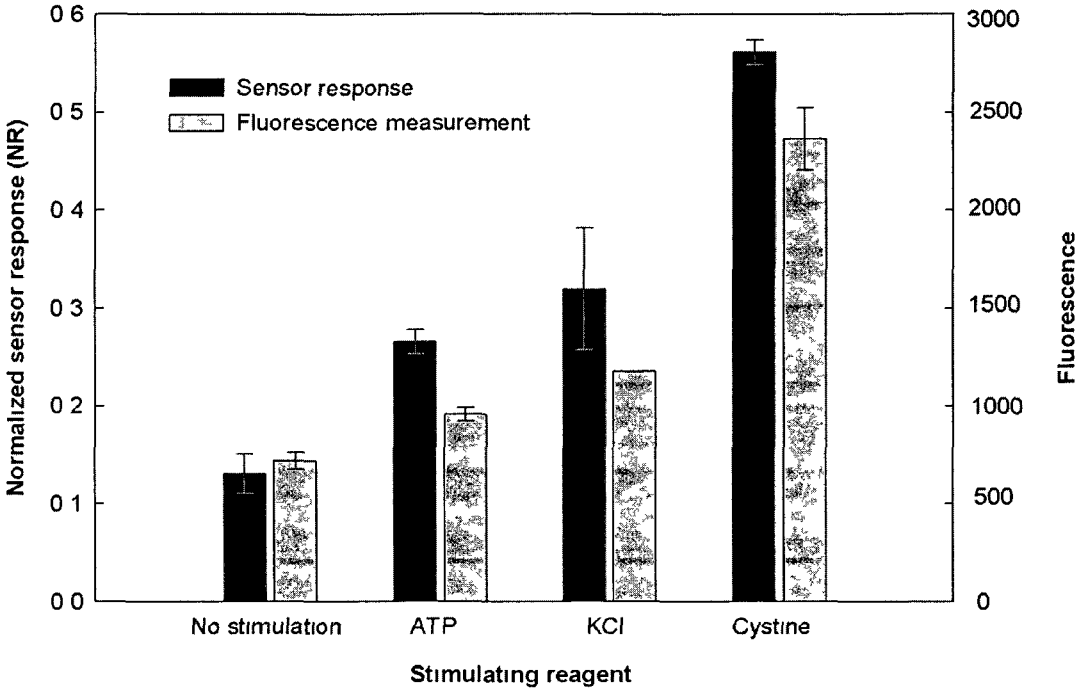

Figure 4.17 Detected glutamate release from brain tumor glioma cells.

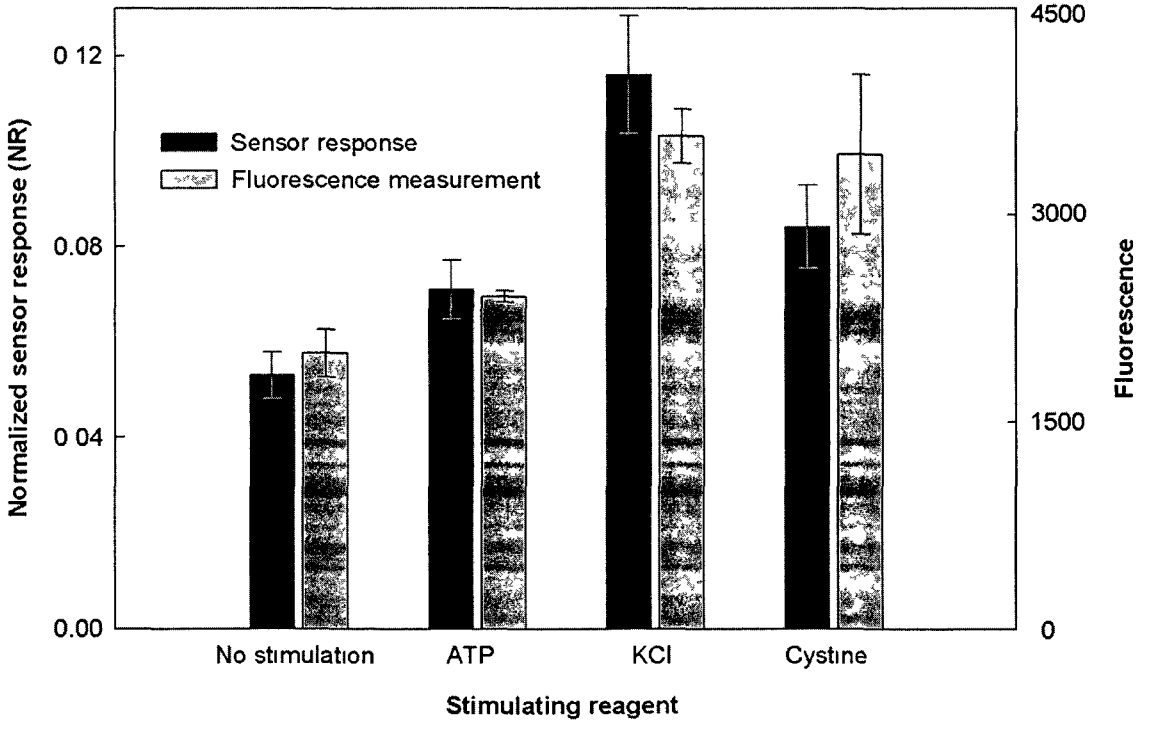

Figure 4.18 Detected glutamate release from astrocytes.

The OECT sensor showed a normalized response of 0.13 without stimulation as shown in Figure 4.17, which implies that the glioma cells themselves have some glutamate available before stimulation. The sensor showed NR's of 0.26, 0.32, and 0.56 for ATP, KCl, and cystine stimulations respectively which can be attributed to the availability of higher glutamate concentrations in the collected samples. Cystine releases the glutamate from glioma cells through a X^-_c exchanger system and KCl releases glutamate through reverse operation of glutamate transporters and swelling/anion channels [207].

A NR of 0.05 was observed for no stimulation depicted in Figure 4.18, indicating that the astrocytes release low levels of glutamate before stimulation compared to glioma cells (Figure 4.17). Normalized responses of 0.07, 0.11, and 0.08 were observed for ATP, KCl, and cystine stimulations. The high glutamate concentration for KCl stimulation is due to the reverse operation of glutamate transporters and depolarization, and astrocytes poorly express cystine system which resulted in low response for cystine stimulation compared to glioma cells [208].

Figures 4.17 and 4.18 show that the OECT biosensor is more sensitive than the fluorescent spectrophotometer assay in measuring glutamate release from brain cells after stimulation and also that the proposed biosensor requires only 5 μL of the sample, while the spectrophotometer requires 50 μL of the sample in addition to fluorescent and other chemicals. The NRs of astrocytes were much lower than the glioma cells, most likely due to fact that astrocytes reuptake the glutamate that is being released from stimulation after a certain time, while the poor reuptake by glioma cells is due to lack of some essential glutamate transporters such as EAAT and GLAST, and their X^-_C system is not sufficient to reuptake the glutamate [203, 204]. In fact, glutamate has been suggested as an

autocrine factor for glioma cells, released into their surroundings in brain tumors as a possible mechanism for enhancing cell growth [200, 204].

CHAPTER 5

CONCLUSIONS AND FUTURE WORK

5.1 Conclusions

Several designs of passive micromixers were simulated using MemCFD module of CoventorWare software. The visual inspection of the fluid flow along the microchannels and the obtained fluid velocities along the channel demonstrated that the designs with rectangular baffles and omega channels will provide good mixing. Several designs of passive micromixers were fabricated on Si using photolithography and ICP etching (to get vertical side walls) in class 100 clean room. The fabricated mixers were tested by injecting red and blue colored food dyes through the channels using a syringe pump. Fluid flow images and videos were collected from the digital camera attached to the microscope. The mixing efficacy was quantified by measuring the standard deviation of RGB values of pixel at inlet and outlet sections. A mixing efficacy of 65.09% was observed in "omega channel with intermediate stage" micromixer design.

A flexible polymer passive micromixer was fabricated on polyester sheet using a simple, inexpensive and rapid xurography technique. The whole transistor was fabricated in less than 15 min and comprises a total thickness of 0.6 mm without the inlet and outlet ports. The flexible micromixer was tested by injecting two food coloring dyes and also by injecting NaOH and Phenolphthalein using a syringe pump. The mixing efficiency was characterized by measuring the absorbance of the color product formed at two outlets.

The mixing efficacy of the micromixer at various *Re* ranging from 0.1-100 was measured by varying the flow rates, and mixing efficiencies greater than 90% were observed for *Re* 0.1, 1, 10, 20, and 30. The biocompatibility of the device was characterized by testing the GOx enzyme activity, which was injected through the microchannels at various flow rates. The GOx enzyme retained its activity for all the measured flow rates.

A complete polymer based transistor was fabricated on both glass and flexible substrates. Xurography technique was used to cut the masks and wells for the transistor. A conducting polymer, PEDOT:PSS was spin coated on the glass to get patterned PEDOT:PSS strips. A stack of three wells was attached onto the patterned PEDOT:PSS strips. PBS and Tris-HCl were used as electrolyte materials. The PEDOT:PSS strips along with the electrolyte solutions constitutes organic electrochemical transistor (OECT). The transistor characteristics are similar to those of p-type MOSFET, as PEDOT:PSS is a p-type semiconductor. The device characteristics demonstrated that the device is losing its current by half in the first two days and no significant reduction is observed for the next 20 days. The device showed a stable response for a wide pH ranging from pH 4 to pH 9.

The fabricated OECT was used to develop glucose and glutamate sensors. The developed glucose sensor is able to detect glucose levels ranging from 1 μM-10 mM and showed a decent response for the glucose levels similar to those found in human saliva. The developed glutamate sensor is able to detect glutamate concentrations ranging from 1 μM-100 μM. The glutamate released from astrocytes and glioma cells after stimulating with ATP, KCl, and cystine was measured using the developed sensor and the results were compared with standard fluorescence spectrophotometer results.

5.2 Future Work

For the simulated micromixer designs, those that showed good mixing performance will be fabricated on PDMS using the soft lithography technique. The developed flexible polymer micromixer will be used to mix antibody and antibody-analyte conjugate for future immunosensor applications. Later, the flexible micromixer could be integrated with the developed biosensor to develop an immunosensor that can detect lower molecular weight molecules.

In an effort to develop an immunosensor to detect lower molecular weight molecules, the cofactor flavin adenine dinucleotide (FAD) was separated from GOx leaving Apo-GOx (This was done by Dr. Blake group at Tulane University and was brought to Louisiana Tech University to make the proposed immunosensor). The reactivation of apo-Gox by adding different concentrations of FAD was done using Thermo Scientific Nanodrop spectrophotometer. Figure 5.1 depicts the reactivation of apo-GOx with various FAD concentrations and a native GOx with full activity. Future experiments could include reactivating the apo-GOx using the developed organic electrochemical transistor to develop the immunosensor.

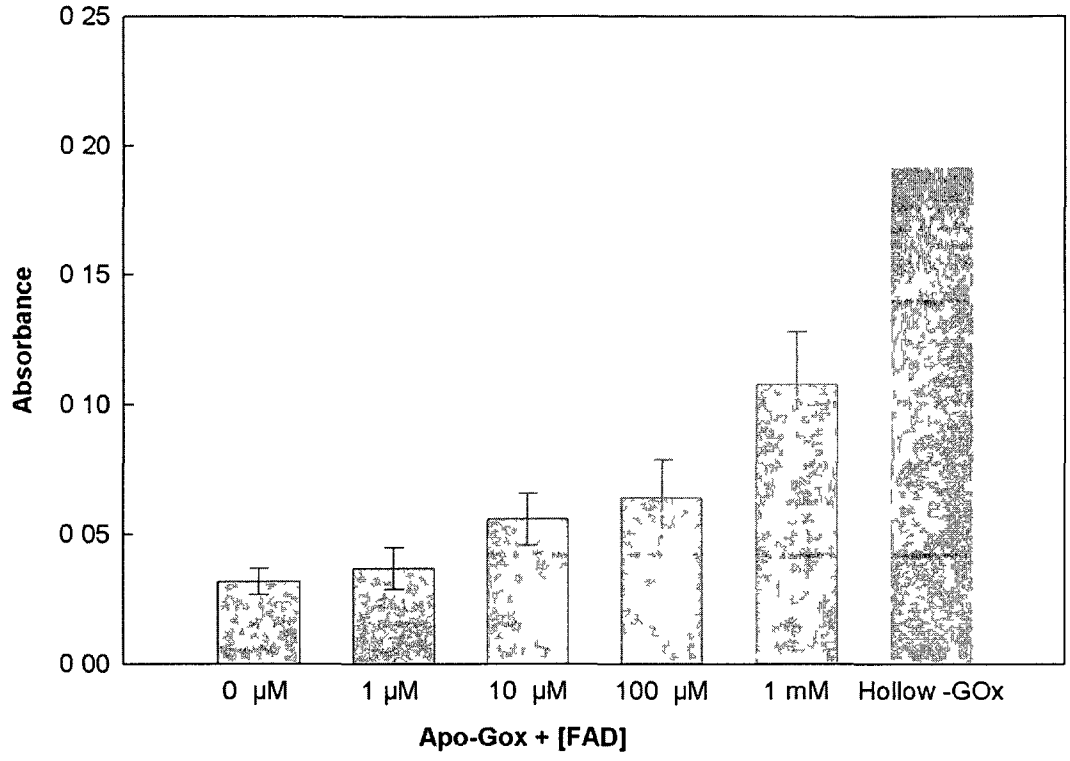

Figure 5.1 Reactivation of Apo-GOx with various FAD concentrations.

APPENDIX A

CELL PREPARATION AND CELLULAR MEDIAS

A.1 Cellular Medias

A.1.1 Preparation of CRL-2303 (glioma cells) Media

1. Add 125 ml of DMEM to the sterile filtration unit
2. Add 25 ml of (5%) Fetal Bovine Serum to the sterile filtration unit
3. Add 1.25 ml of (5%) penicillin/streptomycin to the sterile filtration unit
4. Add 111.25 ml of DMEM to the sterile filtration unit
5. Turn on the vacuum till entire the liquid run down to the container
6. Turn off the vacuum, then remove the filtration unit from the container
7. Place and close the cap on the container
8. Label the media container by CRL-2303, date, maker's name
9. Store the container in the refrigerator

A.1.2 Preparation of Astrocytes Media

1. Add 125 ml of Ham's F-12K to the sterile filtration unit
2. Add 25 ml of Horse Serum to the sterile filtration unit
3. Add 25 ml of (5%) Fetal Bovine Serum to the sterile filtration unit
4. Add 1.25 ml of (5%) penicillin/streptomycin to the sterile filtration unit
5. Add 123.75 ml of Ham's F-12K to the sterile filtration unit
6. Turn on the vacuum till the entire liquid run down to the container
7. Turn off the vacuum, then remove the filtration unit from the container
8. Place and close the cap on the container
9. Label the media container by astrocytes, date, maker's name
10. Store the container in the refrigerator

A.2 Preparation of 24 Well Cell Plate

1. Remove the media from 25 cm^3 flask
2. Wash flask with 3 ml of PBS (phosphate buffer saline)
3. Remove three ml of PBS from the flask
4. Add 3 ml of trypsin into the flask to detach cells from the surface
5. Neutralize trypsin with 7 ml of fresh media
6. Transfer 10 ml of trypsin and media into the centrifuge tube
7. Add 7 ml of fresh media into the flask
8. Centrifuge the tube at 160 rcf for 7 min
9. Remove supernatant from the tube
10. Shake the precipitation till it is mixable
11. Add 3 ml of fresh media into the tube
12. Softly mix the tube on the mixer
13. Count the cells via hemocytometer to find the wanted density of cells
14. Add the concentrated volume into the flask to have the wanted density
15. Incubate the flask at 37 °C, 5% CO_2, 90% humidity
16. Prepare a new tube for 24-wells plate with wanted density from the 3 ml tube
17. Add 0.5 ml of cell solution into each well (12 ml)
18. Incubate the plate at 37 °C , 5% CO_2, 90% humidity for 24 hrs

REFERENCES

[1] T. M. Squires and S. R. Quake, "Microfluidics: Fluid physics at the nanoliter scale," *Reviews of Modern Physics,* vol. 77, pp. 977-1026, 2005.

[2] S. K. Kanakamedala and C.O'Neal, "Dimensionless numbers in microfluidics," Review paper ENGR 610, College of Engineering and Science, Louisiana Tech University, August 15, 2011.

[3] J. W. Joyce, "Fluidics: Basic components and applications," *Special Report HDL-SR-83-9, Harry Diamond Laboratories,* 1983.

[4] D. J. Beebe, G. A. Mensing, and G. M. Walker, "Physics and applications of microfluidics in biology," in *Annual Review of Biomedical Engineering.* vol. 4, pp. 261-286, 2002

[5] J. C. McDonald, D. C. Duffy, J. R. Anderson, D. T. Chiu, H. Wu, O. J. A. Schueller, and G. M. Whitesides, "Fabrication of microfluidic systems in poly(dimethylsiloxane)," *Electrophoresis,* vol. 21, pp. 27-40, 2000.

[6] H. Feng, A. Gaur, S. Yugang, M. Word, J. Niu, I. Adesida, M. Shim, A. Shim, and J. A. Rogers, "Processing dependent behavior of soft imprint lithography on the 1-10-nm scale," *Nanotechnology, IEEE Transactions on,* vol. 5, pp. 301-308, 2006.

[7] H. Becker and C. Gartner, "Polymer microfabrication technologies for microfluidic systems," *Analytical and Bioanalytical Chemistry,* vol. 390, pp. 89-111, 2008.

[8] S. K. Kanakamedala and C.O'Neal, "Polymer microfluidic device fabrication technologies," Review paper ENGR 610, College of Engineering and Science, Louisiana Tech University, August 25, 2011.

[9] A. Bertsch, H. Lorenz, and P. Renaud, "3D microfabrication by combining microstereolithography and thick resist UV lithography," *Sensors and Actuators A: Physical,* vol. 73, pp. 14-23, 1999.

[10] C. Khan Malek, "Laser processing for bio-microfluidics applications (part I)," *Analytical and Bioanalytical Chemistry,* vol. 385, pp. 1351-1361, 2006.

[11] Y.-J. Juang, L. J. Lee, and K. W. Koelling, "Hot embossing in microfabrication. Part I: Experimental," *Polymer Engineering & Science,* vol. 42, pp. 539-550, 2002.

[12] R. Truckenmüller, S. Giselbrecht, N. Rivron, E. Gottwald, V. Saile, A. van den Berg, M. Wessling, and C. van Blitterswijk, "Thermoforming of Film-Based Biomedical Microdevices," *Advanced Materials,* vol. 23, pp. 1311-1329, 2011.

[13] D. A. Mair, E. Geiger, A. P. Pisano, J. M. J. Frechet, and F. Svec, "Injection molded microfluidic chips featuring integrated interconnects," *Lab on a Chip,* vol. 6, pp. 1346-1354, 2006.

[14] D. A. Bartholomeusz, R. W. Boutte, and J. D. Andrade, "Xurography: Rapid prototyping of microstructures using a cutting plotter," *Journal of Microelectromechanical Systems,* vol. 14, pp. 1364-1374, 2005.

[15] C. K. Chiang, C. R. Fincher Jr, Y. W. Park, A. J. Heeger, H. Shirakawa, E. J. Louis, S. C. Gau, and A. G. MacDiarmid, "Electrical conductivity in doped polyacetylene," *Physical Review Letters,* vol. 39, pp. 1098-1101, 1977.

[16] D. Nilsson, M. Chen, T. Kugler, T. Remonen, M. Armgarth, and M. Berggren, "Bi-stable and dynamic current modulation in electrochemical organic transistors," *Advanced Materials,* vol. 14, pp. 51-54, 2002.

[17] J. Liu, M. Agarwal, and K. Varahramyan, "Glucose sensor based on organic thin film transistor using glucose oxidase and conducting polymer," *Sensors and Actuators, B: Chemical,* vol. 135, pp. 195-199, 2008.

[18] "Introduction to organic electronics Webpage, http://www.phys.unsw.edu.au/~arh/background/Organic%20Electronics/Organics.-html", 2010.

[19] Y. Lvov, K. Ariga, M. Onda, I. Ichinose, and T. Kunitake, "Alternate Assembly of Ordered Multilayers of SiO_2 and Other Nanoparticles and Polyions," *Langmuir,* vol. 13, pp. 6195-6203, 1997.

[20] M. Agarwal, Y. Lvov, and K. Varahramyan, "Conductive wood microfibres for smart paper through layer-by-layer nanocoating," *Nanotechnology,* vol. 17, pp. 5319-5325, 2006.

[21] M. Plotner, T. Wegener, S. Richter, S. Howitz, and W.-J. Fischer, "Investigation of ink-jet printing of poly-3-octylthiophene for organic field-effect transistors from different solutions," *Synthetic Metals,* vol. 147, pp. 299-303, 2004.

[22] D. Nilsson, "An Organic Electrochemical Transistor for Printed Sensors and Logic," *Science and Technology,* pp. 35-45, 2005.

[23] V. Saxena, V. Shirodkar, and R. Prakash, "A comparative study of a polyindole-based microelectrochemical transistor in aqueous and non-aqueous electrolytes," *Journal of Solid State Electrochemistry,* vol. 4, pp. 231-233, 2000.

[24] S. J. Kim, K. V. Gobi, R. Harada, D. R. Shankaran, and N. Miura, "Miniaturized portable surface plasmon resonance immunosensor applicable for on-site detection of low-molecular-weight analytes," *Sensors and Actuators B: Chemical,* vol. 115, pp. 349-356, 2006.

[25] S. J. Kim, K. V. Gobi, H. Tanaka, Y. Shoyama, and N. Miura, "A simple and versatile self-assembled monolayer based surface plasmon resonance immunosensor for highly sensitive detection of 2,4-D from natural water resources," *Sensors and Actuators B: Chemical,* vol. 130, pp. 281-289, 2008.

[26] V. Hessel, H. Lowe, and F. Schonfeld, "Micromixers - A review on passive and active mixing principles," *Chemical Engineering Science,* vol. 60, pp. 2479-2501, 2005.

[27] N. T. Nguyen and Z. Wu, "Micromixers - A review," *Journal of Micromechanics and Microengineering,* vol. 15, pp. R1-R16, 2005.

[28] S. K. Kanakamedala and C.O'Neal, "Active and passive micromixers," Review paper ENGR 610, College of Engineering and Science, Louisiana Tech University, August 18, 2011.

[29] G. S. Jeong, S. Chung, C. B. Kim, and S. H. Lee, "Applications of micromixing technology," *Analyst,* vol. 135, pp. 460-473, 2010.

[30] E. A. Mansur, M. Ye, Y. Wang, and Y. Dai, "A state-of-the-art review of mixing in microfluidic mixers," *Chinese Journal of Chemical Engineering,* vol. 16, pp. 503-516, 2008.

[31] T. Fujii, Y. Sando, K. Higashino, and Y. Fujii, "A plug and play microfluidic device," *Lab on a Chip - Miniaturisation for Chemistry and Biology,* vol. 3, pp. 193-197, 2003.

[32] I. Glasgow and N. Aubry, "Enhancement of microfluidic mixing using time pulsing," *Lab on a Chip - Miniaturisation for Chemistry and Biology,* vol. 3, pp. 114-120, 2003.

[33] X. Niu and Y. K. Lee, "Efficient spatial-temporal chaotic mixing in microchannels," *Journal of Micromechanics and Microengineering,* vol. 13, pp. 454-462, 2003.

[34] L. H. Lu, K. S. Ryu, and C. Liu, "A magnetic microstirrer and array for microfluidic mixing," *Journal of Microelectromechanical Systems,* vol. 11, pp. 462-469, 2002.

[35] A. O. Moctar, N. Aubry, and J. Batton, "Electro-hydrodynamic micro-fluidic mixer," *Lab on a Chip - Miniaturisation for Chemistry and Biology,* vol. 3, pp. 273-280, 2003.

[36] J. Deval, P. Tabeling, and C. M. Ho, "A dielectrophoretic chaotic mixer," in *Proceedings of the IEEE Micro Electro Mechanical Systems (MEMS)*, pp. 36-39, 2002.

[37] Y. K. Lee, J. Deval, P. Tabeling, and C. M. Ho, "Chaotic mixing in electrokinetically and pressure driven micro flows," in *Proceedings of the IEEE Micro Electro Mechanical Systems (MEMS)*, pp. 483-486, 2001.

[38] M. H. Oddy, J. G. Santiago, and J. C. Mikkelsen, "Electrokinetic instability micromixing," *Analytical Chemistry,* vol. 73, pp. 5822-5832, 2001.

[39] Z. Tang, S. Hong, D. Djukic, V. Modi, A. C. West, J. Yardley, and R. M. Osgood, "Electrokinetic flow control for composition modulation in a microchannel," *Journal of Micromechanics and Microengineering,* vol. 12, pp. 870-877, 2002.

[40] H. H. Bau, J. Zhong, and M. Yi, "A minute magneto hydro dynamic (MHD) mixer," *Sensors and Actuators, B: Chemical,* vol. 79, pp. 207-215, 2001.

[41] R. M. Moroney, R. M. White, and R. T. Howe, "Ultrasonically induced microtransport with cylindrical geometry," in *American Society of Mechanical Engineers, Dynamic Systems and Control Division (Publication) DSC*, pp. 181-190, 1991.

[42] X. Zhu and E. S. Kim, "Acoustic-wave liquid mixer," *American Society of Mechanical Engineers, Dynamic Systems and Control Division (Publication) DSC,* vol. 62, pp. 35-38, 1997.

[43] K. Yasuda, "Non-destructive, non-contact handling method for biomaterials in micro-chamber by ultrasound," *Sensors and Actuators, B: Chemical,* vol. 64, pp. 128-135, 2000.

[44] H. Mao, T. Yang, and P. S. Cremer, "A Microfluidic Device with a Linear Temperature Gradient for Parallel and Combinatorial Measurements," *Journal of the American Chemical Society,* vol. 124, pp. 4432-4435, 2002.

[45] T. T. Veenstra, T. S. J. Lammerink, M. C. Elwenspoek, and A. Van Den Berg, "Characterization method for a new diffusion mixer applicable in micro flow injection analysis systems," *Journal of Micromechanics and Microengineering,* vol. 9, pp. 199-202, 1999.

[46] R. J. Jackman, T. M. Floyd, R. Ghodssi, M. A. Schmidt, and K. F. Jensen, "Microfluidic systems with on-line UV detection fabricated in photodefinable epoxy," *Journal of Micromechanics and Microengineering,* vol. 11, pp. 263-269, 2001.

[47] M. Koch, H. Witt, A. G. R. Evans, and A. Brunnschweiler, "Improved characterization technique for micromixers," *Journal of Micromechanics and Microengineering,* vol. 9, pp. 156-158, 1999.

[48] A. G. Hadd, D. E. Raymond, J. W. Halliwell, S. C. Jacobson, and J. M. Ramsey, "Microchip Device for Performing Enzyme Assays," *Analytical Chemistry,* vol. 69, pp. 3407-3412, 1997.

[49] J. B. Knight, A. Vishwanath, J. P. Brody, and R. H. Austin, "Hydrodynamic focusing on a silicon chip: Mixing nanoliters in microseconds," *Physical Review Letters,* vol. 80, pp. 3863-3866, 1998.

[50] B. L. Gray, D. Jaeggi, N. J. Mourlas, B. P. Van Drieenhuizen, K. R. Williams, N. I. Maluf, and G. T. A. Kovacs, "Novel interconnection technologies for integrated microfluidic systems," *Sensors and Actuators, A: Physical,* vol. 77, pp. 57-65, 1999.

[51] M. S. Munson and P. Yager, "Simple quantitative optical method for monitoring the extent of mixing applied to a novel microfluidic mixer," *Analytica Chimica Acta,* vol. 507, pp. 63-71, 2004.

[52] Y. Lin, G. J. Gerfen, D. L. Rousseau, and S. R. Yeh, "Ultrafast Microfluidic Mixer and Freeze-Quenching Device," *Analytical Chemistry,* vol. 75, pp. 5381-5386, 2003.

[53] V. Mengeaud, J. Josserand, and H. H. Girault, "Mixing processes in a zigzag microchannel: Finite element simulations and optical study," *Analytical Chemistry,* vol. 74, pp. 4279-4286, 2002.

[54] C. C. Hong, J. W. Choi, and C. H. Ahn, "A novel in-plane passive microfluidic mixer with modified Tesla structures," *Lab on a Chip - Miniaturisation for Chemistry and Biology,* vol. 4, pp. 109-113, 2004.

[55] R. A. Vijayendran, K. M. Motseggod, D. J. Beebe, and D. E. Leckband, "Evaluation of a Three-Dimensional micormixer in a surface-based biosensors," *Langmuir*, vol. 19, pp. 1824-1828, 2002.

[56] T. J. Johnson, D. Ross, and L. E. Locascio, "Rapid microfluidic mixing," *Analytical Chemistry,* vol. 74, pp. 45-51, 2002.

[57] A. D. Stroock and G. M. Whitesides, "Controlling flows in microchannels with patterned surface charge and topography," *Accounts of Chemical Research,* vol. 36, pp. 597-604, 2003.

[58] K. Hosokawa, T. Fujii, and I. Endo, "Droplet-based nano/picoliter mixer using hydrophobic microcapillary vent," in *Proceedings of the IEEE Micro Electro Mechanical Systems (MEMS)*, pp. 388-393, 1999.

[59] P. Paik, V. K. Pamula, and R. B. Fair, "Rapid droplet mixers for digital microfluidic systems," *Lab on a Chip - Miniaturisation for Chemistry and Biology,* vol. 3, pp. 253-259, 2003.

[60] J. D. Tice, A. D. Lyon, and R. F. Ismagilov, "Effects of viscosity on droplet formation and mixing in microfluidic channels," *Analytica Chimica Acta,* vol. 507, pp. 73-77, 2004.

[61] "Mit Webpage, http://web.mit.edu/fluids-modules/www/basic_laws/1-7vorti.pdf" 2010.

[62] J. D. Anderson, "Compulational Fluid Dynamics – The Basics with Applications," *West Nyack, New York, USA: Cambridge Univ.*, 1995.

[63] "Coventor Webpage, http://www.coventor.com/about/index.html" 2010.

[64] J. T. Yang, W. F. Fang, and K. Y. Tung, "Fluids mixing in devices with connected-groove channels," *Chemical Engineering Science,* vol. 63, pp. 1871-1881, 2008.

[65] M. A. Eddings, M. A. Johnson, and B. K. Gale, "Determining the optimal PDMS-PDMS bonding technique for microfluidic devices," *Journal of Micromechanics and Microengineering,* vol. 18, 2008.

[66] J. H. Burroughes, D. D. C. Bradley, A. R. Brown, R. N. Marks, K. Mackay, R. H. Friend, P. L. Burns, and A. B. Holmes, "Light-emitting diodes based on conjugated polymers," *Nature,* vol. 347, pp. 539-541, 1990.

[67] H. Tanaka, T. Yasuda, K. Fujita, and T. Tsutsui, "Transparent image sensors using an organic multilayer photodiode," *Advanced Materials,* vol. 18, pp. 2230-2233, 2006.

[68] B. A. Gregg, "Excitonic solar cells," *Journal of Physical Chemistry B,* vol. 107, pp. 4688-4698, 2003.

[69] B. Chen, T. Cui, Y. Liu, and K. Varahramyan, "All-polymer RC filter circuits fabricated with inkjet printing technology," *Solid-State Electronics,* vol. 47, pp. 841-847, 2003.

[70] "Official Nobel Prize Webpage, http://nobelprize.org " 2011.

[71] D. W. Van Krevelen, K. Te Nijenhuis, and I. NetLibrary, "Properties of polymers: Their correlation with chemical structure; their numerical estimation and prediction from additive group contributions," 1990.

[72] A. Sionkowska, "The influence of UV light on collagen/poly (ethylene glycol) blends," *Polymer degradation and stability,* vol. 91, pp. 305-312, 2006.

[73] M. Nikolou and G. G. Malliaras, "Applications of poly (3,4-ethylenedioxythiophene) doped with poly(styrene sulfonic acid) transistors in chemical and biological sensors," *Chemical Record,* vol. 8, pp. 13-22, 2008.

[74] A. Kassim, H. N. M. E. Mahmud, L. M. Yee, and N. Hanipah, "Electrochemical Preparation and Characterization of Polypyrrole-Polyethylene Glycol Conducting Polymer Composite Films," *The Pacific Journal of Science and Technology,* vol. 7, pp. 103-107, 2006.

[75] J. Isaksson, "Organic bioelectronics,", Ph.D. dissertation, Linköping university, Linköping, Southern Sweden, 2007.

[76] J. Roncali, "Conjugated poly (thiophenes): Synthesis, functionalization, and applications," *Chemical reviews,* vol. 92, pp. 711-738, 1992.

[77] A. R. Blythe and D. Bloor, *Electrical properties of polymers*: Cambridge Univ Pr, 2005.

[78] K. S. Teh and L. Lin, "MEMS sensor material based on polypyrrole–carbon nanotube nanocomposite: Film deposition and characterization," *Journal of Micromechanics and Microengineering,* vol. 15, p. 2019, 2005.

[79] D. Nilsson, T. Kugler, P. O. Svensson, and M. Berggren, "An all-organic sensor-transistor based on a novel electrochemical transducer concept printed electrochemical sensors on paper," *Sensors and Actuators B: Chemical,* vol. 86, pp. 193-197, 2002.

[80] J. M. Poate, H. J. Leamy, T. T. Sheng, and G. K. Celler, "Polyacetylene,(CH)[sub x]: n-type and p-type doping and compensation," *Appl. Phys. Lett,* vol. 33, p. 18, 1978.

[81] J. L. Bredas, B. Themans, J. M. Andre, R. R. Chance, and R. Silbey, "The role of mobile organic radicals and ions (solitons, polarons and bipolarons) in the transport properties of doped conjugated polymers," *Synthetic metals,* vol. 9, pp. 265-274, 1984.

[82] Y. Furukawa, A. Sakamoto, H. Ohta, and M. Tasumi, "Raman characterization of polarons, bipolarons and solitons in conducting polymers," *Synthetic metals,* vol. 49, pp. 335-340, 1992.

[83] W. R. Salaneck and I. Lundström, "Electrically Conducting Organic Polymers: Connections Between Geometric and Electronic Structure," *Physica Scripta,* vol. 1989, p. 9, 1989.

[84] D. Nilson, "An organic electrochemical transistor for printed sensors and logic," M.S. thesis, Linköping university, Linköping, Southern Sweden, 2005.

[85] W. R. Salaneck, R. H. Friend, and J. L. Brédas, "Electronic structure of conjugated polymers: Consequences of electron-lattice coupling," *Physics reports,* vol. 319, pp. 231-251, 1999.

[86] L. Rupprecht, *Conductive polymers and plastics in industrial applications*: William Andrew Inc., 1999.

[87] C. Q. Wu, Y. Qiu, Z. An, and K. Nasu, "Dynamical study on polaron formation in a metal/polymer/metal structure," *Physical Review B,* vol. 68, p. 125416, 2003.

[88] J. Liu, "Poly(ethylenedioxythiophene) based electronic devices for sensor applications," Ph.D. dissertation, Louisiana Tech University, Ruston, LA, USA, 2008.

[89] A. J. Heeger, "Semiconducting and metallic polymers: The fourth generation of polymeric materials," *Current Applied Physics,* vol. 1, pp. 247-267, 2001.

[90] D. Ofer, R. M. Crooks, and M. S. Wrighton, "Potential dependence of the conductivity of highly oxidized polythiophenes, polypyrroles, and polyaniline: Finite windows of high conductivity," *Journal of the American Chemical Society,* vol. 112, pp. 7869-7879, 1990.

[91] P. R. Somani and S. Radhakrishnan, "Electrochromic materials and devices: Present and future," *Materials Chemistry and Physics,* vol. 77, pp. 117-133, 2003.

[92] R. J. Mortimer, "Organic electrochromic materials," *Electrochimica acta,* vol. 44, pp. 2971-2981, 1999.

[93] F. Carpi and D. De Rossi, "Colours from electroactive polymers: Electrochromic, electroluminescent and laser devices based on organic materials," *Optics & Laser Technology,* vol. 38, pp. 292-305, 2006.

[94] P. Andersson, D. Nilsson, P. O. Svensson, M. Chen, A. Malmström, T. Remonen, T. Kugler, and M. Berggren, "Active matrix displays based on all organic electrochemical smart pixels printed on paper," *Advanced Materials,* vol. 14, pp. 1460-1464, 2002.

[95] H. W. Heuer, R. Wehrmann, and S. Kirchmeyer, "Electrochromic window based on conducting poly (3, 4 ethylenedioxythiophene)–poly (styrene sulfonate)," *Advanced Functional Materials,* vol. 12, pp. 89-94, 2002.

[96] E. H. Jager, E. Smela, and O. Inganäs, "Microfabricating conjugated polymer actuators," *Science,* vol. 290, p. 1540, 2000.

[97] E. Smela, "Conjugated polymer actuators for biomedical applications," *Advanced Materials,* vol. 15, pp. 481-494, 2003.

[98] E. Smela, O. Inganäs, and I. Lundström, "Controlled folding of micrometer-size structures," *Science,* vol. 268, p. 1735, 1995.

[99] J. Bobacka, "Potential stability of all-solid-state ion-selective electrodes using conducting polymers as ion-to-electron transducers," *Analytical Chemistry,* vol. 71, pp. 4932-4937, 1999.

[100] P. M. George, D. A. LaVan, J. A. Burdick, C. Y. Chen, E. Liang, and R. Langer, "Electrically controlled drug delivery from biotin doped conductive polypyrrole," *Advanced Materials,* vol. 18, pp. 577-581, 2006.

[101] R. Wadhwa, C. F. Lagenaur, and X. T. Cui, "Electrochemically controlled release of dexamethasone from conducting polymer polypyrrole coated electrode," *Journal of controlled release,* vol. 110, pp. 531-541, 2006.

[102] J. Bobacka, A. Lewenstam, and A. Ivaska, "Electrochemical impedance spectroscopy of oxidized poly (3, 4-ethylenedioxythiophene) film electrodes in aqueous solutions," *Journal of Electroanalytical Chemistry,* vol. 489, pp. 17-27, 2000.

[103] A. Lisowska-Oleksiak and A. Kupniewska, "Transport of alkali metal cations in poly (3, 4-ethylenethiophene) films," *Solid state ionics,* vol. 157, pp. 241-248, 2003.

[104] X. Wang, B. Shapiro, and E. Smela, "Visualizing ion currents in conjugated polymers," *Advanced Materials,* vol. 16, pp. 1605-1609, 2004.

[105] G. Greczynski, T. Kugler, M. Keil, W. Osikowicz, M. Fahlman, and W. R. Salaneck, "Photoelectron spectroscopy of thin films of PEDOT-PSS conjugated polymer blend: a mini-review and some new results," *Journal of Electron Spectroscopy and Related Phenomena,* vol. 121, pp. 1-17, 2001.

[106] L. Groenendaal, F. Jonas, D. Freitag, H. Pielartzik, and J. R. Reynolds, "Poly (3, 4-ethylenedioxythiophene) and its derivatives: Past, present, and future," *Advanced Materials,* vol. 12, pp. 481-494, 2000.

[107] C. J. Drury, C. M. J. Mutsaers, C. M. Hart, M. Matters, and D. M. De Leeuw, "Low-cost all-polymer integrated circuits," *Applied Physics Letters,* vol. 73, pp. 108-110, 1998.

[108] M. Matters, D. M. De Leeuw, M. Vissenberg, C. M. Hart, P. T. Herwig, T. Geuns, C. M. J. Mutsaers, and C. J. Drury, "Organic field-effect transistors and all-polymer integrated circuits," *Optical Materials,* vol. 12, pp. 189-197, 1999.

[109] A. Dodabalapur, "Organic light emitting diodes," *Solid state communications,* vol. 102, pp. 259-267, 1997.

[110] K. Murata, S. Izuchi, and Y. Yoshihisa, "An overview of the research and development of solid polymer electrolyte batteries," *Electrochimica acta,* vol. 45, pp. 1501-1508, 2000.

[111] J. Y. Song, Y. Y. Wang, and C. C. Wan, "Review of gel-type polymer electrolytes for lithium-ion batteries," *Journal of Power Sources,* vol. 77, pp. 183-197, 1999.

[112] K. Gurunathan, A. V. Murugan, R. Marimuthu, U. P. Mulik, and D. P. Amalnerkar, "Electrochemically synthesised conducting polymeric materials for applications towards technology in electronics, optoelectronics and energy storage devices," *Materials Chemistry and Physics,* vol. 61, pp. 173-191, 1999.

[113] R. D. Rauh, F. Wang, J. R. Reynolds, and D. L. Meeker, "High coloration efficiency electrochromics and their application to multi-color devices," *Electrochimica Acta,* vol. 46, pp. 2023-2029, 2001.

[114] J. C. Gustafsson-Carlberg, O. Inganäs, M. R. Andersson, C. Booth, A. Azens, and C. G. Granqvist, "Tuning the bandgap for polymeric smart windows and displays," *Electrochimica acta,* vol. 40, pp. 2233-2235, 1995.

[115] Q. Pei, G. Yu, C. Zhang, Y. Yang, and A. J. Heeger, "Polymer light-emitting electrochemical cells," *Science,* vol. 269, p. 1086, 1995.

[116] T. Johansson, W. Mammo, M. R. Andersson, and O. Inganäs, "Light-emitting electrochemical cells from oligo (ethylene oxide)-substituted polythiophenes: Evidence for in situ doping," *Chemistry of Materials,* vol. 11, pp. 3133-3139, 1999.

[117] B. Wessling, "Scientific and commercial breakthrough for organic metals," *Synthetic metals,* vol. 85, pp. 1313-1318, 1997.

[118] S. Möller, C. Perlov, W. Jackson, C. Taussig, and S. R. Forrest, "A polymer/semiconductor write-once read-many-times memory," *Nature,* vol. 426, pp. 166-169, 2003.

[119] S. Ghosh and O. Inganäs, "Networks of Electron-Conducting Polymer in Matrices of Ion-Conducting Polymers Applications to Fast Electrodes," *Electrochemical and Solid-State Letters,* vol. 3, p. 213, 2000.

[120] Y. Cao, G. Yu, C. Zhang, R. Menon, and A. J. Heeger, "Polymer light-emitting diodes with polyethylene dioxythiophene-polystyrene sulfonate as the transparent anode," *Synthetic Metals,* vol. 87, pp. 171-174, 1997.

[121] L. A. A. Pettersson, F. Carlsson, O. Inganäs, and H. Arwin, "Spectroscopic ellipsometry studies of the optical properties of doped poly (3, 4-ethylenedioxythiophene): An anisotropic metal," *Thin Solid Films,* vol. 313, pp. 356-361, 1998.

[122] T. A. Skotheim and J. R. Reynolds, *Handbook of Conducting Polymers*: CRC, 2007.

[123] M. M. De Kok, M. Buechel, S. E. Vulto, P. Van De Weijer, E. A. Meulenkamp, S. De Winter, A. J. G. Mank, H. J. M. Vorstenbosch, C. H. L. Weijtens, and V. Van Elsbergen, "Modification of PEDOT: PSS as hole injection layer in polymer LEDs," *Physica Sstatus Solidi (a),* vol. 201, pp. 1342-1359, 2004.

[124] A. M. Nardes, *On the conductivity of PEDOT: PSS thin films*: Technische Universiteit Eindhoven, 2007.

[125] J. Ouyang, C. W. Chu, F. C. Chen, Q. Xu, and Y. Yang, "Polymer optoelectronic devices with high-conductivity poly (3, 4-ethylenedioxythiophene) anodes," *Journal of Macromolecular Science, Part A,* vol. 41, pp. 1497-1511, 2004.

[126] A. Elschner, F. Bruder, H. W. Heuer, F. Jonas, A. Karbach, S. Kirchmeyer, S. Thurm, and R. Wehrmann, "PEDT/PSS for efficient hole-injection in hybrid organic light-emitting diodes," *Synthetic Metals,* vol. 111, pp. 139-143, 2000.

[127] G. Fichet, N. Corcoran, P. H. Ho, A. C. Arias, J. D. MacKenzie, W. T. S. Huck, and R. H. Friend, "Self Organized Photonic Structures in Polymer Light Emitting Diodes," *Advanced Materials,* vol. 16, pp. 1908-1912, 2004.

[128] M. Yeon Song, K. J. Kim, and D. Y. Kim, "Enhancement of photovoltaic characteristics using a PEDOT interlayer in TiO_2/MEHPPV heterojunction devices," *Solar Energy Materials and Solar Cells,* vol. 85, pp. 31-39, 2005.

[129] F. Zhang, M. Johansson, M. R. Andersson, J. C. Hummelen, and O. Inganäs, "Polymer photovoltaic cells with conducting polymer anodes," *Advanced Materials,* vol. 14, pp. 662-665, 2002.

[130] D. Nilsson, N. Robinson, M. Berggren, and R. Forchheimer, "Electrochemical logic circuits," *Advanced Materials,* vol. 17, pp. 353-358, 2005.

[131] M. Vazquez, P. Danielsson, J. Bobacka, A. Lewenstam, and A. Ivaska, "Solution-cast films of poly (3, 4-ethylenedioxythiophene) as ion-to-electron transducers in all-solid-state ion-selective electrodes," *Sensors and Actuators B: Chemical,* vol. 97, pp. 182-189, 2004.

[132] P. Asberg and O. Inganas, "Hydrogels of a conducting conjugated polymer as 3-D enzyme electrode," *Biosensors and Bioelectronics,* vol. 19, pp. 199-207, 2003.

[133] X. Cui and D. C. Martin, "Electrochemical deposition and characterization of poly (3, 4-ethylenedioxythiophene) on neural microelectrode arrays," *Sensors and Actuators B: Chemical,* vol. 89, pp. 92-102, 2003.

[134] T. G. Backlund, H. O. Sandberg, R. Osterbacka, H. Stubb, T. Makela, and S. Jussila, "Towards all-polymer field-effect transistors with solution processable materials," *Synthetic Metals,* vol. 148, pp. 87-91, 2005.

[135] F. Garnier, R. Hajlaoui, A. Yassar, and P. Srivastava, "All-polymer field-effect transistor realized by printing techniques," *Science,* vol. 265, p. 1684, 1994.

[136] H. Sirringhaus, N. Tessler, and R. H. Friend, "Integrated, high-mobility polymer field-effect transistors driving polymer light-emitting diodes," *Synthetic Metals,* vol. 102, pp. 857-860, 1999.

[137] H. S. White, G. P. Kittlesen, and M. S. Wrighton, "Chemical derivatization of an array of three gold microelectrodes with polypyrrole: Fabrication of a molecule-based transistor," *Journal of the American Chemical Society,* vol. 106, pp. 5375-5377, 1984.

[138] J. Huang and M. S. Wrighton, "Microelectrochemical multitransistor devices based on electrostatic binding of electroactive anionic metal complexes in proto-nated poly (4-vinylpyridine): devices that can detect and distinguish up to three species simultaneously," *Analytical Chemistry,* vol. 65, pp. 2740-2746, 1993.

[139] J. W. Thackeray, H. S. White, and M. S. Wrighton, "Poly (3-methylthiophene)-coated electrodes: Optical and electrical properties as a function of redox potential and amplification of electrical and chemical signals using poly (3-methylthiophene)-based microelectrochemical transistors," *The Journal of Physi-cal Chemistry,* vol. 89, pp. 5133-5140, 1985.

[140] Z. T. Zhu, J. T. Mabeck, C. Zhu, N. C. Cady, C. A. Batt, and G. G. Malliaras, "A simple poly (3, 4-ethylene dioxythiophene)/poly (styrene sulfonic acid) transistor for glucose sensing at neutral pH," *Chemical Communication,* pp. 1556-1557, 2004.

[141] D. A. Bernards, G. G. Malliaras, G. E. S. Toombes, and S. M. Gruner, "Gating of an organic transistor through a bilayer lipid membrane with ion channels," *Ap-plied physics letters,* vol. 89, p. 053505, 2006.

[142] S. Ashizawa, Y. Shinohara, H. Shindo, Y. Watanabe, and H. Okuzaki, "Polymer FET with a conducting channel," *Synthetic metals,* vol. 153, pp. 41-44, 2005.

[143] D. A. Bernards and G. G. Malliaras, "Steady State and Transient Behavior of Or-ganic Electrochemical Transistors," *Advanced Functional Materials,* vol. 17, pp. 3538-3544, 2007.

[144] J. Ouyang, Q. Xu, C. W. Chu, Y. Yang, G. Li, and J. Shinar, "On the mechanism of conductivity enhancement in poly(3,4- ethylenedioxythiophene):poly(styrene sulfonate) film through solvent treatment," *Polymer,* vol. 45, pp. 8443-8450, 2004.

[145] M. Berggren, R. Forchheimer, J. Bobacka, P. O. Svensson, D. Nilsson, O. Lars-son, and A. Ivaska, "PEDOT: PSS-based electrochemical transistors for ion-to-electron transduction and sensor signal amplification," *Organic Semiconductors in Sensor Applications,* pp. 263-280, 2008.

[146] D. A. Bernards and G. G. Malliaras, "Steady-state and transient behavior of organ-ic electrochemical transistors," *Advanced Functional Materials,* vol. 17, pp. 3538-3544, 2007.

[147] S. K. Kanakamedala, H. T. Alshakhouri, M. Agarwal, and M. A. DeCoster, "A simple polymer based electrochemical transistor for micromolar glucose sensing," *Sensors and Actuators B: Chemical,* vol. 157, pp. 92-97, 2011.

[148] G. Malliaras and R. Friend, "An organic electronics primer," *Physics Today,* vol. 58, pp. 53-58, 2005.

[149] L. Groenendaal, F. Jonas, D. Freitag, H. Pielartzik, and J. R. Reynolds, "Poly(3,4-ethylenedioxythiophene) and Its Derivatives: Past, Present, and Future," *Advanced Materials,* vol. 12, pp. 481-494, 2000.

[150] R. S. Phadke, "Biosensors and enzyme immobilized electrodes," *BioSystems,* vol. 27, pp. 203-206, 1992.

[151] A. Chaubey and B. D. Malhotra, "Mediated biosensors," *Biosensors and Bioelectronics,* vol. 17, pp. 441-456, 2002.

[152] M. Gerard, A. Chaubey, and B. D. Malhotra, "Application of conducting polymers to biosensors," *Biosensors and Bioelectronics,* vol. 17, pp. 345-359, 2002.

[153] D. R. Thevenot, K. Toth, R. A. Durst, and G. S. Wilson, "Electrochemical biosensors: Recommended definitions and classification," *Biosensors and Bioelectronics,* vol. 16, pp. 121-131, 2001.

[154] B. Xie, M. Khayyami, T. Nwosu, P. O. Larsson, and B. Danielsson, "Ferrocene-mediated thermal biosensor," *The Analyst,* vol. 118, pp. 845-848, 1993.

[155] J. I. Peterson and G. G. Vurek, "Fiber-optic sensors for biomedical applications," *Science,* vol. 224, pp. 123-127, 1984.

[156] J. M. Abad, F. Pariente, L. Hernandez, H. D. Abruna, and E. Lorenzo, "Determination of organophosphorus and carbamate pesticides using a piezoelectric biosensor," *Analytical Chemistry,* vol. 70, pp. 2848-2855, 1998.

[157] K. Ramanathan, S. S. Pandey, R. Kumar, A. Gulati, A. Surya, N. Murthy, and B. D. Malhotra, "Covalent immobilization of glucose oxidase to poly(o-amino benzoic acid) for application to glucose biosensor," *Journal of Applied Polymer Science,* vol. 78, pp. 662-667, 2000.

[158] G. Davis, "Electrochemical techniques for the development of amperometric biosensors," *Biosensors,* vol. 1, pp. 161-178, 1985.

[159] S. V. Dzyadevych, V. N. Arkhypova, A. P. Soldatkin, A. V. El'skaya, C. Martelet, and N. Jaffrezic-Renault, "Amperometric enzyme biosensors: Past, present and future," *ITBM-RBM,* vol. 29, pp. 171-180, 2008.

[160] "Centers for Disease Control and Prevention. National diabetes fact sheet: general information and national estimates on diabetes in the United States, 2007. Atlanta, GA: U.S. Department of Health and Human Services, Centers for Disease Control and Prevention, 2008 (http://www.cdc.gov/diabetes/pubs/pdf/ndfs_2007.pdf)."

[161] J. Boyle, T. Thompson, E. Gregg, L. Barker, and D. Williamson, "Projection of the year 2050 burden of diabetes in the US adult population: dynamic modeling of incidence, mortality, and prediabetes prevalence," *Population Health Metrics,* vol. 8, pp. 1-12, 2010.

[162] M. Yamaguchi, M. Mitsumori, and Y. Kano, "Noninvasively measuring blood glucose using saliva," *Engineering in Medicine and Biology Magazine, IEEE,* vol. 17, pp. 59-63, 1998.

[163] T. Saito and M. Watanabe, "Characterization of poly(vinylferrocene-co-2-hydroxyethyl methacrylate) for use as electron mediator in enzymatic glucose sensor," *Reactive and Functional Polymers,* vol. 37, pp. 263-269, 1998.

[164] D. J. Claremont, I. E. Sambrook, C. Penton, and J. C. Pickup, "Subcutaneous implantation of a ferrocene-mediated glucose sensor in pigs," *Diabetologia,* vol. 29, pp. 817-821, 1986.

[165] A. E. G. Cass, G. Davis, G. D. Francis, H. Allen O Hill, W. J. Aston, I. John Higgins, E. V. Plotkin, L. D. L. Scott, and A. P. F. Turner, "Ferrocene-mediated enzyme electrode for amperometric determination of glucose," *Analytical Chemistry",* vol. 56, pp. 667-671, 1984.

[166] D. J. Macaya, M. Nikolou, S. Takamatsu, J. T. Mabeck, R. M. Owens, and G. G. Malliaras, "Simple glucose sensors with micromolar sensitivity based on organic electrochemical transistors," *Sensors and Actuators, B: Chemical,* vol. 123, pp. 374-378, 2007.

[167] N. Y. Shim, D. A. Bernards, D. J. Macaya, J. A. DeFranco, M. Nikolou, R. M. Owens, and G. G. Malliaras, "All-plastic electrochemical transistor for glucose sensing using a ferrocene mediator," *Sensors,* vol. 9, pp. 9896-9902, 2009.

[168] M. Nedergaard, T. Takano, and A. J. Hansen, "Beyond the role of glutamate as a neurotransmitter," *Nature Reviews Neuroscience,* vol. 3, pp. 748-755, 2002.

[169] Y. Cui, J. P. Barford, and R. Renneberg, "Development of an interference-free biosensor for L-glutamate using a bienzyme salicylate hydroxylase/l-glutamate dehydrogenase system," *Enzyme and Microbial Technology,* vol. 41, pp. 689-693, 2007.

[170] T. Hayashi, "A physiological study of epileptic seizures following cortical stimulation in animals and its application to human clinics," *Japan Journal of Physiology,* vol. 1, pp. 46-64, 1952.

[171] D. R. Curtis, J. W. Phillis, and J. C. Watkins, "The chemical excitation of spinal neurones by certain acidic amino acids," *The Journal of Physiology,* vol. 150, pp. 656-682, 1960.

[172] M. Hollmann and S. Heinemann, "Cloned Glutamate Receptors," *Annual Review of Neuroscience,* vol. 17, pp. 31-108, 1994.

[173] R. Nieuwenhuys, "The neocortex: An overview of its evolutionary development, structural organization and synaptology," *Anatomy and Embryology,* vol. 190, pp. 307-337, 1994.

[174] D. C. Javitt, "Glutamate as a therapeutic target in psychiatric disorders," *Mol Psychiatry,* vol. 9, pp. 984-997, 2004.

[175] B. S. Meldrum, "Glutamate as a neurotransmitter in the brain: Review of physiology and pathology," *Journal of Nutrition,* vol. 130, pp. 1007S-1015S, 2000.

[176] Y. Hu, K. M. Mitchell, F. N. Albahadily, E. K. Michaelis, and G. S. Wilson, "Direct measurement of glutamate release in the brain using a dual enzyme-based electrochemical sensor," *Brain Research,* vol. 659, pp. 117-125, 1994.

[177] E. K. Michaelis, "Glutamate neurotransmission: Characteristics of NMDA receptors in the mammalian brain," *Neural Networks,* vol. 2, pp. 3-6, 1996.

[178] S. Chakraborty and C. Retna Raj, "Amperometric biosensing of glutamate using carbon nanotube based electrode," *Electrochemistry Communications,* vol. 9, pp. 1323-1330, 2007.

[179] D. W. Brann and V. B. Mahesh, "Excitatory amino acids: Evidence for a role in the control of reproduction and anterior pituitary hormone secretion," *Endocrine Reviews,* vol. 18, pp. 678-700, 1997.

[180] Y. Akagi, A. Hashigasako, P. Degenaar, S. Iwabuchi, Q. Hasan, Y. Morita, and E. Tamiya, "Enzyme-Linked Sensitive Fluorometric Imaging of Glutamate Release from Cerebral Neurons of Chick Embryos," *Journal of Biochemistry,* vol. 134, pp. 353-358, 2003.

[181] M. C. McGahan, J. Harned, M. Mukunnemkeril, M. Goralska, L. Fleisher, and J. B. Ferrell, "Iron alters glutamate secretion by regulating cytosolic aconitase activity," *American Journal of Physiology - Cell Physiology,* vol. 288, pp. C1117-C1124, 2005.

[182] R. Srinivasan, N. Sailasuta, R. Hurd, S. Nelson, and D. Pelletier, "Evidence of elevated glutamate in multiple sclerosis using magnetic resonance spectroscopy at 3 T," *Brain,* vol. 128, pp. 1016-1025, 2005.

[183] D. H. Allen, J. Delohery, and G. Baker, "Monosodium L-glutamate-induced asthma," *Journal of Allergy and Clinical Immunology,* vol. 80, pp. 530-537, 1987.

[184] A. K. Basu, P. Chattopadhyay, U. Roychudhuri, and R. Chakraborty, "A biosensor based on co-immobilized L-glutamate oxidase and L-glutamate dehydrogenase for analysis of monosodium glutamate in food," *Biosensors and Bioelectronics,* vol. 21, pp. 1968-1972, 2006.

[185] O. Niwa, K. Torimitsu, M. Morita, P. Osbome, and K. Yamamoto, "Concentration of extracellular l-glutamate released from cultured nerve cells measured with a small-volume online sensor," *Analytical Chemistry,* vol. 68, pp. 1865-1870, 1996.

[186] Y. Yu, Q. Sun, T. Zhou, M. Zhu, L. Jin, and G. Shi, "On-line microdialysis system with poly(amidoamine)-encapsulated Pt nanoparticles biosensor for glutamate sensing in vivo," *Bioelectrochemistry,* vol. 81, pp. 53-57.

[187] M. Backer, L. Delle, A. Poghossian, M. Biselli, W. Zang, P. Wagner, and M. J. Schening, "Electrochemical sensor array for bioprocess monitoring," *Electrochimica Acta, 2011.*

[188] K. Hayashi, R. Kurita, T. Horiuchi, and O. Niwa, "Selective detection of L-glutamate using a microfluidic device integrated with an enzyme-modified pre-reactor and an electrochemical detector," *Biosensors and Bioelectronics,* vol. 18, pp. 1249-1255, 2003.

[189] M. A. Rahman, N. H. Kwon, M. S. Won, E. S. Choe, and Y. B. Shim, "Functionalized conducting polymer as an enzyme-immobilizing substrate: An amperometric glutamate microbiosensor for in vivo measurements," *Analytical Chemistry,* vol. 77, pp. 4854-4860, 2005.

[190] M. M. Rahman, T. Yamazaki, T. Ikeda, M. Ishida, and K. Sawada, "Development of a glutamate biosensor based on glutamate oxidase using smart-biochips," in *TRANSDUCERS 2009 - 15th International Conference on Solid-State Sensors, Actuators and Microsystems*, pp. 88-91, 2009.

[191] K. M. Wassum, V. M. Tolosa, J. Wang, E. Walker, H. G. Monbouquette, and N. T. Maidment, "Silicon wafer-based platinum microelectrode array biosensor for near real-time measurement of glutamate in vivo," *Sensors,* vol. 8, pp. 5023-5036, 2008.

[192] M. Zhang, C. Mullens, and W. Gorski, "Amperometric glutamate biosensor based on chitosan enzyme film," *Electrochimica Acta,* vol. 51, pp. 4528-4532, 2006.

[193] S. J. Updike and G. P. Hicks, "Reagentless substrate analysis with immobilized enzymes," *Science,* vol. 158, pp. 270-272, 1967.

[194] P. C. Pandey, S. Glazier, and H. H. Weetall, "An amperometric flow-injection analysis biosensor for glucose based on graphite paste modified with tetracyanoquinodimethane," *Analytical Biochemistry,* vol. 214, pp. 233-237, 1993.

[195] S. Qin, M. Van Der Zeyden, W. H. Oldenziel, T. I. F. H. Cremers, and B. H. C. Westerink, "Microsensors for in vivo measurement of glutamate in brain tissue," *Sensors,* vol. 8, pp. 6860-6884, 2008.

[196] M. Backer, L. Delle, A. Poghossian, M. Biselli, W. Zang, P. Wagner, and M. J. Schoning, "Electrochemical sensor array for bioprocess monitoring," *Electrochimica Acta,* 2011.

[197] D. Braeken, D. R. Rand, A. Andrei, R. Huys, M. E. Spira, S. Yitzchaik, J. Shappir, G. Borghs, G. Callewaert, and C. Bartic, "Glutamate sensing with enzyme-modified floating-gate field effect transistors," *Biosensors and Bioelectronics,* vol. 24, pp. 2384-2389, 2009.

[198] H. Cao, Y. B. Peng, and J. C. Chiao, "An integrated flexible implantable L-glutamate sensor," in *Proceedings of IEEE Sensors*, pp. 2346-2350, 2010.

[199] S. Hozumi, K. Ikezawa, A. Shoji, A. Hirano-Iwata, T. Bliss, and M. Sugawara, "Simultaneous monitoring of excitatory postsynaptic potentials and extracellular l-glutamate in mouse hippocampal slices," *Biosensors and Bioelectronics,* vol. 26, pp. 2975-2980, 2011.

[200] W. Laiwattanapaisal, J. Yakovleva, M. Bengtsson, T. Laurell, S. Wiyakrutta, V. Meevootisom, O. Chailapakul, and J. Emneus, "On-chip microfluidic systems for determination of L-glutamate based on enzymatic recycling of substrate," *Biomicrofluidics,* vol. 3, 2009.

[201] S. Poorahong, P. Santhosh, G. V. Ramírez, T.-F. Tseng, J. I. Wong, P. Kanatharana, P. Thavarungkul, and J. Wang, "Development of amperometric [alpha]-ketoglutarate biosensor based on ruthenium-rhodium modified carbon fiber enzyme microelectrode," *Biosensors and Bioelectronics,* vol. 26, pp. 3670-3673, 2011.

[202] G. Wang, B. M. Daniel, and M. A. DeCoster, "Role of nitric oxide in regulating secreted phospholipase A2 release from astrocytes," *NeuroReport,* vol. 16, pp. 1345-1350, 2005.

[203] H. Sontheimer, "A role for glutamate in growth and invasion of primary brain tumors," *Journal of Neurochemistry,* vol. 105, pp. 287-295, 2008.

[204] Z.C. Ye and H. Sontheimer, "Glioma cells release excitotoxic concentrations of glutamate," *Cancer Research,* vol. 59, pp. 4383-4391, September 9, 1999.

[205] H. Kuskabe, Y, Midorikawa, T. Fujishima, A. Kuninaka., and H. Yoshino, "*Purification and properties of a new enzyme, L-glutamate oxidasse, from Streptomyces sp. X-119-6 grown on wheat bran* ," vol. 47. Tokyo, Japan: Agricultural Chemical Society of Japan, 1983.

[206] D. A. Bernards, D. J. MacAya, M. Nikolou, J. A. Defranco, S. Takamatsu, and G. G. Malliaras, "Enzymatic sensing with organic electrochemical transistors," *Journal of Materials Chemistry,* vol. 18, pp. 116-120, 2008.

[207] Z.C. Ye, M. S. Wyeth, S. Baltan-Tekkok, and B. R. Ransom, "Functional hemichannels in astrocytes: A novel mechanism of glutamate release," *The Journal of Neuroscience,* vol. 23, pp. 3588-3596, May 1, 2003.

[208] W. J. Chung, S. A. Lyons, G. M. Nelson, H. Hamza, C. L. Gladson, G. Y. Gillespie, and H. Sontheimer, "Inhibition of cystine uptake disrupts the growth of primary brain tumors," *The Journal of Neuroscience,* vol. 25, pp. 7101-7110, August 3, 2005.